Dynamics of semiconductor spin qubits in their actual environment

Mehmandoost, M.

DOI
10.4233/uuid:985e08ad-7d4d-4b6c-97a5-d51f8ac80176

Publication date
2024

Document Version
Final published version

Citation (APA)
Mehmandoost, M. (2024). *Dynamics of semiconductor spin qubits in their actual environment*. [Dissertation (TU Delft), Delft University of Technology]. https://doi.org/10.4233/uuid:985e08ad-7d4d-4b6c-97a5-d51f8ac80176

Important note
To cite this publication, please use the final published version (if applicable).
Please check the document version above.

Dynamics of semiconductor spin qubits

IN THEIR ACTUAL ENVIRONMENT

Dynamics of semiconductor spin qubits

IN THEIR ACTUAL ENVIRONMENT

Proefschrift

ter verkrijging van de graad van doctor
aan de Technische Universiteit Delft,
op gezag van de Rector Magnificus prof. ir. T. van der Hagen,
voorzitter van het College voor Promoties,
in het openbaar te verdedigen op dinsdag 12 november 2024 om 15:00 uur

door

Mohammad Mehmandoost

MSc in Physics,
Ulm University, Ulm, Germany,
Born in Rasht, Iran.

Dit proefschrift is goedgekeurd door de co-promotor en promotor.

Samenstelling promotiecommissie:

Rector Magnificuss	voorzitter
Prof. dr. ir. L.M.K. Vandersypen	Technische Universiteit Delft, promotor
Dr. V.V. Dobrovitski	Technische Universiteit Delft, co-promotor
Onafhankelijke leden:	
Prof. dr. B.M. Terhal	Technische Universiteit Delft
Prof. dr. Y.V. Nazarov	Technische Universiteit Delft
Dr. Ł. Cywiński	Institute of Physics Polish Academy of Sciences
Dr. D.J. Michalak	Nederlandse Organisatie voor Toegepast-Natuurwetenschappelijk Onderzoek
Dr. M. Veldhorst	Technische Universiteit Delft, reservelid
Overige leden:	
Dr. M. Rimbach-Russ	Technische Universiteit Delft

Geprint door: Proefschriftenprinten.nl

ISBN 978-94-6366-954-2

Een elektronische versie van dit proefschrift is te vinden op
http://repository.tudelft.nl/.

To my family

Contents

Summary

Quantum computers can solve specific problems with practical applications efficiently faster than classical computers. Spin qubits in semiconductor quantum dots are one of the most promising physical realizations of the quantum computers. This thesis aims to investigate the dynamics of semiconductor spin qubits in their actual environment. Specifically, we aim to understand how the actual environment of the spin qubits give rise to nonlinear response of the qubits to external driving, crosstalk, dephasing (T_2 processes), and the temperature-dependence of the qubit frequency.

Chapter 3 reports on experimental observation of the nonlinear response of the spin qubits to external driving as well as the crosstalk effect, where the Rabi frequency of an adjacent qubit changes as the target qubit is driven. We propose a phenomenological model that relates the external drivings to the observed dynamics of the spin qubits. The physical mechanism that give rise to these phenomena could not be reproduced in our analysis.

Given the progress in reducing noise sources in the spin qubits environment, it is pertinent to investigate the dephasing of spin qubits in a sparse bath of defects. In Chapter 4, we theoretically investigate the qubit dephasing, as measured in the Ramsey and Hahn echo experiments, in a sparse bath of two-level fluctuators (TLFs) with $1/f$ spectral density. We find that although the spectral density remains approximately unchanged, the coherence times become more variable as the bath becomes more sparse. We also find that in a sparse bath the qubit decoherence is dominated by only a fraction of TLF defects. Removing these defects results in a significant improvement of the coherence times.

Chapter 5 explores the potential of a bath of TLFs in elucidating the frequency shifts of spin qubits with temperature and the temperature insensitivity of Ramsey and echo decay times. These effects have been observed in experiments. By tuning the bath parameters, we are able to replicate the observed qubit frequency shift. However, our simulations reveal a decrease in qubit decoherence with temperature, which is inconsistent with the experimental findings.

On the whole, Chapters 3 and 5 aim to refine the models that we use to describe the dynamics of spin qubit in their environment. On the other hand, the theoretical work in Chapter 4 is inspired by the experimental observation of the variability of qubit decoherence and offers suggestions to improve coherence times in certain parameter regimes.

Samenvatting

Kwantumcomputers kunnen specifieke problemen met praktische toepassingen efficiënter en sneller oplossen dan klassieke computers. Spin qubits in halfgeleider kwantum dots zijn een van de meest veelbelovende fysieke realisaties van de kwantumcomputers. Dit proefschrift heeft tot doel de dynamiek van halfgeleider spin qubits in hun werkelijke omgeving te onderzoeken. Specifiek willen we begrijpen hoe de werkelijke omgeving van de spin qubits leidt tot een niet-lineaire respons van de qubits op externe aansturing, crosstalk, dephasing (T_2-processen) en de temperatuurafhankelijkheid van de qubit frequentie.

Hoofdstuk 3 rapporteert over experimentele observatie van de niet-lineaire respons van de spin qubits op externe aansturing, evenals het crosstalk-effect, waarbij de Rabi-frequentie van een aangrenzende qubit verandert wanneer de doel-qubit wordt aangestuurd. We stellen een fenomenologisch model voor dat de externe aansturingen relateert aan de waargenomen dynamiek van de spin qubits. Het fysieke mechanisme dat aanleiding geeft tot deze verschijnselen kon in onze analyse niet worden gereproduceerd.

Gezien de vooruitgang in het verminderen van ruisbronnen in de omgeving van spin qubits, is het relevant om de dephasing van spin qubits in een spaarzaam bad van defecten te onderzoeken. In Hoofdstuk 4 onderzoeken we theoretisch de dephasing van qubits, zoals gemeten in de Ramsey en Hahn-echo experimenten, in een spaarzaam bad van Two-Level Fluctuatoren (TLF's) met $1/f$ spectrale dichtheid. We vinden dat hoewel de spectrale dichtheid ongeveer onveranderd blijft, de coherentietijden variabeler worden naarmate het bad schaarser wordt. We vinden ook dat in een spaarzaam bad de qubit-decoherentie wordt gedomineerd door slechts een fractie van TLF-defecten. Het verwijderen van deze defecten resulteert in een significante verbetering van de coherentietijden.

Hoofdstuk 5 verkent het potentieel van een bad van TLF's om de frequentieverschuivingen van spin qubits met temperatuur en de temperatuuronafhankelijkheid van Ramsey- en echo-vervaltijden te verduidelijken. Deze effecten zijn waargenomen in experimenten. Door de badparameters af te stemmen, kunnen we de waargenomen qubit-frequentieverschuiving repliceren. Onze simulaties laten echter een afname zien in de decoherentie van qubits met de temperatuur, wat inconsistent is met de experimentele bevindingen.

Over het algemeen genomen hebben de hoofdstukken 3 en 5 tot doel de modellen te verfijnen die we gebruiken om de dynamiek van spin qubit in hun omgeving te beschrijven. Aan de andere kant is het theoretische werk in Hoofdstuk 4 geïnspireerd door de experimentele observatie van de variabiliteit van qubit-decoherentie en biedt het suggesties om de coherentietijden in bepaalde parameterregimes te verbeteren.

1

Introduction

The development of a scalable quantum computer based on semiconductor spin qubits requires a thorough understanding of the dynamics of these qubits in their actual environment. In this chapter, we provide a brief overview of the physical system that we are concerned with, and point at the mechanisms that hinder our progress towards building a scalable quantum computer based on semiconductor quantum dots.

1

1.1. Motivation

Scientific research can be likened to exploring uncharted territories, where the landscape is shaped by the work of those who have come before. Our objective may be to build upon existing discoveries, find connections between well-established principles, or investigate unusual phenomena that arise in unfamiliar domains. This thesis reports on such a journey within the realm of quantum science and technology. In this section, we outline the key areas of exploration and the specific challenges we aim to address.

At the heart of quantum science and technology lies the promise of harnessing physical laws governing quantum mechanical systems to revolutionize various fields, including secure communication, ultra-precise sensing, and computation [1]. One of the most transformative applications is quantum computing, which leverages the unique quantum phenomena, such as superposition and entanglement, to solve certain problems more efficiently than classical computers [2–4].

The basic unit of representing data in a quantum computer, the qubit, can be physically realized using any two-state quantum mechanical system. Semiconductor quantum dot spin qubits, in particular, hold great promise for the realization of large qubit registers due to their compatibility with established semiconductor fabrication techniques, making them strong candidates for scalable quantum computing [5–7]. There are several types of semiconductor spin qubits, which differ in their definitions and device structures (for a review, see Refs. [7–9]). This thesis explores a specific type of semiconductor spin qubits, defined as the spin states of single electrons confined to semiconductor quantum dots [10].

Semiconductor quantum dots are small disks formed in a two-dimensional electron gas, shaped by the electrostatic potentials of metallic gates on a semiconductor heterostructure. In this thesis, we focus primarily on spin qubits in Si/SiGe heterostructures, although the models presented may also be applicable to other device structures, such as SiMOS [9], and even to other types of qubits like superconducting qubits. In Si/SiGe devices, single-qubit gates are implemented via electric-dipole spin resonance, while two-qubit gates are based on the exchange interaction between neighboring electron spins, controlled by electrical gating of the potential barrier between adjacent dots. Several key factors make qubit registers composed of arrays of quantum dots promising for quantum computing: high-fidelity single- and two-qubit gates, robust electrical initialization and readout, long coherence times, and the small physical size of the qubits, which facilitates scalability [11–13]. For a comprehensive review of various aspects of semiconductor spin qubits, see Ref. [7].

Semiconductor spin qubits are susceptible to a range of undesired effects originating from their environment within the intricate quantum dot device structure [7]. By studying the dynamics of spin qubits, this thesis aims to gain insights into phenomena such as decoherence, crosstalk, unusual responses to pulsed electromagnetic fields, and unexpected dependencies on physical conditions like temperature. Investigating these effects offers valuable insights into the qubits' environment, which can contribute to the fabrication of higher-quality qubit devices and optimizing quantum control techniques.

Despite decades of research, the environment of semiconductor spin qubits is still not fully understood. This is partly due to the continuous evolution of device materials and structures, as well as the increasing number of qubits in prototype quantum computers, which introduces new challenges. In the early stages of investigating noise-induced qubit decoherence, much of the focus was on noise originating from the atomic nuclei of the host material [14, 15]. However, this magnetic noise was largely mitigated by using isotopically purified ^{28}Si, reducing the concentration of residual ^{29}Si nuclear spins to around 800 ppm, and shifting the primary source of decoherence to electric noise [16]. Moreover, recent efforts to scale spin qubits into larger arrays have underscored the need to better understand crosstalk mechanisms, possibly arising from qubit-environment coupling [17]. Additionally, the desire to operate spin qubits at higher temperatures and the pulse-induced qubit frequency shifts have drawn increased attention to the thermodynamics of spin qubits and their environment [18, 19].

Background electric field fluctuation, commonly referred to as charge noise, is a significant source of both decoherence and gate errors in spin qubit devices [20, 21]. The origins of charge noise can vary, with one potential source being an ensemble of two-level fluctuators (TLFs). Roughly speaking, TLFs are charged two-state quantum mechanical systems that randomly switch states due to interactions with their surrounding environment. Originally, TLF defects were proposed to explain the unusual low-temperature behavior of glasses [22–24] and were later used to describe the lossy environments in superconducting circuits, where their existence has been experimentally confirmed [25, 26]. More recently, TLF-based models have been employed to explain charge noise in semiconductor quantum dots [27–29], and single TLFs have even been individually manipulated in very recent studies [30].

A substantial part of this thesis, presented in Chapters 2, 4, and 5, focuses on qubit decoherence induced by TLFs in the environment, while Chapter 3 explores crosstalk mechanism and unusual response of the spin qubits to extreme external drivings. Chapter 2 introduces the key concepts and tools that are frequently referenced in later chapters. Chapter 3 reports on experiments investigating crosstalk and the nonlinear response of semiconductor spin qubits to microwave drives used for single-qubit rotations. Chapter 4 examines qubit decoherence in a sparse bath of TLFs producing $1/f$ noise, demonstrating that large variability of coherence properties is a hallmark of sparse TLF baths. Finally, Chapter 5 studies the temperature dependence of the spin qubits' Larmor frequency and coherence times, motivated by recent experimental findings. The overall structure of this thesis is outlined in the next section.

1.2. Thesis structure

The structure of this thesis is as follows:

- Chapter 2 introduces the theoretical tools and concepts that are frequently used in later chapters. We review the Gaussian random processes and describe the qubit decoherence by such a noise in terms of the noise spectral density. This description is only valid within the Gaussian limit of the environmental

noise. We provide the formulas for the general case of qubit decoherence by an ensemble of TLFs generating noise with non-Gaussian statistics.

- Chapter 3, presents the experiments on the unusual response of the spin qubits to microwave driving, as well as a novel crosstalk mechanism where the Rabi frequency of an adjacent qubit changes as a target qubit is driven. This chapter also presents a simple phenomenological model describing both effects simultaneously.

- Chapter 4 investigates the qubit decoherence caused by a sparse bath of TLFs, producing $1/f$ noise, showing that in such a bath, Ramsey and echo decay are subject to large variations among samples. The chapter also demonstrates that in certain parameter regimes, qubit decoherence in sparse baths is primarily dominated by a few TLFs. Removing these TLFs leads to remarkable improvements in coherence times.

- Chapter 5 presents a theoretical model that explains the qubit frequency shift as well as the insensitivity of Ramsey and echo decay times to temperature. The model attributes the frequency shift to charge noise originating from TLFs. Numerical simulations of the model demonstrate that adjusting model parameters can reproduce each effect individually, but not simultaneously.

References

[1] M. A. Nielsen and I. L. Chuang, *Quantum Computation and Quantum Information: 10th Anniversary Edition* (Cambridge University Press, 2010).

[2] D. Deutsch, *Quantum theory, the Church-Turing principle and the universal quantum computer,* Proceedings of the Royal Society of London. A. Mathematical and Physical Sciences **400**, 97 (1985), https://royalsocietypublishing.org/doi/pdf/10.1098/rspa.1985.0070 .

[3] R. P. Feynman, *Quantum mechanical computers,* in *Between Quantum and Cosmos*, edited by A. V. der Merwe, W. H. Zurek, and W. A. Miller (Princeton University Press, Princeton, 1988) pp. 523–548.

[4] J. Preskill, *Lecture notes for physics 229: Quantum information and computation,* Online (1998), `http://theory.caltech.edu/~preskill/ph229/`.

[5] F. A. Zwanenburg, A. S. Dzurak, A. Morello, M. Y. Simmons, L. C. L. Hollenberg, G. Klimeck, S. Rogge, S. N. Coppersmith, and M. A. Eriksson, *Silicon quantum electronics,* Rev. of Mod. Phys. **85**, 961 (2013).

[6] L. M. K. Vandersypen and M. A. Eriksson, *Quantum computing with semiconductor spins,* Phys. Today **72**, 38 (2019).

[7] G. Burkard, T. D. Ladd, A. Pan, J. M. Nichol, and J. R. Petta, *Semiconductor spin qubits,* Rev. Mod. Phys. **95**, 025003 (2023).

[8] R. Hanson, L. P. Kouwenhoven, J. R. Petta, S. Tarucha, and L. M. K. Vandersypen, *Spins in few-electron quantum dots,* Rev. Mod. Phys. **79**, 1217 (2007).

[9] W. I. L. Lawrie, H. G. J. Eenink, N. W. Hendrickx, J. M. Boter, L. Petit, S. V. Amitonov, M. Lodari, B. Paquelet Wuetz, C. Volk, S. G. J. Philips, G. Droulers, N. Kalhor, F. van Riggelen, D. Brousse, A. Sammak, L. M. K. Vandersypen, G. Scappucci, and M. Veldhorst, *Quantum dot arrays in silicon and germanium,* Applied Physics Letters **116** (2020), 10.1063/5.0002013, 080501.

[10] D. Loss and D. P. DiVincenzo, *Quantum computation with quantum dots,* Phys. Rev. A **57**, 120 (1998).

[11] E. Kawakami, P. Scarlino, D. R. Ward, F. R. Braakman, D. E. Savage, M. G. Lagally, M. Friesen, S. N. Coppersmith, M. A. Eriksson, and L. M. K. Vandersypen, *Electrical control of a long-lived spin qubit in a Si/SiGe quantum dot,* Nat. Nanotechnol. **9**, 666 (2014).

[12] X. Xue, M. Russ, N. Samkharadze, B. Undseth, A. Sammak, G. Scappucci, and L. M. K. Vandersypen, *Quantum logic with spin qubits crossing the surface code threshold,* Nature **601**, 343 (2022).

[13] S. G. J. Philips, M. T. Mądzik, S. V. Amitonov, S. L. de Snoo, M. Russ, N. Kalhor, C. Volk, W. I. L. Lawrie, D. Brousse, L. Tryputen, B. P. Wuetz, A. Sammak, M. Veldhorst, G. Scappucci, and L. M. K. Vandersypen, *Universal control of a six-qubit quantum processor in silicon,* Nature **609**, 919 (2022).

[14] G. Burkard, D. Loss, and D. P. DiVincenzo, *Coupled quantum dots as quantum gates,* Phys. Rev. B **59**, 2070 (1999).

[15] W. A. Coish and D. Loss, *Hyperfine interaction in a quantum dot: Non-markovian electron spin dynamics,* Phys. Rev. B **70**, 195340 (2004).

[16] L. M. K. Vandersypen, H. Bluhm, J. S. Clarke, A. S. Dzurak, R. Ishihara, A. Morello, D. J. Reilly, L. R. Schreiber, and M. Veldhorst, *Interfacing spin qubits in quantum dots and donnors–hot, dense, and coherent,* npj Quantum Inf. **3**, 34 (2017).

[17] B. Undseth, X. Xue, M. Mehmandoost, M. Rimbach-Russ, P. T. Eendebak, N. Samkharadze, A. Sammak, V. V. Dobrovitski, G. Scappucci, and L. M. Vandersypen, *Nonlinear response and crosstalk of electrically driven silicon spin qubits,* Phys. Rev. Appl. **19**, 044078 (2023).

[18] B. Undseth, O. Pietx-Casas, E. Raymenants, M. Mehmandoost, M. T. Mądzik, S. G. J. Philips, S. L. de Snoo, D. J. Michalak, S. V. Amitonov, L. Tryputen, B. P. Wuetz, V. Fezzi, D. D. Esposti, A. Sammak, G. Scappucci, and L. M. K. Vandersypen, *Hotter is easier: unexpected temperature dependence of spin qubit frequencies,* (2023), arXiv:2304.12984 [cond-mat.mes-hall] .

[19] K. Takeda, J. Yoneda, T. Otsuka, T. Nakajima, M. R. Delbecq, G. Allison, Y. Hoshi, N. Usami, K. M. Itoh, S. Oda, T. Kodera, and S. Tarucha, *Optimized electrical control of a Si/SiGe spin qubit in the presence of an induced frequency shift,* npj Quantum Inf. **4**, 54 (2018).

[20] E. Paladino, Y. M. Galperin, G. Falci, and B. L. Altshuler, $1/f$ *noise: Implications for solid-state quantum information,* Rev. Mod. Phys. **86**, 361 (2014).

[21] F. Beaudoin and W. A. Coish, *Microscopic models for charge-noise-induced dephasing of solid-state qubits,* Phys. Rev. B **91**, 165432 (2015).

[22] R. C. Zeller and R. O. Pohl, *Thermal conductivity and specific heat of nanocrystalline solids,* Phys. Rev. B **4**, 2029 (1971).

[23] P. W. Anderson, B. I. Halperin, and C. M. Varma, *Anomalous low-temperature thermal properties of glasses and spin-glasses,* Philos. Mag. **25**, 1 (1972).

[24] W. A. Phillips, *Tunneling states in amorphous solids,* J. Low Temp. Phys. **7**, 351 (1972).

[25] J. Lisenfeld, A. Bilmes, A. Megrant, R. Barends, J. Kelly, P. Klimov, G. Weiss, J. M. Martinis, and A. V. Ustinov, *Electric field spectroscopy of material defects in transmon qubits,* npj Quantum Information **5**, 105 (2019).

[26] C. Müller, J. H. Cole, and J. Lisenfeld, *Towards understanding two-level-systems in amorphous solids: insights from quantum circuits,* Rep. Prog. Phys. **82**, 124510 (2019).

[27] Y. Choi and R. Joynt, *Interacting random-field dipole defect model for heating in semiconductor-based qubit devices,* (2023), arXiv:2308.00711 [quant-ph] .

[28] D. Mickelsen, H. M. Carruzzo, S. N. Coppersmith, and C. C. Yu, *Effects of temperature fluctuations on charge noise in quantum dot qubits,* (2023), arXiv:2305.14515 [cond-mat.mes-hall] .

[29] R. E. Throckmorton and S. D. Sarma, *A generalized model of the noise spectrum of a two-level fluctuator in the presence of an electron subbath,* (2023), arXiv:2305.14348 [cond-mat.mes-hall] .

[30] F. Ye, A. Ellaboudy, and J. M. Nichol, *Stabilizing an individual charge fluctuator in a si/sige quantum dot,* (2024), arXiv:2407.05439 [cond-mat.mes-hall] .

2

Theoretical toolbox

This chapter presents the theoretical tools necessary to navigate the thesis. These tools include certain characteristics of random processes, as well as descriptions of qubit decoherence induced by environmental fluctuations considered in this thesis. This chapter is neither exhaustive nor pedagogical. It aims to introduce the language spoken in the following chapters.

2.1. The qubit

The qubit is defined by the basis states $|0\rangle$ and $|1\rangle$ in a two-dimensional Hilbert space. An arbitrary qubit state may be written as

$$|\psi\rangle = \alpha|0\rangle + \beta|1\rangle, \tag{2.1}$$

where α and β are complex numbers satisfying the normalization condition

$$|\alpha|^2 + |\beta|^2 = 1. \tag{2.2}$$

A global phase multiplying the qubit state does not change the expectation value of any observable. By ignoring the global phase and taking the normalization condition into account, the qubit state can be represented by two independent real numbers. This motivates representing the qubit state on the Bloch sphere as

$$|\psi\rangle = \cos\frac{\theta}{2}|0\rangle + e^{i\phi}\sin\frac{\theta}{2}|1\rangle, \tag{2.3}$$

where $\theta \in [0,\ \pi]$ and $\phi \in [0,\ 2\pi]$ are the polar and azimuthal angles. The qubit state on the Bloch sphere is illustrated in Fig. 2.1.

The qubit is by definition in a *pure state* if the state vector $|\psi\rangle$ is precisely known. In this thesis, we will work with statistical ensembles of qubit states. The qubit density matrix defined as

$$\hat{\rho} = \sum_k p_k |\psi_k\rangle\langle\psi_k|, \tag{2.4}$$

enables us to represent the statistical ensemble of qubit states. The coefficient p_k gives the probability of finding the qubit in the pure state $|\psi_k\rangle$. The sum of these probabilities equals one.

It is useful to represent the qubit density matrix as

$$\hat{\rho} = \frac{1}{2}(\mathbf{1} + m_x\hat{\sigma}_x + m_y\hat{\sigma}_y + m_z\hat{\sigma}_z), \tag{2.5}$$

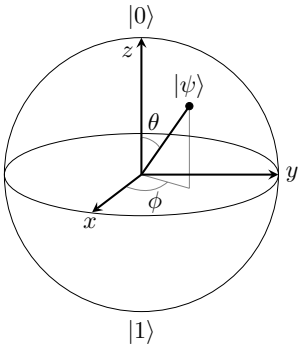

Figure 2.1: Bloch sphere representation of the qubit state. The basis states $|0\rangle$ and $|1\rangle$ are located at the north and south poles. The normalization condition is satisfied by the unit length of the sphere radius. An arbitrary qubit state is denoted by a point on the sphere. The location of this point is given by the polar and azimuthal angles θ and ϕ.

where

$$\hat{\sigma}_x = \begin{bmatrix} 0 & 1 \\ 1 & 0 \end{bmatrix}, \qquad \hat{\sigma}_y = \begin{bmatrix} 0 & -i \\ i & 0 \end{bmatrix}, \qquad \hat{\sigma}_z = \begin{bmatrix} 1 & 0 \\ 0 & -1 \end{bmatrix}, \tag{2.6}$$

are the Pauli matrices and the coefficients

$$m_\eta = \sum_k p_k \langle \psi_k | \hat{\sigma}_\eta | \psi_k \rangle \tag{2.7}$$

with $\eta \in \{x, y, z\}$ are the Bloch vector components. If the density matrix $\hat{\rho}$ is known, the Bloch vector components can be calculated via $m_\eta = \mathrm{Tr}\{\hat{\sigma}_\eta \hat{\rho}\}$.

2.2. Gaussian random processes

In this section, we provide a concise overview of Gaussian random processes. We present the characteristic functional expression in terms of the Gaussian process's mean and autocorrelation function. This expression will serve as a key component in the next section, where we calculate the qubit decoherence within the Gaussian approximation of the environmental noise.

A continuous-time real-valued random process $X(\tau)$ is a collection of random variables indexed by time τ. Consider recording $X(\tau)$ for times $\tau \in [0,\ t]$. A single record of observing $X(\tau)$ gives the sample trace $x(\tau)$. The sample trace $x(\tau)$ is also a collection of samples, each taken from a single random variable. We assume each of these samples can take values from the set of real numbers $\mathbb{R}$.

To study the statistical properties of the random process $X(\tau)$, it is useful to introduce the collection of time points $\tau_1, \ldots, \tau_j, \ldots, \tau_n$, ordered according to

$$0 \leq \tau_1 \leq \tau_2 \leq \ \ldots \ \leq \tau_{n-1} \leq \tau_n \leq t. \tag{2.8}$$

The random process at a given time point τ_j, that is $X(\tau_j)$, is a single random variable denoted by X_j. A sample of X_j is denoted by x_j, and its probability density is denoted by $P_{X_j}(x_j)$. We arrange the collection of random variables X_j's by their indices in an ascending order, and represent them by the list

$$\mathbf{X} = \{X_1,\ \ldots\ , X_j\ ,\ \ldots\ ,\ X_n\}. \tag{2.9}$$

The collection of samples x_j's are similarly arranged and represented by the list

$$\mathbf{x} = \{x_1,\ \ldots\ , x_j\ ,\ \ldots\ ,\ x_n\}. \tag{2.10}$$

The joint probability density of $\mathbf{X}$ is denoted by $P_{\mathbf{X}}(\mathbf{x})$.

Defining a random process is analogous to defining a random variable. Consider the random variable X, with sample $x \in \mathbb{R}$, and the probability density $P_X(x)$. The probability of X taking a value in the interval $[x,\ x + dx]$ is given by

$$\Pr(x \leq X \leq x + dx) = P_X(x)dx. \tag{2.11}$$

Now, consider the random process $X(\tau)$ which can be observed at time points $\tau_1, \ldots, \tau_n$. Also, consider the fixed infinitesimal intervals

$$[x_1,\ x_1 + dx_1],\ \ldots\ ,\ [x_n,\ x_n + dx_n], \tag{2.12}$$

at time points $\tau_1, \ldots, \tau_n$. The random process $X(\tau)$ is defined if the probability of its trace passing through these infinitesimal intervals is known for any set of time points $\tau_1, \ldots, \tau_n$ with $n = 1, \ldots, \infty$ [1]. This probability may be written as

$$\Pr(x_1 < X_1 \leq x_1 + dx_1, \cdots, x_n < X_n \leq x_n + dx_n) = P_{\mathbf{X}}(\mathbf{x})d\mathbf{x}, \tag{2.13}$$

where $d\mathbf{x} = \prod_{j=1}^{n} dx_j$. The probability of $X(\tau)$ taking values within the intervals $[x_k,\ x_k + dx_k],\ \cdots,\ [x_n,\ x_n + dx_n]$, given that $X(\tau)$ has already taken certain values of $x_1,\ \cdots,\ x_{k-1}$, is given by

$$P(x_1,\ \cdots, x_{k-1}|x_k, \cdots, x_n) \prod_{j=k}^{n} dx_j, \tag{2.14}$$

where $P(x_1,\ \cdots, x_{k-1}|x_k, \cdots, x_n)$ denotes the conditional probability density. The random process $X(\tau)$ is a Markov process if for any set of time points $\tau_1,\ \cdots, \tau_n$ one has

$$P(x_1,\ \cdots, x_{n-1}|x_n) = P(x_{n-1}|x_n). \tag{2.15}$$

The statistical parameters of the random process $X(\tau)$ that will be used in this thesis are defined below:

- The average (mean) of a random process $X(\tau)$ is defined as

$$\mu(\tau) = \langle X(\tau) \rangle = \int x(\tau) P_X(x) dx. \tag{2.16}$$

  Here, $P_X(x)$ is the probability density of a single random variable, i.e., the random process $X(\tau)$ at a specific time τ.

- The n'th moment of the random process $X(\tau)$ can be expressed as

$$\langle X(\tau_1)X(\tau_2)\cdots X(\tau_n) \rangle = \int x(\tau_1)x(\tau_2)\cdots x(\tau_n) P_{\mathbf{X}}(\mathbf{x}) d\mathbf{x}, \tag{2.17}$$

  where $P_{\mathbf{X}}(\mathbf{x})$ is the joint probability density of the collection of random variables $X(\tau_1), \cdots, X(\tau_n)$.

- The second moment of a random process, known as the autocorrelation function, is represented as

$$c(\tau_1,\ \tau_2) = \langle X(\tau_1)X(\tau_2) \rangle. \tag{2.18}$$

- The variance of the random process $X(\tau)$ is defined as

$$\sigma^2(\tau) = \langle [X(\tau) - \langle X(\tau) \rangle]^2 \rangle. \tag{2.19}$$

A random process is stationary if all of its moments remain unchanged by a shift in time, i.e.,

$$\langle X(\tau_1)X(\tau_2)\cdots X(\tau_n) \rangle = \langle X(\tau_1 + s)X(\tau_2 + s)\cdots X(\tau_n + s) \rangle, \tag{2.20}$$

for all n, s, and timepoints $\tau_1, \cdots, \tau_n$. If $X(\tau)$ is stationary, its mean $\mu(\tau)$ and variance $\sigma^2(\tau)$ are time-independent. We simply denote the mean and variance of a stationary process by μ and σ^2. The autocorrelation function of a stationary random process satisfies

$$c(\tau_1,\ \tau_2) = c(\tau_1 + s,\ \tau_2 + s). \tag{2.21}$$

In other words, for a stationary process, only the difference between the two time points τ_1 and τ_2 matters. We therefore denote the autocorrelation function of a stationary process by

$$c(\tau) = \langle X(0)X(\tau)\rangle. \tag{2.22}$$

The spectral density of a stationary process is the Fourier transform of its autocorrelation function [1], i.e.,

$$S(\omega) = \frac{1}{2\pi}\int_{-\infty}^{+\infty} c(\tau)e^{-i\omega\tau}d\tau. \tag{2.23}$$

For a definition of spectral density that does not rely on the autocorrelation function, see for instance Refs. [1, 2].

The characteristic functional of the random process $X(\tau)$ is defined as

$$f[k(\tau)] = \langle \exp[i\int_0^t d\tau x(\tau)k(\tau)]\rangle, \tag{2.24}$$

where $k(\tau)$ is an arbitrary (as long as the integral exists) test function [2]. By expanding $f[k(\tau)]$ in powers of $k(\tau)$ the characteristic functional may be written as

$$f[k(\tau)] = \sum_{m=1}^{\infty}\frac{i^m}{m!}\int k(\tau_1)\cdots k(\tau_n)\langle X(\tau_1)\cdots X(\tau_n)\rangle d\tau_1\cdots d\tau_n. \tag{2.25}$$

The cumulant generating functional of the random process is defined as

$$\Psi[k(\tau)] = \ln\{f[k(\tau)]\}. \tag{2.26}$$

Expanding the cumulant generating functional in powers of $k(\tau)$ gives

$$\Psi[k(\tau)] = \sum_{m=1}^{\infty}\frac{i^m}{m!}\int k(\tau_1)\cdots k(\tau_n)\langle X(\tau_1)\cdots X(\tau_n)\rangle_c d\tau_1\cdots d\tau_n, \tag{2.27}$$

where $\langle X(\tau_1)\cdots X(\tau_n)\rangle_c$ is the n'th order cumulant of the random process.

The random process $X(\tau)$ is called a Gaussian random process if for all $\mathbf{X}$, the joint probability density $P_{\mathbf{X}}(\mathbf{x})$ is a multivariate Gaussian distribution [2]. If $X(\tau)$ is a Gaussian random process, its characteristic functional takes the form [1]

$$f[k(\tau)] = \exp[i\mu\int_0^t d\tau k(\tau) - \frac{1}{2}\int_0^t\int_0^t d\tau_1 d\tau_2\langle X(\tau_1)X(\tau_2)\rangle k(\tau_1)k(\tau_2)]. \tag{2.28}$$

Therefore, a Gaussian random process is fully characterized by its mean and autocorrelation function.

2.3. Decoherence within the Gaussian limit

In this section, we study qubit *decoherence* in an environment modeled by a Gaussian random process. Decoherence, in this context, pertains to the decay of the off-diagonal elements of the density matrix, $m_x \pm im_y$, due to interaction between the qubit and its environment. The qubit is subject to echo pulses that are both ideal (perfect π rotations) and instantaneous (δ-peaked in time). We show that encoding the echo pulses into the arbitrary auxiliary test function $k(\tau)$, here called the time-domain filter function, allows for obtaining a computationally tractable decoherence formula. This formula is expressed in terms of the noise spectral density $S(\omega)$ and the Fourier transformed filter function $K(\omega t)$.

Consider the qubit Hamiltonian

$$\hat{H}(\tau) = \frac{1}{2}x(\tau)\hat{\sigma}_z + h(\tau)\hat{\sigma}_x, \tag{2.29}$$

where $x(\tau)$ is a sample trace of $X(\tau)$ observed for times $\tau \in [0,\ t]$. Here, time t gives the duration of an experiment between initialization and read-out. The sequence of echo pulses are contained in

$$h(\tau) = \frac{1}{2}\sum_{j=1}^{n} \pi\delta(\tau - t_j). \tag{2.30}$$

The specific number of echo pulses n, and their timings t_j, depend on the type of experiment. We assume the qubit is initially polarized along the x-axis, with $m_x = 1$. We further assume the qubit density matrix to be reconstructable at read-out.

The time-evolution operator for a sample trace $x(\tau)$ may be written as ($\hbar = 1$)

$$\hat{U}(t;\ 0) = \hat{\mathcal{T}}\{\exp[-i\int_0^t d\tau \hat{H}(\tau)]\}, \tag{2.31}$$

where $\hat{\mathcal{T}}$ is the time-ordering operator. Given that each π-pulse implements the gate $i\hat{\sigma}_x$, the time-evolution operator may be expanded as

$$\hat{U}(t;\ 0) = i^n\hat{U}(t;\ t_n)\hat{\sigma}_x\hat{U}(t_n;\ t_{n-1})\hat{\sigma}_x\ \ldots\ \hat{\sigma}_x\hat{U}(t_2;\ t_1)\hat{\sigma}_x\hat{U}(t_1;\ 0), \tag{2.32}$$

where

$$\hat{U}(t_k;\ t_{k-1}) = \exp[-\frac{i}{2}\hat{\sigma}_z\int_{t_{k-1}}^{t_k} d\tau x(\tau)]. \tag{2.33}$$

Using the relation

$$\hat{\sigma}_x e^{i\alpha\hat{\sigma}_z}\hat{\sigma}_x = e^{-i\alpha\hat{\sigma}_z}, \tag{2.34}$$

the time evolution operator may be written as

$$\hat{U}(t;\ 0) = i^n\hat{U}(t;\ t_n)\hat{U}^\dagger(t_n;\ t_{n-1})\ \ldots\ \hat{U}^\dagger(t_2;\ t_1)\hat{U}(t_1;\ 0). \tag{2.35}$$

We now introduce the time-domain filter function [3]

$$k(\tau) = \sum_{k=0}^{n} (-1)^k \theta(t_{k+1} - \tau)\theta(\tau - t_k), \tag{2.36}$$

where θ is the Heaviside step function, $t_0 = 0$, and $t_{n+1} = t$. The parameters $t_1, \cdots, t_n$ are the same as in Eq. (2.30). We can now write the time-evolution operator for a sample trace of noise as

$$\hat{U}(t;\ 0) = i^n \exp[-\frac{i}{2}\hat{\sigma}_z \int_0^t d\tau\, x(\tau)\, k(\tau)]. \tag{2.37}$$

Since the qubit Bloch vector is confined to the xy-plane, it is convenient to work with the qubit phase coherence denoted by

$$f = \langle 1|\hat{\rho}|0\rangle = m_x + i m_y. \tag{2.38}$$

The qubit phase averaged over samples of the random process $X(\tau)$ can be expressed as

$$\begin{aligned} \bar{f}[k(t)] &= \langle 1|\langle \hat{U}(t;\ 0)\, \hat{\rho}(0)\, \hat{U}^\dagger(t;\ 0)\rangle_X |0\rangle \\ &= \langle \exp[-i \int_0^t d\tau\, x(\tau)\, k(\tau)]\rangle_X. \end{aligned} \tag{2.39}$$

The angular brackets $\langle \cdots \rangle_X$ in Eq. (2.39) denote averaging over traces of random processes $X(\tau)$; in the following, we drop the subscript X for simplicity. The average phase in Eq. (2.39) has the same form as the characteristic functional of the random processes $X(\tau)$. For the average phase $\bar{f}[k(\tau)]$ the arbitrary auxiliary test function $k(\tau)$ is chosen to be the filter function characterizing the sequence of echo pulses.

Assuming $X(\tau)$ to be a Gaussian random process, the average phase may be written as

$$\bar{f}[k(\tau)] = \exp[i\mu \int_0^t d\tau\, k(\tau) - \frac{1}{2}\int_0^t \int_0^t d\tau_1\, d\tau_2\, \langle X(\tau_1)X(\tau_2)\rangle\, k(\tau_1)\, k(\tau_2)]. \tag{2.40}$$

Equation above takes the same form of Eq. (2.28). Here, we designated the average phase to the characteristic functional and the time-domain filter function to the arbitrary auxiliary test function. The autocorrelation function can be written as the inverse Fourier transform of the noise spectral density, i.e.,

$$\langle X(\tau_1)X(\tau_2)\rangle = \int_{-\infty}^{+\infty} d\omega\, e^{i\omega(\tau_1 - \tau_2)} S(\omega). \tag{2.41}$$

Plugging equation above into Eq. (2.40), and integrating over τ_1 and τ_2 gives

$$\bar{f}(t) = \exp[i\mu \int_0^t d\tau k(\tau) - \frac{1}{2}\int_{-\infty}^{+\infty} d\omega S(\omega)|K(\omega t)|^2], \tag{2.42}$$

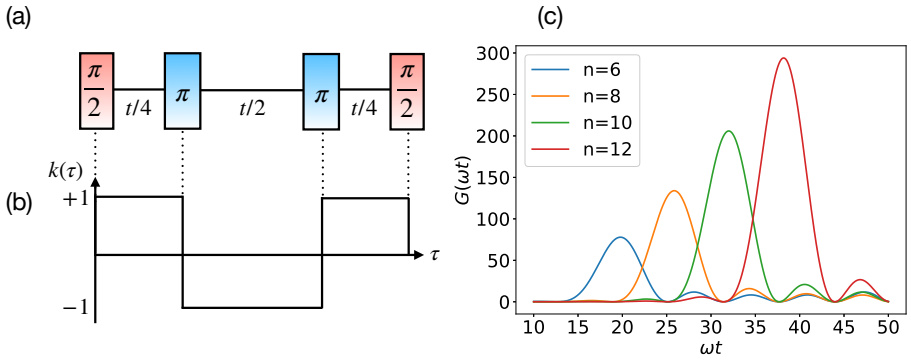

Figure 2.2: (a) CP sequence with two echo pulses (blue). The qubit is initialized in the state $|0\rangle$, and the first $\pi/2$ pulse (red) rotates it, for example, to align along the x axis. After the final $\pi/2$ pulse (red), the qubit state is measured in the computational basis, along the z axis. (b) Since the pulses are considered instantaneous and ideal, each π pulse effectively flips the sign of the noise, which is reflected in the time-domain filter function $k(\tau)$. For a general CP sequence with n echo pulses, the delay between the π pulses is t/n, while the initial and final delays after and before the $\pi/2$ pulses are $t/2n$. (c) The frequency-domain function $G(\omega t)$ for different values of $n = 6,\ 8,\ 10,\ 12$. As n increases, the peak shifts to higher frequencies.

where

$$K(\omega t) = \int_0^t d\tau\, e^{i\omega\tau}\, k(\tau). \tag{2.43}$$

Let us introduce the function

$$G(\omega t) = \omega^2 |K(\omega t)|^2. \tag{2.44}$$

Also, let us for simplicity assume that the noise is zero mean, i.e., $\mu = 0$. The average phase coherence then takes the form [3]

$$\bar{f}(t) = \exp[-\frac{1}{2}\int_{-\infty}^{+\infty} d\omega\, S(\omega)\, \frac{G(\omega t)}{\omega^2}]. \tag{2.45}$$

Figure 2.2 illustrates the frequency-selective nature of the function $G(\omega t)$ in the case of Carr-Purcell (CP) sequence. A CP sequence with $n = 2$ pulses and the corresponding time-domain filter function $k(\tau)$ are shown in Figs. 2.2 (a) and (b), respectively. For an even number of echo pulses n, the function $G(\omega t)$ takes the form

$$G(\omega t) = 8 \sin^4 \frac{\omega t}{4n} \sin^2 \frac{\omega t}{2} / \cos^2 \frac{\omega t}{2n}. \tag{2.46}$$

Figure 2.2(c) shows $G(\omega t)$ for multiple values of n. For a fixed n, $G(\omega t)$ is periodic in ωt. However, since $G(\omega t)$ multiplies by a $1/\omega^2$ in Eq. (2.45), the peaks shown in Fig. 2.2 play a dominant role in selecting specific parts of the spectral density $S(\omega)$, and thus in contributing to qubit decoherence. The term $G(\omega t)/\omega^2$ acts as a filter that passes noise within certain frequency bands. As the number of echo pulses increases, while keeping the measurement time t fixed, the peak of this bell-shaped function shifts to higher frequencies.

2.4. Decoherence induced by an ensemble of two-level fluctuators

A considerable share of this thesis is devoted to qubit decoherence induced by an ensemble of tunneling Two-Level Systems (TLSs). A tunneling TLS in contact with a bath of harmonic oscillators is an eminent example in the field of open quantum systems [4]. This system, often called the spin-boson model, has different regimes of behavior. We are in particular interested in the incoherent tunneling regime. In this regime, the TLS phase coherence is immediately lost after tunneling. Dynamics of the TLS thus reduces to a series of jumps between the excited and ground states. A TLS in this regime is often called the Two-Level Fluctuator (TLF). This motivates modeling the TLF by a two-state Markov process. In what follows, we present the formulas for qubit decoherence by an ensemble of TLFs in the Ramsey, Hahn echo, and Carr-Purcell experiments.

The two-state Markov process has only two states, denoted by $+1$ and -1, representing the TLF excited and ground states. This process is characterized by excitation and relaxation rates, $\gamma_\uparrow$ and $\gamma_\downarrow$. Let P_e and P_g be the probabilities of the TLF being in the excited and ground states, and define the vector $P = [P_e,\ P_g]^T$. The TLF rate equations can be expressed as

$$\dot{P}(\tau) = \mathbb{M}\, P(\tau), \tag{2.47}$$

where

$$\mathbb{M} = \begin{bmatrix} -\gamma_\downarrow & \gamma_\uparrow \\ \gamma_\downarrow & -\gamma_\uparrow \end{bmatrix}. \tag{2.48}$$

For a sample trace $x(\tau)$ of the two-state Markov process, the coherent dynamics of the qubit is governed by ($\hbar = 1$)

$$i\dot{\hat{\rho}}(\tau) = [\hat{H}(\tau),\ \hat{\rho}(\tau)], \tag{2.49}$$

where

$$\hat{H}(\tau) = \frac{1}{2} v\, k(\tau)\, x(\tau)\, \hat{\sigma}_z. \tag{2.50}$$

Here, v denotes the qubit-TLF coupling strength, and $k(\tau)$ is the time-domain filter function specified in Eq. (2.36).

Since the qubit state is confined to the xy-plane, it is more convenient to work with the qubit phase $f = m_x + i\, m_y$ instead of the density matrix $\hat{\rho}(\tau)$. Using Eq. (2.49), we can express the equation of motion of the qubit phase for the sample trace $x(\tau)$ as

$$\dot{f}(\tau) = i\, v\, k(\tau)\, x(\tau)\, f(\tau). \tag{2.51}$$

The solution to the differential equation above gives the qubit phase $f(\tau)$ for one realization of the random process $X(\tau)$, i.e., the sample trace $x(\tau)$. In other words, the solution $f(\tau)$ is a single realization of the random process $F(\tau)$, which depends on the two-state Markov process $X(\tau)$. We are interested in the average over all possible realizations of $f(\tau)$, which is denoted by $\bar{f}(\tau)$. The average phase $\bar{f}(\tau)$ can be obtained by utilizing the stochastic Liouville equations. Below, we briefly

describe how to calculate the average phase using the stochastic Liouville equations. A detailed description of this formalism can be found in Refs. [2, 5, 6].

As said, the random process $X(\tau)$ is Markovian. Therefore, the joint process $\{F(\tau),\ X(\tau)\}$ is also Markovian [2]. We use the abbreviated notation $P(f,\ x;\ \tau)$, instead of $P(f,\ x;\ \tau|f_0,\ x_0;\ \tau_0)$, for the transition probability of the joint process $\{F(\tau),\ X(\tau)\}$. We further define the transition probabilities

$$P_e(f,\ x;\ \tau) = P(f,\ +1;\ \tau|f_0,\ +1;\ \tau_0) + P(f,\ +1;\ \tau|f_0,\ -1;\ \tau_0), \tag{2.52}$$

and

$$P_g(f,\ x;\ \tau) = P(f,\ -1;\ \tau|f_0,\ +1;\ \tau_0) + P(f,\ -1;\ \tau|f_0,\ -1;\ \tau_0). \tag{2.53}$$

The transition probabilities $P_e(f,\ x;\ \tau)$ and $P_g(f,\ x;\ \tau)$ obey the equations [2]

$$\frac{\partial}{\partial\tau}P_e(f,\ x;\ \tau) = i\,v\,k(\tau)\,P_e(f,\ x;\ \tau) - \gamma_\downarrow P_e(f,\ x;\ \tau) + \gamma_\uparrow P_g(f,\ x;\ \tau), \tag{2.54}$$

and

$$\frac{\partial}{\partial\tau}P_g(f,\ x;\ \tau) = -i\,v\,k(\tau)\,P_g(f,\ x;\ \tau) + \gamma_\downarrow P_e(f,\ x;\ \tau) - \gamma_\uparrow P_g(f,\ x;\ \tau). \tag{2.55}$$

We define the marginal averages

$$\bar{f}_e(\tau) = \int df\ f(\tau)\,P_e(f,\ x;\ \tau), \tag{2.56}$$

and

$$\bar{f}_g(\tau) = \int df\ f(\tau)\,P_g(f,\ x;\ \tau). \tag{2.57}$$

Multiplying both sides of Eqs. (2.54) and (2.55) by f, and using the definition of marginal averages given in Eqs. (2.56) and (2.57), we arrive at the coupled equations

$$\dot{\bar{f}}_e = i\,v\,k(\tau)\,\bar{f}_e - \gamma_\downarrow\,\bar{f}_e + \gamma_\uparrow\,\bar{f}_g, \tag{2.58}$$

and

$$\dot{\bar{f}}_g = -i\,v\,k(\tau)\,\bar{f}_g + \gamma_\downarrow\,\bar{f}_e - \gamma_\uparrow\,\bar{f}_g. \tag{2.59}$$

The solution to the equations above gives the average phase $\bar{f}(\tau) = \bar{f}_g(\tau) + \bar{f}_e(\tau)$.

The average phase for the cases that will be considered in this thesis are given below. These formulas have been previously reported, e.g., in Refs. [7–11]. For simplicity, we drop the bar over the average phase $\bar{f}$. For a symmetric TLF $\gamma_\downarrow = \gamma_\uparrow$.

- Ramsey decay by an asymmetric TLF:

$$f_{\mathrm{R}}(t) = \exp(-\Gamma t)\left[\cosh(At) + \frac{\Gamma}{A}\sinh(At)\right], \tag{2.60}$$

with $\Gamma = \gamma - iv\delta\gamma/2\gamma$, $A = (\gamma^2 - iv\delta\gamma - v^2)^{\frac{1}{2}}$, $\gamma = (\gamma_\downarrow + \gamma_\uparrow)/2$ and $\delta\gamma = \gamma_\downarrow - \gamma_\uparrow$.

- Ramsey decay by a symmetric TLF:

$$f_{\mathrm{R}}(t) = e^{-\gamma t}(\cosh \alpha t + \frac{\gamma}{\alpha} \sinh \alpha t), \tag{2.61}$$

  where $\alpha = \sqrt{\gamma^2 - v^2}$.

- Echo decay by an asymmetric TLF:

$$\begin{aligned} f_{\mathrm{H}}(t) =& e^{-\gamma t}[\cosh(At/2)\cosh(A^*t/2) \\ &+ \frac{v^2+\gamma^2}{A^*A}\sinh(At/2)\sinh(A^*t/2) \\ &+ \frac{\Gamma}{A}\sinh(At/2)\cosh(A^*t/2) \\ &+ \frac{\Gamma^*}{A^*}\sinh(A^*t/2)\cosh(At/2)]. \end{aligned} \tag{2.62}$$

- Echo decay by a symmetric TLF:

$$f_{\mathrm{H}}(t) = e^{-\gamma t}(\frac{\gamma^2}{\alpha^2}\cosh \alpha t + \frac{\gamma}{\alpha}\sinh \alpha t - \frac{v^2}{\alpha^2}). \tag{2.63}$$

- Qubit dephasing by a symmetric TLF in the Carr-Purcell experiment:

$$f_{\mathrm{CP}}(t) = \frac{e^{-\gamma t}}{2}\left[\frac{\gamma^2\cosh(\alpha t/m) - v^2}{\alpha\sqrt{\gamma^2\cosh^2(\alpha t/m) - v^2}}(\mu_+^m - \mu_-^m) + \mu_+^m + \mu_-^m\right], \tag{2.64}$$

  with

$$\mu_\pm = \frac{\gamma}{\alpha}\left[\sinh(\alpha t/m) \pm \sqrt{\cosh^2(\alpha t/m) - v^2/\gamma^2}\right], \tag{2.65}$$

  and m denoting the number of echo pulses.

We now consider the Hamiltonian ($\hbar = 1$)

$$\hat{H}(\tau) = \frac{1}{2}\sum_k^N x_k(\tau)\hat{\sigma}_z + h(\tau)\hat{\sigma}_x, \tag{2.66}$$

for a qubit coupled to an ensemble of N independent TLFs. The function $h(\tau)$ is given in Eq. (2.30). It can be inferred from Eq. (2.39) that the decoherence induced by a TLF ensemble is the product

$$F(\tau) = \prod_{k=1}^N f_k(\tau). \tag{2.67}$$

Here, we omitted the subscripts denoting the type of experiment (Ramsey, Hahn echo, Carr-Purcell) for simplicity.

References

[1] R. Kubo, M. Toda, and N. Hashitsume, *Statistical Physics II: Nonequilibrium Statistical Mechanics* (Springer, Heidelberg, Germany, 1991).

[2] N. G. van Kampen, *Stochastic Processes in Physics and Chemistery*, 3rd ed. (Elsevier, Amsterdam, 2007).

[3] L. Cywiński, R. M. Lutchyn, C. P. Nave, and S. Das Sarma, Phys. Rev. B **77**, 174509 (2008).

[4] U. Weiss, *Quantum Dissipative Systems*, 4th ed. (WORLD SCIENTIFIC, 2012).

[5] R. Kubo, *Note on the stochastic theory of resonance absorption,* J. Phys. Soc. Jpn. **9**, 935 (1954).

[6] R. Kubo, *Stochastic Liouville equations,* J. Math. Phys. **4**, 174 (1963).

[7] G. Zhidomirov and K. M. Salikhov, *Contribution to the theory of spectral diffusion in magnetically diluted solids,* Sov. Phys. JETP **29**, 1037 (1969).

[8] E. Paladino, L. Faoro, G. Falci, and R. Fazio, *Decoherence and $1/f$ noise in Josephson qubits,* Phys. Rev. Lett. **88**, 228304 (2002).

[9] R. de Sousa and S. Das Sarma, *Theory of nuclear-induced spectral diffusion: Spin decoherence of phosphorus donors in Si and GaAs quantum dots,* Phys. Rev. B **68**, 115322 (2003).

[10] G. Ramon, *Dynamical decoupling of a singlet-triplet qubit afflicted by a charge fluctuator,* Phys. Rev. B **86**, 125317 (2012).

[11] G. Ramon, *Non-Gaussian signatures and collective effects in charge noise affecting a dynamically decoupled qubit,* Phys. Rev. B **92**, 155422 (2015).

3

Nonlinear response and crosstalk of electrically driven silicon spin qubits

Micromagnet-based electric dipole spin resonance offers an attractive path for the near-term scaling of dense arrays of silicon spin qubits in gate-defined quantum dots while maintaining long coherence times and high control fidelities. However, accurately controlling dense arrays of qubits using a multiplexed drive will require an understanding of the crosstalk mechanisms that may reduce operational fidelity. We identify a novel crosstalk mechanism whereby the Rabi frequency of a driven qubit is drastically changed when the drive of an adjacent qubit is turned on. These observations raise important considerations for scaling single-qubit control.

Author contributions: Participated in analyzing the results, developing the phenomenological model that relates the electrical drivings to the qubits' dynamics, and performing numerical simulations. All results of this chapter have been published in Ref. [1].

3.1. Introduction

Electric dipole spin resonance (EDSR) is a key ingredient for the all-electrical control of single-electron spin qubits in silicon quantum dots [2]. While some approaches are able to utilize the weak intrinsic spin-orbit coupling (SOC) of silicon [3, 4], the placement of an on-chip micromagnet has proven especially effective for gate-based quantum dots in both Si/SiGe [5, 6] and Si-MOS [7] platforms, with single-qubit gate fidelities exceeding 99.9% having been demonstrated [8]. Furthermore, electron spins in dense arrays can be made addressable by engineering an appropriate local magnetic field gradient within a stronger external field [9]. This makes micromagnet-based EDSR attractive for the near-term scaling of spin qubit processors.

In the original description of micromagnet-based EDSR, an ac electric field pushes a harmonically confined electron back and forth in a constant magnetic field gradient, such that the spin is effectively acted upon by an ac magnetic field as in conventional electron spin resonance (ESR) [10, 11]. An array of spectrally-separated spins can ideally be controlled via a single, multiplexed driving field containing a linear combination of frequencies addressing individual qubits. Rabi's formula implies that the qubit dynamics are only slightly affected by off-resonance tones such that crosstalk can be accounted for systematically to maintain high fidelity [12].

Substantial effort has been placed on detecting and modelling crosstalk in superconducting and trapped-ion systems [13], but the identification of crosstalk mechanisms in semiconductor quantum dot devices is only beginning to receive attention as these platforms mature into the multi-qubit era [14–16]. Given that high qubit density is one of the known advantages of semiconductor quantum processors, maintaining high-fidelity operation with small qubit pitch in the presence of crosstalk is an essential hurdle to overcome.

In this article, we measure the nonlinear Rabi frequency scaling of two single-electron spin qubits controlled via EDSR in a ^{28}Si/SiGe double-dot device. The nonlinearity gives rise to a sizeable crosstalk effect when attempting to drive simultaneous single-qubit rotations, and we develop a simple phenomenological extension of silicon-based EDSR theory to relate our observations. Although the physical origin of the nonlinearity is not precisely known, we find that anharmonicity in the quantum dot confining potential cannot quantitatively explain our measurements. We therefore comment on other device physics, such as microwave-induced artefacts, that may contribute to the crosstalk mechanism. The insights made here will help inform continued development of EDSR-enabled spin qubit devices, as well as raise important considerations for programming spin-based quantum processors in silicon.

3.2. Methods

To probe the behavior of two spin qubits controlled via a frequency multiplexed drive, two quantum dots with single-electron occupancy are electrostatically accumulated in an isotopically purified ^{28}Si/SiGe quantum well [Fig. 3.1(a)]. A cobalt micromagnet placed on top of the dot region becomes magnetized in the external

field applied along the z'-axis, creating local transverse (x'-axis) and longitudinal (z'-axis) magnetic field gradients. The transverse gradient gives rise to a synthetic SOC, and the longitudinal gradient spectrally separates the Larmor frequencies of the two spins. The IQ-modulated electric drive necessary to control the spin states by EDSR is delivered via the gate "MW" or the gate "B". Further details of the fabrication, initialization, control, and readout of the qubits can be found in [17] (we here used room temperature electronics only).

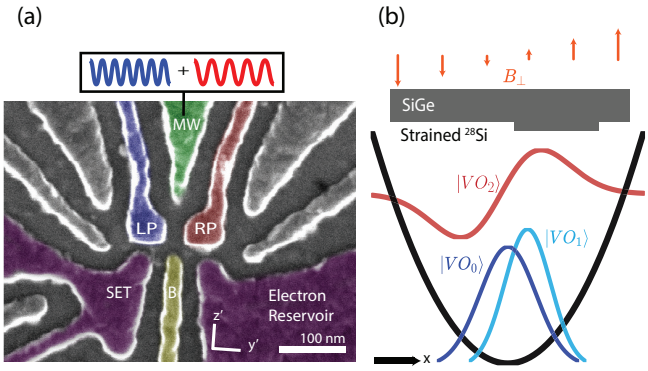

Figure 3.1: (a) False-coloured image of a device nominally equivalent to the one used in the experiment. Single-electron spin qubits Q1 and Q2 are confined under plunger gates "LP" and "RP" respectively, while a barrier gate "B" is used to control the tunnel coupling between the dots. Qubit states are read-out using energy-selective tunneling to the electron reservoir, with a single-electron transistor (SET) used to measure the corresponding change in charge-occupation. Microwave controls for both qubits are simultaneously applied to either the "MW" or "B" gate. (b) Illustration of wave function envelopes in a silicon quantum well. EDSR can be mediated by both the first excited orbit-like state $|\mathrm{VO}_2\rangle$ as well as the first excited valley-like state $|\mathrm{VO}_1\rangle$ as a consequence of interface-induced hybridization. Interface disorder here is represented as a rectangular "atomic step" for simplicity, but hybridization may also be a consequence of more detailed alloy disorder. In any case, a finite dipole transition element along with the micromagnet spin-orbit coupling enables electrically driven spin rotations.

In a gate-defined quantum dot in silicon, an electric field is able to couple spin-like qubit states via EDSR due to the spin-orbit coupling perturbing the pure spin eigenstates such that they become slightly hybridized with the electron charge states. For single-electron spin qubits in Si/SiGe, the charge states are themselves hybridized valley-orbit states owing to the nearly-degenerate conduction band valleys of strained silicon quantum wells [18]. EDSR may therefore be mediated by orbit-like or valley-like hybridized states which support a nonzero dipole transition element with the electron ground state, as illustrated in Fig. 3.1(b) [10, 19]. In either case, a robust linear relationship between the amplitude of the driving field and the Rabi frequency of the spin qubit is expected (see Appendices 3.B and 3.C).

To drive on-resonance Rabi oscillations, we first use a Ramsey pulse sequence to accurately identify the relevant resonance frequencies of the two qubits, which range from 11.89 GHz in a 320 mT external field to 15.91 GHz in 475 mT. This calibration strategy was also employed to achieve >99% fidelity universal control in this device

[20]. The corresponding drives are applied either to the "MW" or "B" gate, and the same driving frequency is used for all drive durations and amplitudes. A rectangular pulse with duration up to 3 μs is used, and the measured time-domain spin response is fit to a sinusoidal function $A\cos(2\pi f_{\mathrm{Rabi}}t+\phi)+C$ to extract the Rabi frequency. While it is well documented that qubit frequencies may shift nontrivially as a result of on- or off-resonant microwave driving [21], the relatively short pulses used here do not induce a shift large enough to compromise the fidelity of the Rabi oscillations.

3.3. Results

3.3.1. Nonlinear Rabi Scaling

We observe unexpected nonlinear Rabi frequency scaling when each spin is driven individually as shown in Fig. 3.2. We observe that the linear Rabi frequency-drive amplitude scaling predicted from theory only holds for Rabi frequencies up to 1-2 MHz. This is at odds with previous experimental demonstrations of micromagnet-based EDSR in silicon and GaAs, where Rabi frequencies of several tens of MHz have been measured to smoothly saturate [8, 22–24]. These results have been loosely interpreted as resulting from anharmonicity in the confinement potential, and we also find this a plausible explanation through numeric simulations in Appendix 3.C. However, confinement anharmonicity alone does not fully account for the nonlinearity and lower driving limit observed in the devices considered here. We emphasize that the crosstalk effect discussed in Sec. 3.3.2 will occur regardless of the cause of the nonlinearity, and the limited Rabi frequencies achieved in this device make crosstalk more prominent than could otherwise be expected.

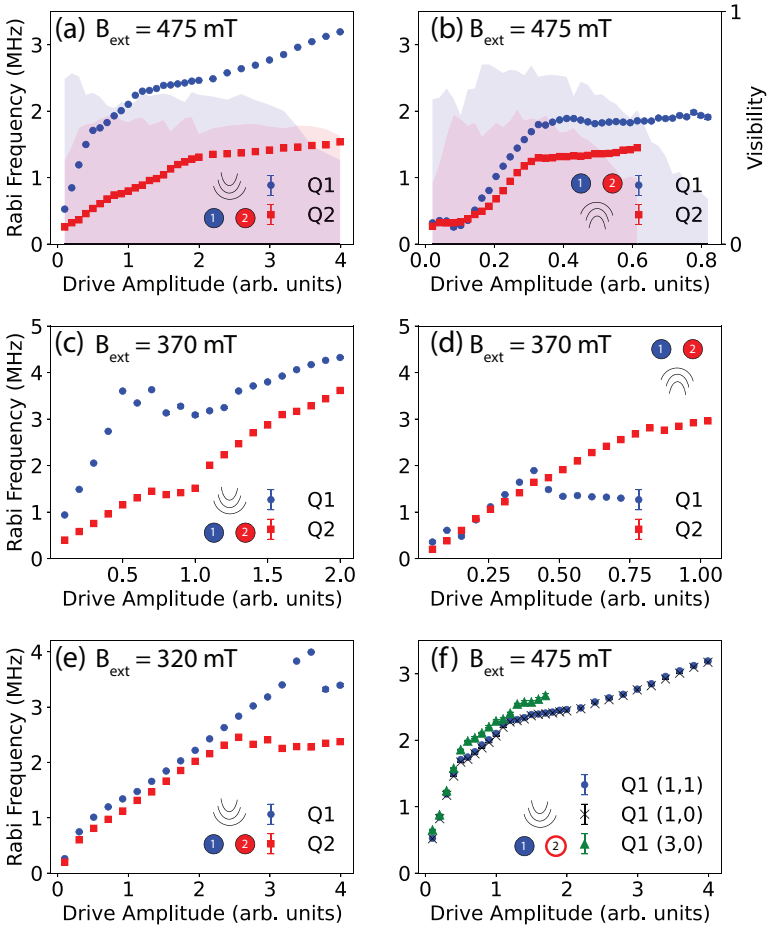

Figure 3.2: Rabi frequency scalings as a function of the applied resonant ac electric field amplitude. The external field is set to $B_{\text{ext}} = 475$ mT in (a),(b) and (f), $B_{\text{ext}} = 370$ mT in (c) and (d), and $B_{\text{ext}} = 320$ mT in (e). In (a), (c), (e), and (f) the qubits are driven using the "MW" gate as illustrated. In (b) and (d) the qubits are instead driven using the "B" gate. In (a-e) only a single qubit is driven at once in the (1,1) electron occupation regime, while the undriven qubit is left to idle. In (f) the Q1 Rabi scaling is compared in different charge states of the device. In (a-b) the visibility of the readout is indicated by the shaded regions. Q1 systematically has a higher visibility than Q2 as the latter is read out via a CROT interaction which has finite fidelity. Lowered visibility for longer drives is expected due to electron reservoir heating. The horizontal axis is scaled such that 1 arbitrary unit (arb. unit) represents the same nominal drive amplitude delivered to the device by taking into account the room-temperature vector source power and all nominal attenuation in the signal paths.

The exact electric field driving amplitude is not known precisely, so a linear scale is used such that 1 unit of amplitude is approximately equivalent to a 2 MHz Rabi frequency for Q1 in the configuration of Fig. 3.2(a). We estimate that this amplitude corresponds to a microwave power of about −35 dBm delivered to the

bonding wire to the sample [1]. This nominal amplitude is used as a reference for other experiments, when the attenuation in each line can be used to estimate the power delivered to the device [2]. Magnetostatic simulations of the on-chip micromagnet design estimate a stray field of $0.3-0.7$ mT/nm, depending on the effective driving axis, which is somewhat less than the 1 mT/nm estimated in other similar devices [8]. This smaller driving gradient necessitates a proportionally larger driving amplitude to achieve the same frequency, which may play a role in the observation of nonlinear effects at smaller Rabi frequencies.

For each quantum dot, external magnetic field, and driving gate, the associated curve contains unique, but robustly reproducible, nonlinear characteristics qualitatively similar to [7]. These often appear as "plateaus" where the Rabi frequency apparently saturates, or only changes modestly, when the amplitude of the electric drive is adjusted. Increasing the driving amplitude does not always yield larger Rabi frequencies, nor is the visibility or quality of Rabi oscillations immediately degraded in these regions. Longer driving does lead to some reduced visibility in part due to self-heating of the electron reservoirs used for energy-selective readout. In some experimental configurations, driving even more strongly in the nonlinear regime will lead to a sudden loss in qubit visibility. Decreased visibility and a diminished T_2^{Rabi} have been previously reported for fast EDSR in silicon [8, 23], and may also be a result of population leakage to spin-orbit states outside of the qubit subspace.

In addition to the general Rabi saturation effect observed, each measured Rabi scaling exhibits distinct kinks. Note that the difference in scaling trends between adjacent spins has previously been observed [26] and may be attributed to differences in the local magnetic field gradient at each dot location. However, this does not explain the nonlinearity in the qubit response as the micromagnet gradient is nearly constant over the 100 nm pitch of the dots. From the distinct shapes of the Q1 and Q2 curves, it is apparent that the origin of the nonlinearity is particular to each qubit frequency and not a global phenomena as could be expected from a uniform distortion in the driving field. We also note that a drive-induced shift in the qubit's resonance frequency, which has previously been observed in EDSR experiments [9, 21, 27], is not a plausible cause of the nonlinear scaling since an off-resonant drive will result in faster oscillations, not slower [28].

Next, we consider the possibility that the nonlinearity is due to the influence of the second qubit. However, upon removing the Q2 electron, there is no change in the Q1 Rabi scaling as shown in Fig. 3.2(f). Furthermore, the residual exchange interaction between the two qubits is measured to be below 50 kHz, indicating a very weak spin-spin interaction taking place. Repeating the experiment in the

[1] This is inferred based on a vector source generator output power of -14 dBm, a nominal attenuation of 6 dB at 4 K, and an estimated cable/connector attenuation of 15 dB.

[2] Unknown impedance mismatches at, for example, bonding wires connections, make the on-chip ac electric field vary with frequency. Therefore the comparison between Rabi scaling trends at different magnetic fields is qualitative. Previous photon-assisted tunneling measurements on similar devices estimate the electric field amplitude to be on the order of 1000 V/m, or equivalently a voltage amplitude of 0.1 mV on the gate [25]. This estimate, along with a transverse magnetic gradient of about $0.3-0.7$ mT/nm from simulations and a harmonic potential energy scale of 1 meV, agrees with the frequency of Rabi oscillations we observe.

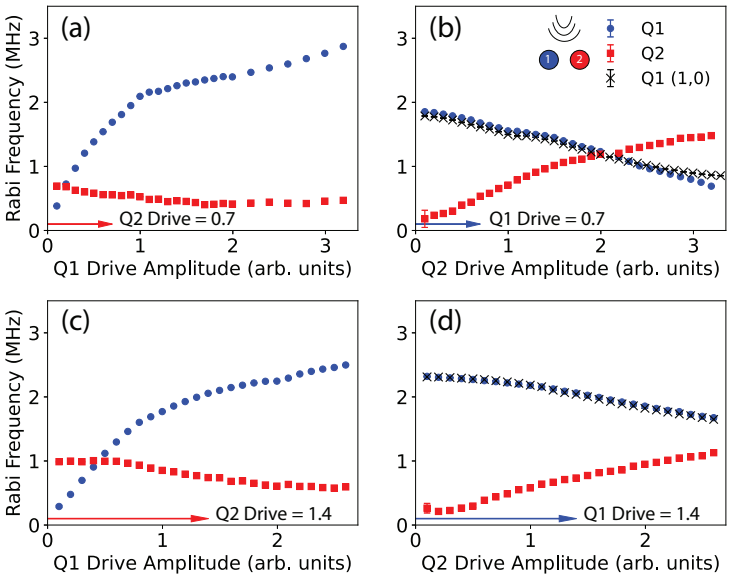

Figure 3.3: Crosstalk in single-qubit operation. The Rabi frequencies of both qubits are measured when a constant driving tone on-resonance with one qubit is present (shown in the bottom left of each panel) while a second tone resonant with the other qubit is swept in amplitude. In panels (a) and (b) the constant driving amplitude is half (0.7 arb. units) that in panels (c) and (d) (1.4 arb. units). Note that doubling the constant tone amplitude does not double the Rabi frequency, because the EDSR response is already nonlinear as shown in Fig. 3.2(a). In panels (b) and (d), the experiment repeated in the (1,0) regime gives nearly identical results as in the (1,1) regime. All experiments are carried out at $B_{\text{ext}} = 475$ mT, and the "MW" gate is used in all cases as indicated in the top right illustration.

(3,0) regime produces the same initial linear trend, suggesting that in both the 1-electron and 3-electron modes the same dipole transition element, whether orbit-like or valley-like, is responsible for mediating EDSR. The nonlinear scaling regime is similarly shaped, but measurably different, suggesting that the root cause of the nonlinearity may be somewhat influenced by the quantum dot structure.

3.3.2. Crosstalk

When both qubit driving tones are simultaneously applied to the "MW" gate, a large crosstalk effect occurs (Fig. 3.3). When a resonantly driven spin is also placed under the influence of an additional off-resonant drive, the additional ac field amplitude modifies the qubit response as to diminish the resonant spin-flip Rabi frequency. This effect has substantial consequences for high-fidelity logic gates which must be calibrated to a nanosecond-precision duration, because even a small unaccounted change in Rabi frequency would result in severe over- or under-rotations of qubit states. High-fidelity control can be maintained in a small device by operating gates serially [20, 29, 30], but this is an undesirable constraint for efficiently implementing quantum algorithms.

By comparing Fig. 3.3(a-b) with (c-d), it is clear that the Rabi frequency is more strongly modified when the resonant tone amplitude is smaller with respect to the off-resonant pulse amplitude. This implies that crosstalk would become more severe as single-qubit operations are more densely multiplexed. Directly adjusting microwave pulses for the unique response of each qubit may greatly increase the calibration overhead for larger qubit arrays, depending on the locality of the nonlinear response. We emphasize again that the crosstalk effect is not a consequence of the *existence* of a nearby qubit, but rather is caused by the act of driving a second nearby qubit. This is illustrated in Fig. 3.3(b) and (d), where the Q1 behavior is nearly identical in the case that the Q2 electron is removed from the double-dot region.

3.4. Discussion

We now introduce a model Hamiltonian to survey in more depth the possible origin of the observed nonlinearity and crosstalk. Consider the following micromagnet-enabled EDSR Hamiltonian:

$$H(t) = H_0 - \frac{E_Z}{2}\hat{\sigma}_z + b'_{SL}\hat{x}\vec{n}\cdot\vec{\sigma} + E'_{ac}(t)\hat{x}. \tag{3.1}$$

H_0 describes the orbital and valley degrees of freedom of the charge state. $E_Z = g\mu_B B_{\text{tot}}$ is the Zeeman splitting of the spin state, where $g \approx 2$ is the g-factor in silicon, μ_B is the Bohr magneton, and B_{tot} is the total magnetic field along the $\hat{\sigma}_z$ spin quantization axis. $\hat{x}$ is the 1D position operator along the driving axis, which is determined by the orientation of the electric driving field $E'_{ac}(t) = e\sum_k E_{ac,k}\sin(\omega_k t)$ at the quantum dot location. $b'_{SL} = \frac{1}{2}g\mu_B|\vec{b}_{SL}|$ gives the strength of the SOC as a function of the magnitude of the magnetic field gradient $|\vec{b}_{SL}|$ along this axis. $\vec{n} = \left(0, \cos\theta, \sin\theta\right)^T$ characterizes the nature of the SOC, where θ gives the angle of the gradient with respect to the $\hat{\sigma}_y$ spin quantization axis.

EDSR is simplest to investigate in the case of harmonic confinement of the electron with effective mass m^*, such that $H_0 = \hbar\omega_0(\hat{a}^\dagger\hat{a} + \frac{1}{2})$ with $\hat{a}^\dagger, \hat{a}$ being the quantum raising and lowering operators, $\hbar\omega_0$ giving the energy difference between orbital eigenstates, and $\hbar = h/2\pi$ as the reduced Planck's constant. The resulting Hamiltonian $H(t)$ can be analyzed perturbatively (see Appendix3.B) to find an on-resonance Rabi frequency of:

$$f_{\text{Rabi}} = \frac{g\mu_B|\vec{b}_{SL}|\cos\theta eE_{ac}}{2hm^*\omega_0^2} \tag{3.2}$$

and a drive-dependent resonance frequency shift of $\hbar\omega \propto -E_{ac}^2$ [28]. According to Equation 3.2, dot-to-dot variations in EDSR sensitivity are expected as different qubit locations will experience different confinement strengths, magnetic field gradients, and electric driving angles. However, proportionality to the oscillating electric field amplitude is always expected from Eq. 3.2.

Different linear scaling for small drives has been reported in both GaAs [22, 24, 26] and Si [5, 7, 8, 23]. The linear regime may extend from Rabi frequencies of

only a few MHz to tens of MHz depending on the quantum dot environment, but a nonlinear regime can be identified when $f_{\text{Rabi}} \neq BE_{ac}$ where B is a scaling constant. Although smooth deviation from the linear trend can be seen in direct simulation of Equation 3.1 owing to higher-order terms, the origin of the numerous nonlinear features we observe is unclear. Furthermore, previous works in similar Si/SiGe devices have found Larmor frequency shifts of both signs that are not quadratic in driving amplitude [21, 27], contrary to the theoretical expectation. This leads us to conclude that the model of Eq. 3.1 does not adequately capture all relevant features of the qubit physics.

Anharmonic models of the confinement potential H_0 have been used to explain nonlinear phenomena such as second-harmonic driving [31, 32] and even nonlinear Rabi scaling [33, 34]. However, with both valley splittings of the evaluated device measured to be in excess of 150 μeV, it is unclear why such an anharmonic confinement potential applies to this device. Furthermore, our numerical simulations of Eq. 3.1 with anharmonic orbital- and valley-like models fail to capture the breadth of nonlinear features we observe in experiment (see Appendix 3.C).

It is noteworthy that the EDSR Hamiltonian of Eq. 3.1 with harmonic orbital confinement will exhibit nonlinearity for driving amplitudes which are no longer of a perturbative magnitude with respect to the orbital spacing (see Fig. 3.7). The crosstalk effect will also occur in this regime when multiple driving tones are applied, albeit at larger Rabi frequencies than what we observe in this experiment. Therefore, neither an anharmonic confinement potential nor the phenomenological additions we make to the Hamiltonian in the forthcoming discussion are necessary preconditions for either Rabi frequency nonlinearity or crosstalk. Such modifications to Eq. 3.1 do seem necessary, however, to explain their occurrence at modest Rabi frequencies.

Based on the variety of nonlinearities observed from single-qubit measurements in Fig. 3.2, it is clear that at least the microwave power (P_k) and frequency (ω_k) components are important contributing factors. We therefore focus on the time-dependent driving term of the EDSR Hamiltonian as the simplest source of the nonlinearity and identify two possible physical origins: electric drive distortion and microwave-induced artefacts.

If the signal amplitude at room temperature is not linearly related to the amplitude delivered to the device, then the origin of the nonlinearity may be trivially related to classical electronics or transmission lines. It is not possible for us to measure the electric field at the dot location without considering the electron spin as a sensor itself. Still, we have verified that the output of the IQ-modulated signal is linear with respect to the input. Beyond this element, there are known interference effects in the transmission lines but no active electronic components that are suspected to show nonlinear effects. Furthermore, the signal paths to the “B” and “MW” gates are separate from room temperature, and nonlinearity is present when either gate is used for driving. Conversely, applying a drive through the same gate gives a different nonlinear response depending on which qubit it addresses. This points to a microscopic origin of the nonlinearity, although the driving frequencies and orientations for the two qubits differ as well, making it difficult to completely rule out any origin of nonlinearity from a classical distortion of the driving signal.

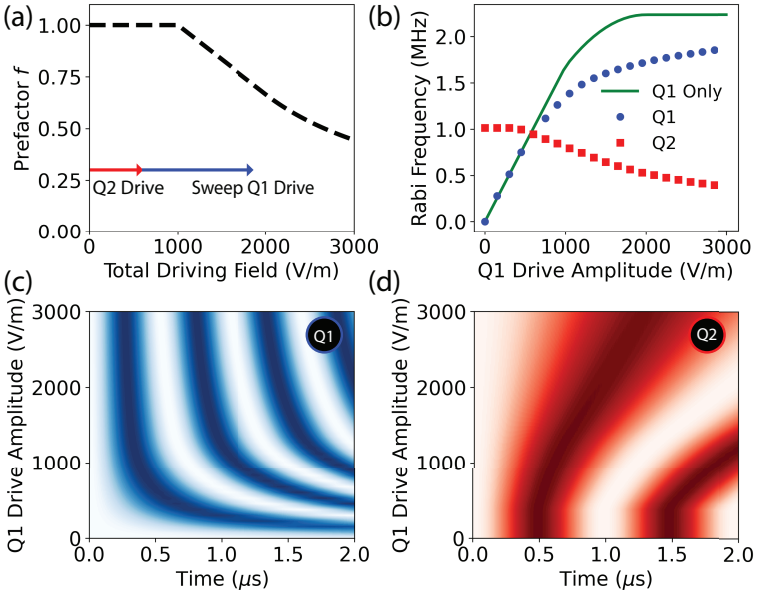

Figure 3.4: (a) Plot showing one possible instance of the phenomenological prefactor describing the nonlinearity in the EDSR mechanism. To illustrate the emergence of crosstalk, we set the Q2 electric drive to a constant amplitude, and manipulate the amplitude of the Q1 drive. The effective driving term in the Hamiltonian will be unique depending on the sum of both microwave drives. (b) The effect of two microwave drives on the two-spin system is numerically simulated with the nonlinear prefactor in (a). The solid green line gives the modified analytic Rabi frequency in the case that only Q1 is driven, while the discrete points are derived by fitting the numerically solved spin dynamics to a sinusoid. (c-d) The spin dynamics of Q1 and Q2 corresponding to the fits in (b). Light and dark regions indicate the probability of measuring a ground or excited state spin respectively. For simulation, we take $E_{Z,\mathrm{Q1}} = 12.066$ GHz, $E_{Z,\mathrm{Q2}} = 11.966$ GHz, $|\vec{b}_{SL}| = 0.3$ mT/nm, $a_0 = \sqrt{\hbar/m^*\omega_0} = 20$ nm, and $E_{ac,Q2} = 600$ V/m.

In Appendix 3.A, we describe how nonlinearity and crosstalk were observed in a different experimental setup using a nominally identical device design. This reinforces the likelihood that the nonlinearity originates at the device and highlights that the nonlinear behaviour is not a peculiarity of a single experimental setup.

Second, we consider the possibility that a microwave drive could influence a quantum dot's confinement potential, and therefore its orbital structure, through heat-induced device strain or the activation of charge traps, for example. Although a true harmonic confinement potential is robust against small perturbations, the anharmonicity introduced by asymmetric confinement or valley-orbit hybridization may be sensitive to such changes [35–37]. We therefore acknowledge the possibility that a nonlinear drive-dependent dipole element $r(E_{\mathrm{tot}}) = \langle VO_0(E_{\mathrm{tot}})|\hat{x}|VO_1(E_{\mathrm{tot}})\rangle$ may manifest in a way that is consistent with our observations. The plausibility of these hypotheses would need to be verified through more rigorous modelling.

Although the origin of the nonlinearity remains uncertain, we can nevertheless gain insight in the crosstalk effect by extending the model of Eq. 3.1 phenomeno-

logically by including a prefactor $f(P_k, \omega_k)$ in the electric driving term such that $E'_{ac}(t)\hat{x} \rightarrow f(P_k, \omega_k)E'_{ac}(t)\hat{x}$. Following from the Rabi scalings measured in Fig. 3.2, we consider the prefactor to be dependent on the power $P_k \propto |E_{ac,k}|^2$ and frequency ω_k of all applied drives. To illustrate the consequences of the phenomenological model, consider the prefactor plotted in Fig. 3.4(a). The prefactor reflects changes in the quantum dot structure, such as a contracted electric dipole, or effective driving field that may manifest as a function of microwave irradiation. Intuitively, the prefactor introduces a "clipping" effect akin to an overdriven amplifier, where an increase in input amplitude no longer leads to a proportional increase in the output EDSR response, i.e. in the Rabi frequency.

To see the importance of this dependence, we numerically integrated the time-dependent Schrödinger equation $i\hbar\dot{\psi} = H(t)\psi$ using Eq. 3.1 and the prefactor depicted in Fig. 3.4(a). A constant driving tone resonant with Q2 drives Rabi oscillations. As a Q1 driving tone is turned on, two notable crosstalk effects occur [Fig. 3.4(b-d)]. First, the Q1 Rabi frequency is substantially smaller than in the case where no Q2 drive is present. Second, the Q2 Rabi frequency decreases markedly as the Q1 Rabi frequency increases. The fitted Rabi frequencies in Fig. 3.4(b) behave analogously to the measured crosstalk effect presented in Fig. 3.3, and the same effect is obtained in the absence of a second electron.

For the near-term scaling of silicon spin qubit devices using micromagnet-based EDSR, the practical issues introduced here can be limited by ensuring the electric drive is oriented parallel to a sufficiently large transverse magnetic gradient. This ensures that a reasonably large f_{Rabi} is achieved at a sufficiently small magnitude of E_{ac} that is within the perturbative limit. Our observations suggest multiplexing qubit control using a linear combination of driving signals is possible within this regime. Emphasis on these design principles may be why nonlinear Rabi scaling was not found to be a control-limiting artefact at few-MHz Rabi frequencies in a more advanced multilayer gate device with possibly tighter confinement potentials [9]. We anticipate that nonlinear effects, including crosstalk, would still appear for faster EDSR driving. Although we cannot provide a conclusive origin for this effect, we believe a more careful consideration of microwave propagation at the device will be fruitful.

3.5. Conclusion

In summary, we have presented experimental evidence of a strong nonlinearity in the fundamental resonance of a single-electron spin qubit controlled by EDSR with a synthetic spin-orbit coupling. To understand both the nonlinear Rabi frequency scaling and crosstalk effects that are observed, we have developed a simple phenomenological model whose accuracy and consequences may be probed through further experiments. The novel crosstalk mechanism introduced here poses important questions for the scalability of spin qubit devices relying on multiplexed single-qubit control.

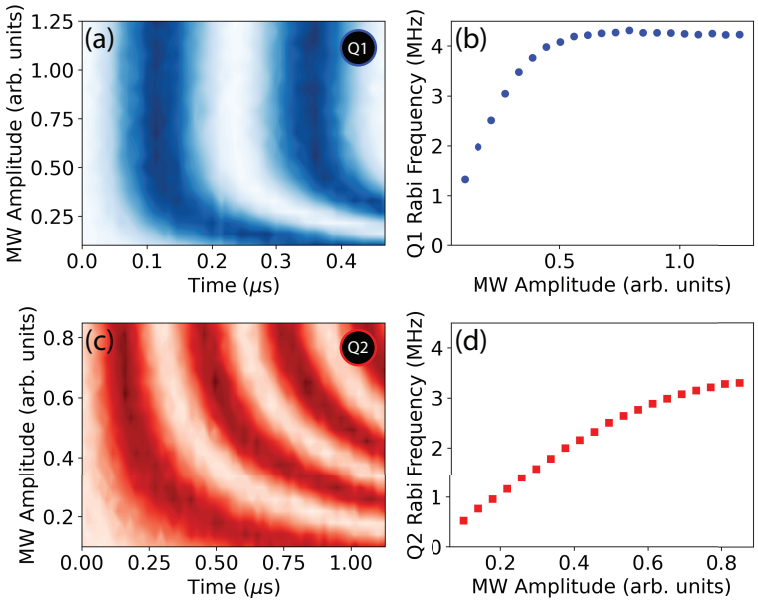

Figure 3.5: Rabi oscillations in Device B. Panels (a) and (c) plot the qubit dynamics as a function of microwave driving amplitude. Panels (b) and (d) show the fitted Rabi frequencies respectively.

3.A. Evidence of nonlinear Rabi scaling in a second device

To provide further evidence that the nonlinear Rabi frequency scaling and crosstalk as discussed in the main text can be seen more generally, we include data collected from a second device - Device B - which is nominally identical with respect to the design in Fig. 3.1(a) - Device A - and is fabricated on the same purified ^{28}Si/SiGe heterostructure. As such, we expect Device B to host quantum dots with a similar orbital confinement and micromagnet gradient as Device A. The Larmor frequencies of Q1 and Q2 of Device B were 15.582 GHz and 15.798 GHz respectively. Device B was cooled in an independent dilution refrigerator and controlled using different electronics than Device A. Rabi oscillations and fitted Rabi frequencies are included in Fig. 3.5. The amplitude scale is independent of that used in the main text.

While both qubits reach the nonlinear regime at modest Rabi frequencies similar to Device A, Q1 of Device B illustrates a striking example of a very flat plateau. As with Device A, there is no immediate evidence of visibility loss or lower Rabi oscillation quality in the plateau region. However, the logical gate fidelities and T_2^{Rabi} were not quantified. Crosstalk, of the kind described in the main text, was also observed in Device B, but not studied systematically like in the case of Device A. The observation of nonlinearity in a second device from an independent setup suggests that the origin of the phenomena can be attributed to the devices, and is less likely the result of a faulty component, for example.

3.B. EDSR IN A HARMONIC CONFINEMENT POTENTIAL

Here we summarize micromagnet-based EDSR with a harmonic confinement potential. We consider the following EDSR Hamiltonian:

$$H(t) = \hbar\omega_0(\hat{a}^\dagger\hat{a} + \frac{1}{2}) + \tilde{E}_{ac}\sin(\omega t)(\hat{a}^\dagger + \hat{a}) - \frac{E_Z}{2}\sigma_z + \tilde{b}_{SL}(\hat{a}^\dagger + \hat{a})\vec{n}\cdot\vec{\sigma}, \tag{3.3}$$

where the position operator $\hat{x} = \sqrt{\frac{\hbar}{2m^*\omega_0}}(\hat{a}^\dagger + \hat{a})$ in terms of the quantum harmonic ladder operators, $m^* = 0.19m_e$ is the in-plane effective mass of the electron in the silicon quantum well, and the spin-dependent terms are as defined in the main text. For the subsequent analysis, the length scale is absorbed in the relevant energy scales such that $\tilde{b}_{SL} = \frac{1}{2}g\mu_B|\vec{b}_{SL}|\sqrt{\hbar/2m^*\omega_0}$ and $\tilde{E}_{ac} = eE_{ac}\sqrt{\hbar/2m^*\omega_0}$. By considering a typical orbital spacing of $\hbar\omega_0 \approx 1$ meV corresponding to a Fock-Darwin radius of $a_0 = \sqrt{\frac{\hbar}{m^*\omega_0}} \approx 20$ nm, an ac electric field amplitude of order less than 10^4 V/m, an external magnetic field of 475 mT, and a transverse magnetic field gradient of 0.5 mT/nm, the relevant terms correspond to the energy scales:

$$\begin{aligned}
\hbar\omega &\approx E_Z,\\
\tilde{b}_{SL} &\approx 1\ \mu\text{eV},\\
\tilde{E}_{ac} &\approx 100\ \mu\text{eV},\\
E_Z &\approx 50\ \mu\text{eV}.
\end{aligned}$$

Therefore:

$$\epsilon \approx \frac{\omega}{\omega_0} \approx \frac{\tilde{b}_{SL}}{\hbar\omega_0} \approx \frac{\tilde{E}_{ac}}{\hbar\omega_0} \approx \frac{E_Z}{\hbar\omega_0} \ll 1, \tag{3.4}$$

and it is appropriate to treat all terms of order ϵ perturbatively with respect to the orbital energy scale. Following the approach of time-dependent Schrieffer-Wolff perturbation theory employed in [28], we derive the effective spin Hamiltonian (ignoring elements proportional to the identity) up to fifth-order as $\tilde{H} = \sum_{n=1}^{5}\tilde{H}^{(n)}$ where:

$$\begin{aligned}
\tilde{H}^{(1)} =& \frac{-E_Z}{2}\sigma_z\\
\tilde{H}^{(2)} =& -\frac{2\tilde{b}_{SL}\tilde{E}_{ac}\cos\theta\sin(\omega t)}{\hbar\omega_0}\sigma_y - \frac{2\tilde{b}_{SL}\tilde{E}_{ac}\sin\theta\sin(\omega t)}{\hbar\omega_0}\sigma_z\\
\tilde{H}^{(3)} =& -\frac{E_Z\tilde{b}_{SL}^2\cos\theta\sin\theta}{\hbar^2\omega_0^2}\sigma_y + \frac{E_Z\tilde{b}_{SL}^2\cos^2\theta}{\hbar^2\omega_0^2}\sigma_z\\
\tilde{H}^{(4)} =& -\frac{\tilde{b}_{SL}\tilde{E}_{ac}\cos\theta(E_Z^2+\hbar^2\omega^2)\sin(\omega t)}{\hbar^3\omega_0^3}\sigma_y - \frac{\tilde{b}_{SL}\tilde{E}_{ac}\sin\theta\omega^2\sin(\omega t)}{\hbar\omega_0^3}\sigma_z\\
\tilde{H}^{(5)} =& -\frac{E_Z\tilde{b}_{SL}^2\cos\theta\sin\theta(E_Z^2+2\tilde{E}_{ac}^2-\tilde{b}_{SL}^2-2\tilde{E}_{ac}^2\cos(2\omega t))}{\hbar^4\omega_0^4}\sigma_y\\
&+\frac{E_Z\tilde{b}_{SL}^2\cos^2\theta(E_Z^2-\tilde{b}_{SL}^2+4\tilde{E}_{ac}^2\sin^2(\omega t))}{\hbar^4\omega_0^4}\sigma_z.
\end{aligned}$$

Expanding the Floquet Hamiltonian and carrying out another second-order Schrieffer-Wolff transformation [28] yields an on-resonance Rabi frequency of:

$$\hbar\Omega_{\text{Rabi}} = \frac{2\tilde{b}_{SL}\tilde{E}_{ac}\cos\theta}{\hbar\omega_0}\left(1+\frac{E_Z^2}{\hbar^2\omega_0^2}\right) \tag{3.5}$$

$$= \frac{g\mu_B a_0^2|\vec{b}_{SL}|\cos\theta e E_{ac}}{2\hbar\omega_0}\left(1+\frac{E_Z^2}{\hbar^2\omega_0^2}\right) \tag{3.6}$$

accurate to $E_Z\epsilon^4$. The drive-dependent frequency shift, analogous to the Bloch-Siegert shift in electron spin resonance, is given as:

$$\hbar\omega_{\text{BSS}} = -\frac{4E_Z\tilde{b}_{SL}^2\tilde{E}_{ac}^2\cos^2\theta}{\hbar^4\omega_0^4} \tag{3.7}$$

$$= -\frac{g^2\mu_B^2 a_0^4 E_Z|\vec{b}_{SL}|^2\cos^2\theta e^2 E_{ac}^2}{4\hbar^4\omega_0^4}. \tag{3.8}$$

The sign of the shift is opposite what is expected from standard ESR. The reason for this is discussed in [28]. The resonance frequency shifts due to a nonlinear Zeeman term and g-factor renormalization are calculated to be, respectively:

$$\hbar\omega_{nlz} = -\frac{2E_Z^3\tilde{b}_{SL}^2\cos^2\theta}{\hbar^4\omega_0^4} \tag{3.9}$$

$$\hbar\omega_g = -\frac{2E_Z\tilde{b}_{SL}^2\cos^2\theta}{\hbar^2\omega_0^2}\left(1-\frac{\tilde{b}_{SL}^2}{\hbar^2\omega_0^2}\right). \tag{3.10}$$

Therefore, a harmonic confinement potential should yield the relations $f_{\text{Rabi}} \propto E_{ac}$ and $\hbar\omega_{\text{BSS}} \propto -E_{ac}^2$ for micromagnet-based EDSR. The perturbative regime used to derive these relations should be valid, for realistic parameters, at least to the order of $f_{\text{Rabi}} = 10$ MHz. It should be noted that nonlinear phenomena, such as second-harmonic driving, are permissible even with perfect harmonic confinement, as evidenced from the presence of longitudinal driving in $\tilde{H}^{(3)}$ and $\tilde{H}^{(5)}$. However, it is believed that nonlinearity originating from anharmonic confinement will be dominant in silicon quantum dots [31].

3.C. EDSR with anharmonic confinement

Here we show how EDSR in the presence of anharmonic confinement, either as a result of a nontrivial potential landscape or the presence of valley-orbit states, permits nonlinear phenomena. However, the nonlinear Rabi scaling found here does not seem to adequately account for the experimental results.

We consider a general two-level orbital subspace acted on by the set of Pauli operators $\{\tau_i\}$, which may describe two hybridized valley-orbit states in silicon, or the lowest two states of an anharmonic confinement potential. Since the micromagnet spin-orbit coupling energy scale is the smallest, we consider the dynamics of the driven orbital sector first. The driven orbital Hamiltonian is:

$$H_0(t) = -\frac{\Delta_0}{2}\tau_z + E'_{ac}\sin(\omega t)\hat{x}, \tag{3.11}$$

where Δ_0 denotes the energy splitting between the ground and excited states and $E'_{ac} = eE_{ac}$ is the scaled electric field as in the main text. The eigenstates of $H_0(t)$ when no drive is present, which we denote as $|\mathrm{VO}_0\rangle$ and $|\mathrm{VO}_1\rangle$, may in general contain both transverse and longitudinal elements, such that:

$$\hat{x} = r\tau_x - p\tau_z, \tag{3.12}$$

where $r = \langle \mathrm{VO}_0|\hat{\mathrm{x}}|\mathrm{VO}_1\rangle > 0$ and $2p = \langle \mathrm{VO}_1|\hat{\mathrm{x}}|\mathrm{VO}_1\rangle - \langle \mathrm{VO}_0|\hat{\mathrm{x}}|\mathrm{VO}_0\rangle$ are real parameters. The parameter p quantifies the extent to which the orbital states have a different centre of mass, as would be the case in an asymmetric confinement potential (see the sketch in Fig. 3.7). We transform the Hamiltonian by an angle $\pi/2 - \theta$ about the τ_y axis, where $\sin\theta = \frac{p}{\sqrt{r^2+p^2}}$:

$$H'_0(t) = \exp(i(\pi/2-\theta)\tau_y)H_0(t)\exp(-i(\pi/2-\theta)\tau_y) \tag{3.13}$$

$$= -\frac{\Delta}{2}\tilde{\tau}_x - \left(\frac{\epsilon + E''_{ac}\sin(\omega t)}{2}\right)\tilde{\tau}_z \tag{3.14}$$

where $\Delta = \Delta_0\cos\theta$, $\epsilon = \Delta_0\sin\theta$, and $E''_{ac} = 2E'_{ac}\sqrt{r^2+p^2}$. Eq. 3.14 is the standard Landau-Zener-Stückelberg Hamiltonian [38]. By moving into the rotating frame using the unitary transformation $\exp(-iE''_{ac}\cos(\omega t)\tilde{\tau}_z/2\omega)$ and applying the Jacobi-Anger expansion, one can distinguish between single-photon transition matrix elements $\Delta J_1(E''_{ac}/\hbar\omega)$ and two-photon transition matrix elements $\Delta J_2(E''_{ac}/\hbar\omega)$ where $J_n(x)$ is the n-th order Bessel function of the first kind. The latter mechanism corresponds to subharmonic driving, when the spin degree of freedom is included perturbatively. An analysis of Eq. 3.14 using the dressed-state formalism in the context of silicon-based EDSR is found in [32].

To illustrate how the Rabi frequency scales in different parameter regimes, we consider the full Hamiltonian numerically for various Δ_0, r, p, E_Z:

$$H(t) = -\frac{\Delta_0}{2}\tau_z + E'_{ac}\sin(\omega t)\hat{x} - \frac{E_Z}{2}\sigma_z + b'_{SL}\hat{x}\sigma_x, \tag{3.15}$$

with all definitions the same as in the main text. In all cases, we choose an initial state in the ground valley-orbit and spin states, and we set $\hbar\omega = E_Z$ for all simulations, neglecting the small g-factor renormalization due to the micromagnet coupling for simplicity. The nominal transverse micromagnet gradient is simulated to be between 0, along the qubit axis, and 0.7 mT/nm along the orthogonal axis. Due to fabrication imperfections and qubit driving likely not taking place along the maximal gradient, we use a value of $|b_{SL}| = 0.3$ mT/nm in simulations. This conservative estimate should underestimate the Rabi frequency at which nonlinearity arises. The small longitudinal gradient can be predicted from the approximately 100 MHz Zeeman difference between the qubit, with an estimated pitch of 100 nm, as 0.04 mT/nm along the qubit axis. Therefore, we neglect any σ_z coupling in the simulation.

In Fig. 3.7, we simulate EDSR mediated by an orbital state with an estimated energy splitting of $\Delta_0 = 1$ meV and a corresponding dipole transition element of

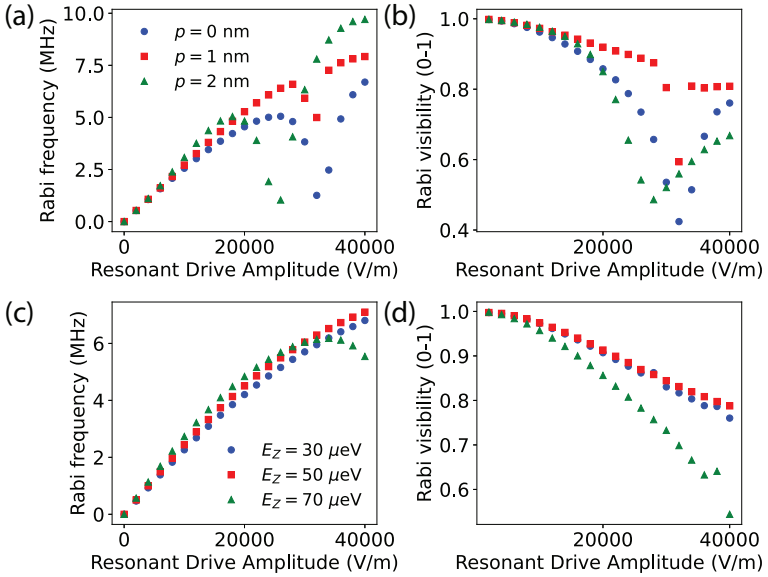

Figure 3.6: (a) Rabi frequency and (b) visibility of valley-mediated EDSR where $\Delta_0 = 150$ μeV, $r = 2$ nm, and $E_Z = 60$ μeV. Different values of p consider different spatial orientations of the excited valley state. (c) Rabi frequency and (d) visibility of valley-mediated EDSR considering different Zeeman splittings where $\Delta_0 = 150$ μeV, $r = 2$ nm, and $p = 0$ nm.

$r = 20/\sqrt{2}$ nm. By changing the parameter p, we effectively model the influence of an asymmetric confinement potential, where the excited state has a shifted centre of mass. Such a skew has negligible influence for a weakly driven spin. Notably, for larger drives ($f_{\text{Rabi}} \gg 10$ MHz) the Rabi frequency deviates below the linear trend predicted by Eq. 3.5 and the visibility decreases due to residual couplings to spin-orbit states outside of the qubit subspace. Such effects have been observed in [8, 23], and may be exacerbated by microwave heating which is not included in our simulations. For considering the phenomenology discussed in the main text, we use this model when $p = 0$ nm and add the prefactor $f(P_k, \omega_k)$ to Eq. 3.3.

In Fig. 3.6(a-b), we probe EDSR when mediated via a valley state. Magnetospectroscopic measurements of the device in our experiment show valley splittings of 180 μeV and 160 μeV for Q1 and Q2 respectively. We note that valley splittings of this magnitude would suggest that there is a relatively small degree of hybridization between orbital and valley degrees of freedom due to interface defects. For our simulations, we select a valley splitting of $\Delta_0 = 150$ μeV and a modest dipole transition element of $r = 2$ nm. An interesting feature appears at the particular Zeeman splitting of $E_Z = 60$ μeV, where both a dip in the Rabi frequency and visibility are found at larger driving amplitudes. The precise driving amplitude where this dip occurs depends on the spatial nature of the valley-like states. We have verified that such a dip can also result in a crosstalk effect, though it qualitatively does not match that observed in experiment.

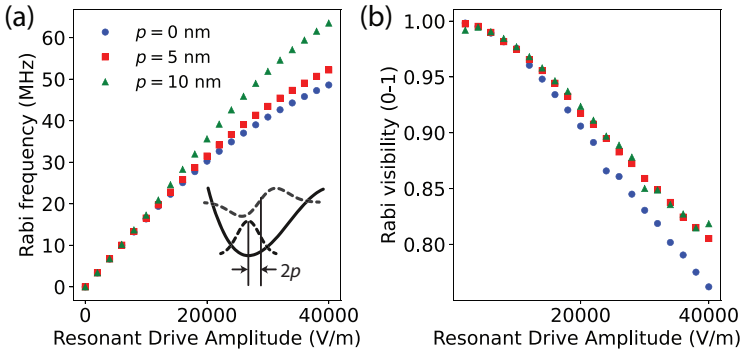

Figure 3.7: (a) Rabi frequency and (b) visibility of orbital-mediated EDSR where $\Delta_0 = 1$ meV, $r = 20/\sqrt{2}$ nm, and $E_Z = 60$ μeV. As no rotating wave approximation is made in the simulation, the spin dynamics are not perfectly sinusoidal and small aberrations in the visibility trend appear. The Rabi frequency is well defined in all cases. As illustrated in the sketch, a larger length p corresponds to a more skewed confinement potential. This results in a different electric dipole which affects the onset of the nonlinear features for strong drives. Nonlinearity in the Rabi frequency scaling becomes apparent when the energy scale of the drive E'_{ac} is no longer of a perturbative magnitude with respect to the orbital spacing Δ_0.

In Fig. 3.6(c-d), we repeat EDSR simulations with a valley-like state with $r = 2$ nm and $p = 0$ nm for different Zeeman splittings similar to those used in experiment. In contrast to orbit-mediated EDSR, there is a notable dependence of the Rabi frequency on E_Z. However, no nonlinearity like that seen in experiment is observed.

References

[1] B. Undseth, X. Xue, M. Mehmandoost, M. Rimbach-Russ, P. T. Eendebak, N. Samkharadze, A. Sammak, V. V. Dobrovitski, G. Scappucci, and L. M. Vandersypen, *Nonlinear response and crosstalk of electrically driven silicon spin qubits,* Phys. Rev. Appl. **19**, 044078 (2023).

[2] L. M. K. Vandersypen, H. Bluhm, J. S. Clarke, A. S. Dzurak, R. Ishihara, A. Morello, D. J. Reilly, L. R. Schreiber, and M. Veldhorst, *Interfacing spin qubits in quantum dots and donnors–hot, dense, and coherent,* npj Quantum Inf. **3**, 34 (2017).

[3] A. Corna, L. Bourdet, R. Maurand, A. Crippa, D. Kotekar-Patil, H. Bohuslavskyi, R. Laviéville, L. Hutin, S. Barraud, X. Jehl, and et al., *Electrically driven electron spin resonance mediated by spin–valley–orbit coupling in a silicon quantum dot,* npj Quantum Inf. **4**, 6 (2018).

[4] W. Huang, M. Veldhorst, N. M. Zimmerman, A. S. Dzurak, and D. Culcer, *Electrically driven spin qubit based on valley mixing,* Phys. Rev. B **95**, 075403 (2017).

[5] E. Kawakami, P. Scarlino, D. R. Ward, F. R. Braakman, D. E. Savage, M. G. Lagally, M. Friesen, S. N. Coppersmith, M. A. Eriksson, and L. M. K. Vandersypen, *Electrical control of a long-lived spin qubit in a Si/SiGe quantum dot,* Nat. Nanotechnol. **9**, 666 (2014).

[6] X. Croot, X. Mi, S. Putz, M. Benito, F. Borjans, G. Burkard, and J. R. Petta, *Flopping-mode electric dipole spin resonance,* Phys. Rev. Res. **2**, 012006(R) (2020).

[7] R. C. C. Leon, C. H. Yang, J. C. C. Hwang, J. C. Lemyre, T. Tanttu, W. Huang, K. W. Chan, K. Y. Tan, F. E. Hudson, K. M. Itoh, and et al., *Coherent spin control of s-, p-, d- and f-electrons in a silicon quantum dot,* Nat. Commun. **11**, 797 (2020).

[8] J. Yoneda, K. Takeda, T. Otsuka, T. Nakajima, M. R. Delbecq, G. Allison, T. Honda, T. Kodera, S. Oda, Y. Hoshi, N. Usami, K. M. Itoh, and S. Tarucha, *A quantum-dot spin qubit with coherence limited by charge noise and fidelity higher than 99.9%,* Nature Nanotech. **13**, 102 (2018).

[9] S. G. J. Philips, M. T. Mądzik, S. V. Amitonov, S. L. de Snoo, M. Russ, N. Kalhor, C. Volk, W. I. L. Lawrie, D. Brousse, L. Tryputen, B. P. Wuetz, A. Sammak, M. Veldhorst, G. Scappucci, and L. M. K. Vandersypen, *Universal control of a six-qubit quantum processor in silicon,* Nature **609**, 919 (2022).

[10] Y. Tokura, W. G. van der Wiel, T. Obata, and S. Tarucha, *Coherent single electron spin control in a slanting Zeeman field,* Phys. Rev. Lett. **96**, 047202 (2006).

[11] M. Pioro-Ladriere, T. Obata, Y. Tokura, Y.-S. Shin, T. Kubo, K. Yoshida, T. Taniyama, and S. Tarucha, *Electrically driven single-electron spin resonance in a slanting Zeeman field,* Nat. Phys. **4**, 776 (2008).

[12] I. Heinz and G. Burkard, *Crosstalk analysis for single-qubit and two-qubit gates in spin qubit arrays,* Phys. Rev. B **104**, 045420 (2021).

[13] M. Sarovar, T. Proctor, K. Rudinger, K. Young, E. Nielsen, and R. Blume-Kohout, *Detecting crosstalk errors in quantum information processors,* Quantum **4**, 321 (2020).

[14] X. Xue, T. F. Watson, J. Helsen, D. R. Ward, D. E. Savage, M. G. Lagally, S. N. Coppersmith, M. A. Eriksson, S. Wehner, and L. M. K. Vandersypen, *Benchmarking gate fidelities in a* Si/SiGe *two-qubit device,* Phys. Rev. X **9**, 021011 (2019).

[15] F. Fedele, A. Chatterjee, S. Fallahi, G. C. Gardner, M. J. Manfra, and F. Kuemmeth, *Simultaneous operations in a two-dimensional array of singlet-triplet qubits,* PRX Quantum **2**, 040306 (2021).

[16] W. I. L. Lawrie, M. Russ, F. van Riggelen, N. W. Hendrickx, S. L. de Snoo, A. Sammak, G. Scappucci, and M. Veldhorst, *Simultaneous driving of semiconductor spin qubits at the fault-tolerant threshold,* (2021), arXiv:2109.07837 .

[17] X. Xue, B. Patra, J. P. G. van Dijk, N. Samkharadze, S. Subramanian, A. Corna, B. Paquelet Wuetz, C. Jeon, F. Sheikh, E. Juarez-Hernandez, and et al., *CMOS-based cryogenic control of silicon quantum circuits,* Nature **593**, 205 (2021).

[18] F. A. Zwanenburg, A. S. Dzurak, A. Morello, M. Y. Simmons, L. C. L. Hollenberg, G. Klimeck, S. Rogge, S. N. Coppersmith, and M. A. Eriksson, *Silicon quantum electronics,* Rev. of Mod. Phys. **85**, 961 (2013).

[19] P. Huang and X. Hu, *Fast spin-valley-based quantum gates in Si with micromagnets,* npj Quantum Inf. **7**, 162 (2021).

[20] X. Xue, M. Russ, N. Samkharadze, B. Undseth, A. Sammak, G. Scappucci, and L. M. K. Vandersypen, *Quantum logic with spin qubits crossing the surface code threshold,* Nature **601**, 343 (2022).

[21] K. Takeda, J. Yoneda, T. Otsuka, T. Nakajima, M. R. Delbecq, G. Allison, Y. Hoshi, N. Usami, K. M. Itoh, S. Oda, T. Kodera, and S. Tarucha, *Optimized electrical control of a Si/SiGe spin qubit in the presence of an induced frequency shift,* npj Quantum Inf. **4**, 54 (2018).

[22] J. Yoneda, T. Otsuka, T. Nakajima, T. Takakura, T. Obata, M. Pioro-Ladriere, H. Lu, C. J. Palmstrom, A. C. Gossard, and S. Tarucha, *Fast electrical control of single electron spins in quantum dots with vanishing influence from nuclear spins,* Phys. Rev. Lett. **113**, 267601 (2014).

[23] K. Takeda, J. Kamioka, T. Otsuka, J. Yoneda, T. Nakajima, M. R. Delbecq, S. Amaha, G. Allison, T. Kodera, S. Oda, and et al., *A fault-tolerant addressable spin qubit in a natural silicon quantum dot,* Science Advances **2**, e1600694 (2016).

[24] T. Nakajima, A. Noiri, K. Kawasaki, J. Yoneda, P. Stano, S. Amaha, T. Otsuka, K. Takeda, M. R. Delbecq, G. Allison, A. Ludwig, A. D. Wieck, D. Loss, and S. Tarucha, *Coherence of a driven electron spin qubit actively decoupled from quasistatic noise,* Phys. Rev. X **10**, 011060 (2020).

[25] E. Kawakami, *Characterization of an electron spin qubit in a Si/SiGe quantum dot*, Ph.D. thesis, TU Delft (2016).

[26] T. Obata, M. Pioro-Ladriere, Y. Tokura, Y.-S. Shin, T. Kubo, K. Yoshida, T. Taniyama, and S. Tarucha, *Coherent manipulation of individual electron spin in a double quantum dot integrated with a micromagnet,* Phys. Rev. B **81**, 085317 (2010).

[27] T. F. Watson, S. G. J. Philips, E. Kawakami, D. R. Ward, P. Scarlino, M. Veldhorst, D. E. Savage, M. G. Lagally, M. Friesen, S. N. Coppersmith, and et al., *A programmable two-qubit quantum processor in silicon,* Nature **555**, 633 (2018).

[28] J. Romhanyi, G. Burkard, and A. Palyi, *Subharmonic transitions and Bloch-Siegert shift in electrically driven spin resonance,* Phys. Rev. B **92**, 054422 (2015).

[29] A. Noiri, K. Takeda, T. Nakajima, T. Kobayashi, A. Sammak, G. Scappucci, and S. Tarucha, *Fast universal quantum gate above the fault-tolerance threshold in silicon.* Nature **601**, 338 (2022).

[30] A. R. Mills, C. R. Guinn, M. M. Feldman, A. J. Sigillito, M. J. Gullans, M. T. Rakher, J. Kerckhoff, C. A. C. Jackson, and J. R. Petta, *High-fidelity state preparation, quantum control, and readout of an isotopically enriched silicon spin qubit,* Phys. Rev. Appl. **18**, 064028 (2022).

[31] P. Scarlino, E. Kawakami, D. R. Ward, D. E. Savage, M. G. Lagally, M. Friesen, S. N. Coppersmith, M. A. Eriksson, and L. M. K. Vandersypen, *Second-harmonic coherent driving of a spin qubit in a Si/SiGe quantum dot,* Phys. Rev. Lett. **115**, 106802 (2015).

[32] P. Scarlino, E. Kawakami, T. Jullien, D. R. Ward, D. E. Savage, M. G. Lagally, M. Friesen, S. N. Coppersmith, M. A. Eriksson, and L. M. K. Vandersypen, *Dressed photon-orbital states in a quantum dot: Intervalley spin resonance,* Phys. Rev. B **95**, 165429 (2017).

[33] D. V. Khomitsky, L. V. Gulyaev, and E. Y. Sherman, *Spin dynamics in a strongly driven system: Very slow rabi oscillations,* Phys. Rev. B **85**, 125312 (2012).

[34] Y. Tokura, T. Kubo, and W. J. Munro, *Power dependence of electric dipole spin resonance,* (2013), arXiv:1308.0071 .

[35] J. K. Gamble, M. A. Eriksson, S. N. Coppersmith, and M. Friesen, *Disorder-induced valley-orbit hybrid states in Si quantum dots,* Phys. Rev. B **88**, 035310 (2013).

[36] P. Boross, G. Szechenyi, D. Culcer, and A. Palyi, *Control of valley dynamics in silicon quantum dots in the presence of an interface step,* Phys. Rev. B **94**, 035438 (2016).

[37] A. Hosseinkhani and G. Burkard, *Electromagnetic control of valley splitting in ideal and disordered si quantum dots,* Phys. Rev. Res. **2**, 043180 (2020).

[38] S. Shevchenko, S. Ashhab, and F. Nori, *Landau–Zener–Stückelberg interferometry,* Phys. Rep. **492**, 1 (2010).

4

Qubit decoherence in a sparse bath of two-level fluctuators

Decades of extensive research have successfully reduced the number of decohering defects in the environment of semiconducting and superconducting qubits, leading to significant improvements in their coherence times. However, the resulting sparse defect environments leads to increased variability of coherence times among qubits in quantum processors. In this chapter, we study qubit decoherence as measured in the Ramsey and Hahn echo experiments, which are caused by a sparse bath of defects producing noise with spectral density $S(f) \sim 1/f$. The defects are modeled as two-level fluctuators, each randomly changing state with a rate γ, that is log-uniformly distributed in $[\gamma_m,\ \gamma_M]$. We find that the bath density, defined as the ratio of the number of TLFs to the logarithmic width of the distribution of rates, is a key parameter in determining the behavior of the system. We confirm that although the noise spectral density remains approximately unchanged, the coherence times become more variable as the bath density decreases. Furthermore, we numerically confirm that in sparse baths, the Ramsey and echo decay times, T_2^* and T_2, are dominated by a few exceptional defects characterized by their rate γ. If the exceptional defects are removed, the coherence times greatly improve. Additionally, we observed that for a narrow distribution of the couplings of two-level fluctuators to the qubit, the Ramsey decay in a sparse bath may exhibit revivals. This study provides new insights into qubit decoherence by realistic $1/f$ noise which could lead to the development of strategies to further improve coherence times.

Author contributions: Contributed to conceiving and implemented the work. This work was conceived and planned by V. V. Dobrovitski, who also participated in the discussion and analysis of the results. Most results of this chapter are published in Ref. [1].

4.1. Introduction

Scaling quantum computers requires large arrays of well-characterized physical qubits with long coherence times, enabling the application of quantum error correction protocols [2, 3]. Noise with spectral density $S(f) \sim 1/f$ poses a significant challenge in scaling up solid-state qubits by reducing their coherence times [4]. For instance, coherence times of semiconductor spin qubits are shortened by charge noise [5–11], while coherence times of various superconducting qubits are limited by both charge and magnetic flux noise [12–17]. All of these noise sources exhibit a $1/f$ dependence in certain frequency ranges of the spectrum [4].

Collective dynamics of a bath of two-level fluctuators (TLFs) is a widely accepted model of $1/f$ noise [18–20]. Any quantum two-level system that undergoes repeated incoherent tunneling between its states can be a TLF [21]. A well-known example is the displacement of an atom or a group of atoms between energetically similar states in a glass [22, 23]. This type of TLFs are present in the glass oxides used as insulators in solid-state qubit devices [8, 24]. A similar mechanism, particular to quantum dot devices, is the trapping and detrapping of charged particles [25]. As another example, the surface spins giving rise to flux noise in superconducting circuits are hypothesized to form clusters that act as TLFs [26, 27].

Although the microscopic origins of $1/f$ noise in solid-state qubit devices are not fully understood, substantial progress has been made in mitigating noise sources in the fabrication stage [8, 28, 29]. For instance, reducing the thickness of the dielectric layer has been shown to decrease charge noise in Si/SiGe quantum dot spin qubits [8], while minimizing the junction area and appropriate surface treatment can reduce charge and flux noise in superconducting qubits [30–32]. Consequently, it is plausible that the $1/f$ noise in current devices arises from a sparse bath of TLFs [10, 33]. In this work, we study qubit decoherence induced by a sparse TLF bath producing noise with $1/f$ spectral density. In general, coupling of a qubit to a bath of TLFs can result in both energy relaxation (T_1) and dephasing (T_2^* and T_2) processes. Here, we focus solely on the qubit dephasing as measured in Ramsey and Hahn echo experiments.

The conventional approach describes the qubit decoherence in terms of the noise (first) spectral density [12, 34–37]. However, the qubit decoherence is uniquely related to the noise spectral density if the noise is a Gaussian random process. Using numerical simulation, we found that the Gaussianity of the $1/f$ noise produced by a TLF bath is determined by the bath density $d = n/w$, where n is the number of TLFs and $w = \ln(\gamma_M/\gamma_m)$ is the logarithmic width of the distribution of TLF rates γ. The $1/f$ noise of a TLF bath becomes a Gaussian random process when $d \to \infty$. We assume the rates, γ, are log-uniformly distributed while the coupling strengths of the TLFs to the qubit, v, are narrowly distributed. These assumptions guarantee the spectral density of both sparse and dense baths to be of the form $S(f) \sim 1/f$. Our study indicates that even though the spectral density of sparse and dense baths are quite similar, the qubit decoherence exhibits large fluctuations across different bath samples when the bath density d is small. Furthermore, we found that the qubit decoherence in a sparse bath is dominated by a small fraction of TLFs characterized by their rates. Below, these TLFs are called exceptional. If

the exceptional TLFs are removed, the coherence times improve substantially.

In addition to the bath density d, the mean coupling strength $\bar{v}$ relative to the minimum and maximum rates, γ_m and γ_M, is of equal importance. The weak and strong coupling regimes are defined by $\bar{v} \lesssim \gamma_m$ and $\bar{v} \gg \gamma_m$, respectively. As γ_M is large, we have excluded the case of $\bar{v} \gtrsim \gamma_M$ from this study. Moreover, we have omitted the echo decay in the weak coupling regime since it produces results similar to the Ramsey decay in the same regime. Therefore, our focus is on studying the Ramsey and echo decay in the strong coupling regime and the Ramsey decay in the weak coupling regime.

This chapter is organized as follows. In Sec. 4.2, we introduce the model used to investigate qubit decoherence by $1/f$ noise of a TLF bath. Section 4.3 presents the Monte Carlo simulations of the model. In Sec. 4.3.1, we demonstrate that qubit decoherence in sparse baths varies significantly among bath samples, despite both sparse and dense baths having a $1/f$ power spectrum. Section 4.3.2 primarily focuses on the impact of exceptional TLFs on qubit decoherence in sparse baths and the substantial improvement achieved by their removal. In Sec. 4.3.3, we show that in the strong coupling regime ($\bar{v} \gg \gamma_m$), the Ramsey decay may exhibit revivals. In Sec. 4.4, we analyze the results by (*i*) discussing why conventional approach of Refs. [12, 34–37] cannot explain the variability in qubit decoherence, and (*ii*) comparing exceptional TLFs with few strongly coupled TLFs that have a similar effect [34]. Finally, in Sec. 4.5, we conclude with remarks on the implications of our findings and suggest directions for future work.

4.2. Model description

We consider a qubit coupled to a bath of non-interacting TLFs. The qubit density matrix may be written as

$$\hat{\rho} = \frac{1}{2}(\mathbf{1} + m_x\hat{\sigma}_x + m_y\hat{\sigma}_y + m_z\hat{\sigma}_z), \tag{4.1}$$

where $\hat{\sigma}_x$, $\hat{\sigma}_y$, and $\hat{\sigma}_z$ are the Pauli matrices, $\mathbf{1}$ is the identity matrix, and m_η with $\eta \in \{x, y, z\}$ are the qubit's Bloch vector components. The qubit is defined using the basis states $|0\rangle$ and $|1\rangle$, which are the eigenstates of the Pauli matrix $\hat{\sigma}_z$.

The qubit dynamics in the presence of the TLF bath is governed by the Hamiltonian

$$\hat{H}(t) = \frac{1}{2}[\nu_0 + \nu(t)]\hat{\sigma}_z + \frac{\Omega(t)}{2}\cos(\nu_0 t + \phi)\hat{\sigma}_x, \tag{4.2}$$

where we have set $\hbar = 1$ for simplicity. Here, ν_0 is the qubit Larmor frequency and $\nu(t)$ represents random modulations of the qubit frequency induced by TLFs. The second term describes the control pulses that implement the qubit rotations required in Ramsey and echo experiments, with the rotation axis specified by ϕ and the rotation angle determined by the area under the envelope $\Omega(t)$. In the frame rotating with angular frequency ν_0 with respect to the lab frame, and within the rotating wave approximation, the qubit Hamiltonian reads

$$\tilde{H}(t) = \frac{\nu(t)}{2}\hat{\sigma}_z + \frac{\Omega(t)}{2}[\cos\phi\hat{\sigma}_x + \sin\phi\hat{\sigma}_y]. \tag{4.3}$$

In the following, we first discuss the details of the TLF bath and then provide explicit expressions for the Ramsey and echo decay using the Hamiltonian in Eq. (4.3).

In general, a TLF is a quantum two-level system coupled to its own environment. A well-known example of a TLF is the spin-boson model, which is used to study the dissipative dynamics of a two-level system in a heat bath [21]. This model has different regimes of behavior. In the incoherent tunneling regime, the two-level system undergoes a series of sudden jumps. A TLF in this work could be thought of as a two-level system in the spin-boson model operating within the incoherent tunneling regime. A TLF can be approximated by a classical random process if the coupling strength to the qubit is smaller than the decoherence rate of the TLF on its own bath [38]. We assume that the TLFs are symmetric, spending equal time in both states on average. Physically, a TLF could be a particle incoherently tunneling or thermally hopping between the minima of a double-well potential [22, 23, 39–41]. For a symmetric TLF, the energy difference ϵ between the minima is zero. At high temperatures, when $k_B T \gg \epsilon$, TLFs with non-zero ϵ become symmetric [42]. We note that other physical systems, such as charge traps near gate electrodes or magnetic impurities, can also behave like TLFs [26, 27, 43–46].

We model each TLF by the classical random process

$$\nu_k(t) = v_k \xi_k(t), \tag{4.4}$$

where $\xi_k(t)$ is a stationary two-state Markov process with the states ± 1 [47], v_k is the coupling strength of the TLF to the qubit, and the index $k = 1, \ldots, n$ labels the TLF. The two-state Markov process is also called random telegraph noise [18]. The autocorrelation function of the two-state Markov process reads

$$\langle \xi_k(0)\xi_k(t)\rangle = e^{-2\gamma_k|t|}, \tag{4.5}$$

where the brackets $\langle ...\rangle$ denote averaging over different realizations of the process, and γ_k is the transition rate from one state of the process to the other.

The TLF rates are samples of the log-uniform distribution

$$P_\Gamma(\gamma) = \frac{1}{w\gamma}, \tag{4.6}$$

with lower and higher cutoffs γ_m and γ_M, respectively. The normalization constant $w = \ln(\gamma_M/\gamma_m)$ is the logarithmic width of the distribution of rates. For clarity, we drop indices whenever possible. Throughout this work, we assume a narrow distribution of coupling strengths $P_V(v)$, either Dirac delta distribution or normal distribution with mean $\bar{v}$ and standard deviation σ_V, satisfying $\sigma_V/\bar{v} \ll \gamma_M/\gamma_m$. We define the bath density d as the ratio of the number of TLFs n to the log-width of the distribution of rates w, i.e.,

$$d = \frac{n}{w}. \tag{4.7}$$

This parameter plays a crucial role in our work, as we observe novel effects in the regime where d is small, and the TLF bath is sparse.

A sample TLF bath is characterized by the set

$$\mathcal{B} = \{(\gamma_1,\ v_1), \ldots, (\gamma_k,\ v_k), \ldots, (\gamma_n,\ v_n)\}, \tag{4.8}$$

where each pair $(\gamma_k,\ v_k)$ for $k = 1, \cdots, n$ represents the jumping rate and the coupling strength of the k-th TLF. As said, these values are samples of the probability densities $P_\Gamma(\gamma)$ and $P_V(v)$. Consequently, the properties of the noise generated by each sample bath and the corresponding qubit decoherence can vary between different bath samples. The total noise produced by a sample TLF bath reads

$$\nu(t) = \sum_k^n \nu_k(t), \tag{4.9}$$

where $\nu_k(t)$, as defined in Eq. (4.4), represents the noise produced by the k-th TLF.

The power spectral density of noise $\nu(t)$ is a useful tool for understanding how the noise power is distributed across different frequencies. It is defined using the statistical properties of the noise, with stationarity playing a crucial role. The spectral density of $\nu(t)$ is expressed as

$$S(\omega) = \lim_{T\to\infty} \frac{1}{T} \left\langle \left| \int_0^T dt\, e^{i\omega t}\, \nu(t) \right|^2 \right\rangle, \tag{4.10}$$

where $\nu(t)$ represents a single realization of the noise, and $\langle \cdots \rangle$ denotes the averaging over different realization of the noise. This expression can be rewritten as

$$S(\omega) = \lim_{T\to\infty} \frac{1}{T} \int_0^T \int_0^T dt' dt''\, e^{i\omega(t''-t')}\, \langle \nu(t')\nu(t'') \rangle. \tag{4.11}$$

Since $\nu_k(t)$ is stationary, the sum $\nu(t) = \sum_k \nu_k(t)$ is also stationary. The statistical properties of a stationary process, such as the autocorrelation function, remain invariant under time shifts. Therefore, for the stationary noise $\nu(t)$, we have

$$\langle v(t')v(t'') \rangle = \langle v(0)v(t''-t') \rangle. \tag{4.12}$$

This implies that the correlation between two values of the process depends only on the time difference $t''-t'$, rather than the specific time points t' and t''. Consequently, the spectral density can be expressed as

$$S(\omega) = \int_{-\infty}^{+\infty} dt\, e^{i\omega t}\, \langle \nu(0)\nu(t) \rangle. \tag{4.13}$$

This expression is often used as the primary definition of power spectral density, in place of Eq. (4.10). The Wiener-Khinchin theorem formally restates this result, though invoking the theorem is not strictly necessary to establish the relationship. The Wiener-Khinchin theorem states that the power spectral density of a wide-sense stationary random process is the Fourier transform of the autocorrelation function, and vice versa [48].

The power spectral density of the noise generated by a single TLF, $\nu_k(t)$, can be calculated as

$$\begin{aligned} S_k(\omega) &= \int_{-\infty}^{+\infty} dt\, e^{i\omega t}\, \langle \nu_k(0)\nu_k(t)\rangle \\ &= v_k^2 \int_{-\infty}^{+\infty} dt\, e^{i\omega t}\, e^{-2\gamma_k|t|} \\ &= \frac{4\gamma_k v_k^2}{4\gamma_k^2+\omega^2}. \end{aligned} \tag{4.14}$$

The power spectral density of the total noise $\nu(t)$ is then

$$S(\omega) = \sum_k^n S_k(\omega). \tag{4.15}$$

Since $S(\omega)$ is a sample of the sum of independent and identically distributed random variables, dividing $S(\omega)$ by n gives the sample mean of the spectral density $S_k(\omega)$. According to the law of large numbers [49], as n increases, this sample mean, if it exists, converges to the true mean of $S_k(\omega)$. In other words,

$$\begin{aligned} \lim_{n\to\infty} \frac{1}{n}\sum_k^n S_k(\omega) &= \int_{v_m}^{v_M}\int_{\gamma_m}^{\gamma_M} dv\, d\gamma\, P_V(v)\, P_\Gamma(\gamma)\, \frac{4\gamma v^2}{\omega^2+4\gamma^2} \\ &= \frac{2\,\bar{v^2}}{w\,\omega}[\arctan(2\gamma_M/\omega) - \arctan(2\gamma_m/\omega)], \end{aligned} \tag{4.16}$$

where

$$\bar{v^2} = \int_{v_m}^{v_M} dv\, P_V(v)\, v^2, \tag{4.17}$$

is the variance of noise generated by a single TLF, and v_m and v_M represent the minimum and maximum values of the coupling strength, respectively. It should be noted that the limit $n \to \infty$ is useful for obtaining the analytical estimates of the noise spectral density. However, in practice, the number of TLFs n can be large but not infinite in the strict mathematical sense.

The power spectral density provides a tool for analyzing the spectral components of noise, allowing us to identify regions where the noise behaves as white noise (constant power across frequencies) or colored noise (power concentrated in specific frequency bands). Asymptotic expansions of the spectral density

$$S(\omega) = \frac{2\,n\,\bar{v^2}}{w\,\omega}\left[\arctan(2\gamma_M/\omega) - \arctan(2\gamma_m/\omega)\right], \tag{4.18}$$

in the low ($\omega \ll \gamma_m$), intermediate ($\gamma_m \ll \omega \ll \gamma_M$), and high ($\omega \gg \gamma_M$) frequency regimes provide simple representations of the distribution of noise power across different frequencies. Using the trigonometric identity

$$\arctan(z) + \arctan\left(\frac{1}{z}\right) = \frac{\pi}{2}, \tag{4.19}$$

and the Taylor series expansion of the arctangent function,

$$\arctan(z) = z - \frac{z^3}{3} + \mathcal{O}(z^5), \tag{4.20}$$

which is convergent for $|z| \leq 1$, except for $z = \pm i$, one obtains

$$\arctan(y) = \frac{\pi}{2} - \frac{1}{y} + \frac{1}{3y^3} + \mathcal{O}(y^{-5}), \tag{4.21}$$

where $y = 1/z$. Equations (4.20) and (4.21) allow us to analyze the asymptotic behavior of the arctangent function for small and large arguments, respectively. In the low-frequency limit ($\omega \ll \gamma_m$), both arguments of the arctangent functions in Eq. (4.18) are large ($2\gamma_M/\omega \gg 1$ and $2\gamma_m/\omega \gg 1$). Using Eq. (4.21), the spectral density simplifies to a constant value, corresponding to the white noise spectrum of $\nu(t)$ at low frequencies. For intermediate frequencies ($\gamma_m \ll \omega \ll \gamma_M$), $2\gamma_M/\omega \gg 1$ while $2\gamma_m/\omega \ll 1$. Using the Taylor expansion of $\arctan(2\gamma_m/\omega)$ for small argument and expanding $\arctan(2\gamma_M/\omega)$ using Eq. (4.21), the spectral density simplifies to

$$S(\omega) \propto \frac{1}{\omega}, \tag{4.22}$$

characteristic of $1/f$ noise [19]. In the high-frequency limit ($\omega \gg \gamma_M$), $2\gamma_M/\omega \ll 1$ and $2\gamma_m/\omega \ll 1$. Using the Taylor series expansion for both arctangent terms, the spectral density simplifies to $S(\omega) \propto 1/\omega^2$.

Returning to system Hamiltonian in Eq. (4.3), we now provide explicit expressions for the qubit dephasing in a TLF bath as measured in the Ramsey and Hahn echo experiments. We assume the control pulses are extremely short, such that the application of a pulse instantly rotates the qubit [50]. In the Ramsey experiment, the qubit is initialized in the state $m_x = 1$, and after freely evolving for the delay time t is measured in the x basis. The echo experiment is similar, except for a π rotation interjecting the free evolution time at $t/2$ [51]. Since the TLFs are symmetric, the total noise has zero mean, and the noise-averaged Bloch vector component $\langle m_y(t)\rangle$ remains zero while the qubit undergoes dephasing. The phase coherence as measured in the Ramsey/Hahn echo experiments is therefore $F_{R/H}(\mathcal{B};t) = \langle m_x(t)\rangle$. The qubit phase in the Ramsey experiment may be written as

$$F_R(\mathcal{B};t) = \langle \exp[i \int_0^t ds\nu(s)]\rangle. \tag{4.23}$$

Since the pulses are assumed to rotate the qubit instantaneously, the π pulse in the echo experiment effectively changes the sign of the noise. Therefore, the echo decay may be obtained via

$$F_H(\mathcal{B};t) = \langle \exp[i \int_0^{t/2} ds\nu(s) - i \int_{t/2}^t ds\nu(s)]\rangle. \tag{4.24}$$

Since the TLFs are independent and $\nu(t) = \sum_k^n \nu_k(t)$, the Ramsey/Hahn echo signal for a qubit coupled to a sample bath $\mathcal{B}$ is the product

$$F_{R/H}(\mathcal{B};t) = \prod_k^n f_{R/H}^{(k)}(\gamma_k, v_k; t), \tag{4.25}$$

where $f^{(k)}_{R/H}(t)$ is the Ramsey/Hahn echo decay induced by the k-th fluctuator. Explicit expressions for the Ramsey and echo decay induced by a single fluctuator are [42, 44, 52, 53]

$$f_R(\gamma, v; t) = e^{-\gamma t}(\cosh \alpha t + \frac{\gamma}{\alpha} \sinh \alpha t), \tag{4.26}$$

and

$$f_H(\gamma, v; t) = e^{-\gamma t}(\frac{\gamma^2}{\alpha^2} \cosh \alpha t + \frac{\gamma}{\alpha} \sinh \alpha t - \frac{v^2}{\alpha^2}), \tag{4.27}$$

where, $\alpha = \sqrt{\gamma^2 - v^2}$. In this work, the Ramsey and echo coherence times, denoted by T_2^* and T_2, respectively, are defined via

$$F_{H(R)}(\mathcal{B}; T_2^{(*)}) = 1/e. \tag{4.28}$$

4

It is useful to recall that if the zero-mean stationary noise $\nu(t)$ is a Gaussian random process, it is fully characterized by the power spectral density $S(\omega)$ (see Ch. 2). This follows from the cumulant expansion for Gaussian processes, where all cumulants of order higher than two are zero. The first and second-order cumulants of a random process correspond to its mean and autocorrelation function, respectively. In this work, we consider the general situation where $\nu(t)$ is not necessarily Gaussian. Therefore, the qubit decoherence induced by such a noise is not always fully described by the noise power spectral density $S(\omega)$. This motivates the use of exact expressions given by Eq. (4.25), instead of the spectral density, for describing the qubit decoherence. Furthermore, the average of $S(\omega)$ for any number of TLFs n, even if n is not large, matches the expression in Eq. (4.18). This indicates that $S(\omega)$ is a self-averaging quantity.

4.3. Numerical simulation results

To numerically compute the Ramsey/echo decay in a given bath sample $\mathcal{B}$, we generate a list of TLF rates and coupling strengths as given in Eq. (4.8). We obtain the modified bath sample, denoted by $\tilde{\mathcal{B}}$, by eliminating the pairs of $(\gamma,\ v)$ corresponding to exceptional defects, specified in Sec. 4.3.2. The Ramsey/echo decay in a given bath sample, either original $\mathcal{B}$ or modified $\tilde{\mathcal{B}}$, is then calculated using Eqs. (4.25), (4.26), and (4.27). This procedure constitutes the main part of the algorithms used for our numerical simulations.

4.3.1. Variability of qubit decoherence

Figure 4.1 presents the numerically computed spectral densities of noise generated by different TLF bath samples. In both panels, the coupling strengths are distributed according to $P_V(v) = \delta(v - \bar{v})$, excluding the possibility of pronounced Lorentzian peaks from individual TLFs in the spectrum. The values of γ_m and γ_M, which define the lower and upper cutoffs, are held constant across all spectra. In Fig. 4.1(a), the number of TLFs n is varied, resulting in bath densities of $d < 1$, $d \sim 1$, and $d > 1$ for small, intermediate, and large values of n, relative to the logarithmic width of the rate distribution $w = \ln(\gamma_M/\gamma_m)$. Notably, the spectral densities of both sparse

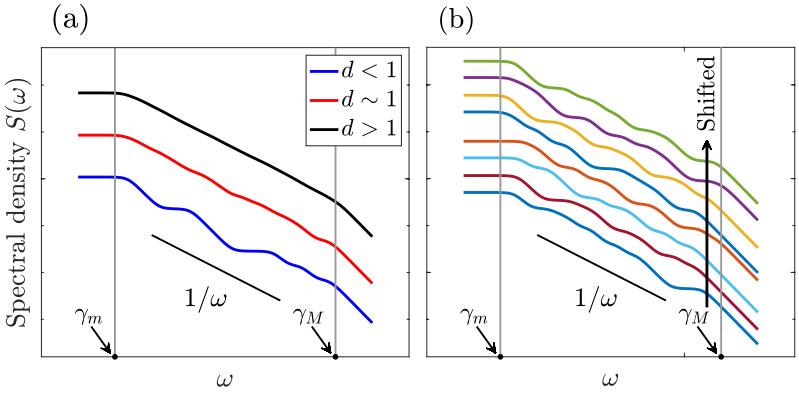

Figure 4.1: Simulated spectral densities of the noise generated by bath samples of varying density d. Both panels (a) and (b) have the same ratio of $\gamma_M/\gamma_m = 10^9$, motivated by experimental observations of $1/f$ noise in semiconductor spin qubit devices, which can span several decades in frequency (see, for instance, Refs. [7, 11]). The noise variance $n\bar{v}^2 = \gamma_m^2$ is the same for all plotted spectra, but the spectra are shifted vertically for clarity. The horizontal and vertical axes in both plots are scaled logarithmically (log-log plots). (a) Spectral densities of sample baths with different values of d. The number of TLFs for the blue, red, and black curves are respectively $n = 5,\ 30,\ 1000$, while the ratio $\gamma_M/\gamma_m = 10^9$ remains constant, resulting in bath densities of $d \approx 0.18,\ 1.08,\ 36.19$. (b) Spectral densities of sparse sample baths with fixed values of $n = 10$ and $d \approx 0.36$. Each colored curve represents a specific sample of the spectral density of the TLF bath, characterized by the set $\mathcal{B}$ given in Eq. (4.8).

$(d < 1)$ and dense $(d > 1)$ bath samples are quite similar, with minimal wiggles introduced by individual TLFs. In particular, a $1/f$ dependence is observed between the lower and upper cutoffs, even for $d < 1$. Here, the noise variance $n\bar{v}^2$ is kept constant, but the sample spectra are shifted vertically for clarity. Figure 4.1(b) shows multiple samples of the spectral density for sparse baths, with all system parameters held fixed. While the precise location of the wiggles varies between samples, the general $1/f$ scaling of the spectra remains consistent across samples.

As shown in Fig. 4.2, the behavior of the Ramsey decay $F_R(\mathcal{B}; t)$ in sparse and dense baths is distinct from the noise spectra. Figure 4.2(a) shows the Ramsey decay in a few sparse bath samples with a fixed small density d, revealing that the qubit decoherence varies significantly among different bath samples. In contrast, Fig. 4.2(b) shows the Ramsey decay for a few dense bath samples with a fixed large density d. Here, the Ramsey decay only exhibits subtle variations between the different bath samples. The probability density functions (p.d.f.'s) of the Ramsey decay $F_R(\mathcal{B}; t)$ for sparse and dense baths are estimated in Figs. 4.2(c) and 4.2(d), respectively. These panels are pixelated, and a vertical column of pixels is a histogram showing the estimated p.d.f. of $F_R(\mathcal{B}; t)$ at a specific value of $\gamma_m t$. The color intensity represents the relative number (fraction) of the qubits having a specific value of $F_R(\mathcal{B}; t)$ [or $F_H(\mathcal{B}; t)$ in remainder of the text] at a specific value of $\gamma_m t$. The estimated p.d.f.'s demonstrate that for small d, the qubit decoherence is subject to large variations, while for large d, the decoherence only varies slightly.

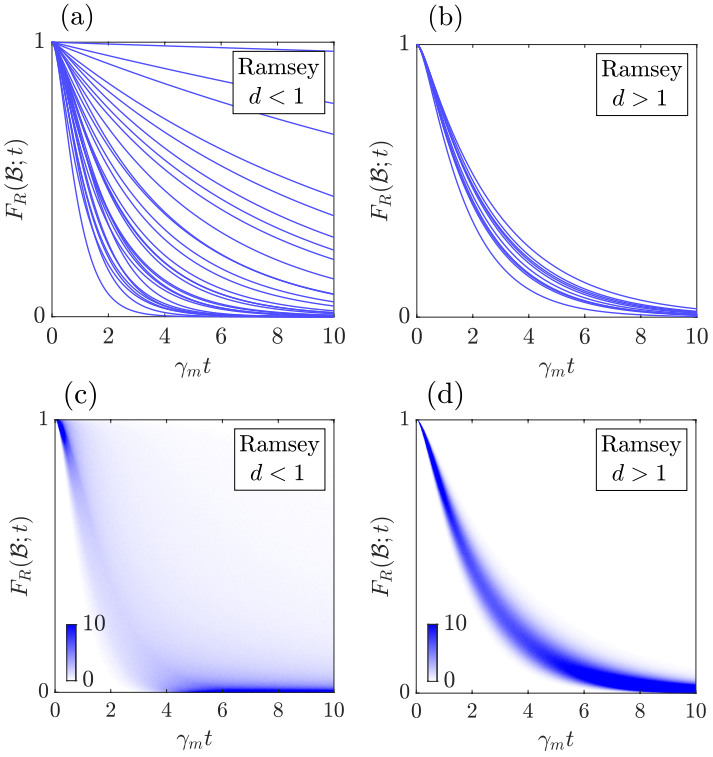

Figure 4.2: Ramsey decay in the weak coupling regime for sparse versus dense baths. The ratio $\gamma_M/\gamma_m = 10^5$ is fixed in all panels. (a) Ramsey decay in 30 sparse bath samples with $n = 10$ and $d \approx 0.87$, where the coupling strengths are distributed according to $P_V(v) = \delta(v - \bar{v})$ with $\bar{v} = \gamma_m$. (b) Ramsey decay in 10 dense bath samples with $n = 160$ and $d \approx 13.9$, where the coupling strengths are distributed according to $P_V(v) = \delta(v - \bar{v})$ with $\bar{v} = \gamma_m/4$, ensuring that the noise variance $n\bar{v}^2$ remains the same as in (a). (c)-(d) Histograms estimating p.d.f.'s of Ramsey decay $F_R(\mathcal{B};t)$ corresponding to parameter values in (a)-(b). Each panel has a resolution of $10^3 \times 10^3$ pixels, and a vertical column of 10^3 pixels at a given time t represents a histogram of 10^5 samples of $F_R(\mathcal{B};t)$. The number of counts in each pixel is divided by 100 to estimate the probability density of $F_R(\mathcal{B};t)$. The estimated p.d.f. values smaller than 10 are linearly mapped to the color bar, while those greater than or equal to 10 are mapped to the darkest shade in the color bar.

The same behavior can be seen for the echo decay $F_H(\mathcal{B};t)$. Figures 4.3(a) and 4.3(b) compare the echo decay in sparse and dense baths. The echo decay in sparse bath samples with a fixed small density d varies again largely among the different bath samples. In contrast, the echo decay in dense bath samples with a fixed large density d only slightly varies between the different bath samples. The estimated p.d.f.'s of the echo decay $F_H(\mathcal{B};t)$ for sparse and dense baths are shown in Figs. 4.3(c) and 4.3(d), respectively.

These simulations indicate that the qubit decoherence is strongly influenced by the density of the TLF bath d, with significant differences observed between sparse and dense baths. Although the spectral densities of both types of baths exhibit a

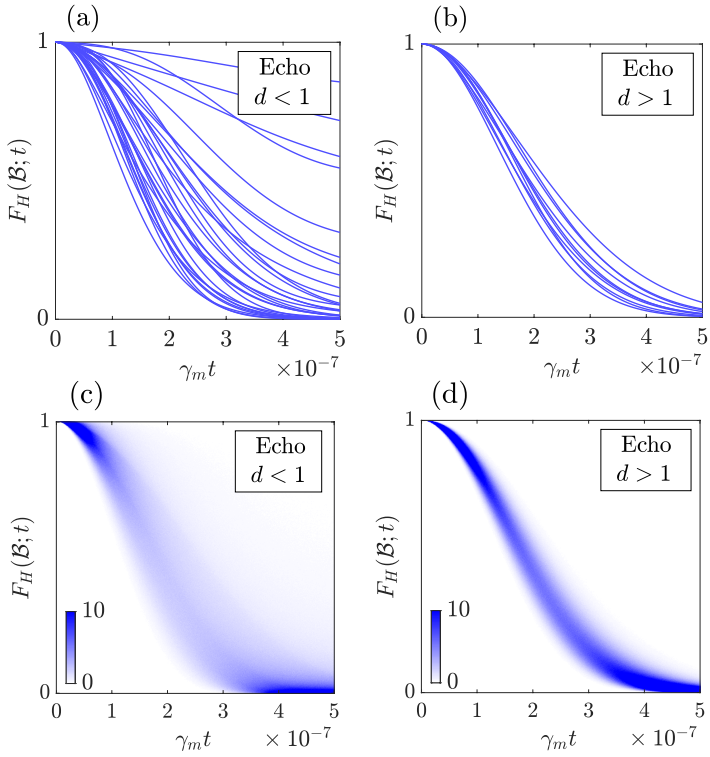

Figure 4.3: Echo decay in sparse versus dense baths. For all panels, the ratio $\gamma_M/\gamma_m = 10^{12}$ is fixed. (a) Echo decay in 30 sparse bath samples with $n = 16$ and $d \approx 0.58$. The coupling strengths are distributed according to $P_V(v) = \delta(v - \bar{v})$, with $\bar{v} = \gamma_m \times 10^7$. (b) Echo decay in 10 dense bath samples with $n = 100$ and $d \approx 3.62$. We plotted fewer samples than in (a) for clarity. The coupling strengths are distributed according to $P_V(v) = \delta(v - \bar{v})$, with $\bar{v} = 4\gamma_m \times 10^6$, so that the noise variance $n\bar{v}^2$ remains the same as in (a). (c)-(d) Histograms estimating p.d.f.'s of echo decay $F_H(\mathcal{B};t)$ corresponding to parameter values in (a)-(b). Details of the histograms are the same as in Fig. 4.2(c).

$1/f$ dependence with minimal wiggles from individual TLFs, the variability of qubit decoherence is much greater in sparse baths than in dense ones. It is important to note that this feature is dependent not only on the bath density d but also on the coupling regime. The large variability occurs for Ramsey decay in the weak coupling regime and echo decay in the strong coupling regime, but not for Ramsey decay in the strong coupling regime. Simulation results for the Ramsey decay in the strong coupling regime are presented separately in Sec. 4.3.3.

4.3.2. Improvements by removing exceptional defects

A special feature of sparse baths is the occurrence of exceptional defect, a single TLF that dominates the qubit decoherence. An exceptional defect is identified as the TLF whose jumping rate γ is closest to the mean coupling strength $\bar{v}$. The

question is whether removing exceptional defects can improve the coherence times. By removing only a fraction of these defects one can greatly improve coherence times. We demonstrate this improvement for both an infinitely narrow distribution of coupling strengths and a normal distribution with a small standard deviation. In both cases, removing exceptional defects leads to similar improvements in coherence times.

Figure 4.4 shows the qualitative improvement in Ramsey decay by removing exceptional defects. Specifically, Fig. 4.4(a) shows the Ramsey decay over multiple bath samples with a fixed small density d. The original bath samples consist of 12 TLFs. These baths are modified by removing only two exceptional TLFs. The original and modified baths are denoted by $\mathcal{B}$ and $\tilde{\mathcal{B}}$, respectively. The Ramsey decay over the original and modified baths, is shown in blue and red curves, respectively. Figure 4.4(b) illustrates that the improvement in Ramsey decay due to removal of the exceptional defects is accompanied by a shuffling effect; the order of Ramsey decays in terms of their coherence times is not preserved when the baths are modified. Figures 4.4(c) and (d) are histograms estimating the probability densities of Ramsey decay in the original and modified baths, respectively.

In Fig. 4.5, we quantify the improvement of Ramsey decay by eliminating the exceptional defects, using the same parameters as in Fig. 4.4. We benchmark the improvement using the *coherence fidelity*, which is the amplitude of Ramsey decay $F_R(\mathcal{B};t)$ at a specific time t, and the coherence time T_2^*. Figure 4.5(a) displays the estimated probability densities of the coherence fidelity for the original and modified baths. To determine the fraction of qubits with coherence fidelities above a certain value, we use the complementary cumulative distribution function (c.c.d.f.) defined as $\bar{F}_X(x) = \int_x^\infty P_X(u)du$ for a random variable X with sample x and probability density $P_X(x)$. By removing 2 exceptional defects, the fraction of qubits with coherence fidelity above 90% at time $t = 1/\gamma_m$ improves by ≈ 7.7, as shown in Fig. 4.5(b). Figures 4.5(c) and (d) show the estimated p.d.f. and c.c.d.f. of T_2^* for the original and modified baths. We see that the fraction of qubits with $T_2^* \geq 20/\gamma_m$ improves by ≈ 14.

Figure 4.6 shows the qualitative improvement in echo decay by removing exceptional defects. Figure 4.6(a) shows the echo decay over multiple bath samples with a fixed small density d. The original bath samples, consisting of 20 TLFs, were modified by removing only two exceptional TLFs. The original and modified baths are again denoted by $\mathcal{B}$ and $\tilde{\mathcal{B}}$, while the blue and red curves represent the echo decay over the original and modified baths. We observe in Figs. 4.6(a) and (b) that the removal of exceptional defects leads to a significant improvement in echo decay. Figures. 4.6(c) and (d) are histograms estimating the probability densities of echo decay in the original and modified baths.

In Fig. 4.7, we quantitatively investigate the impact of eliminating exceptional defects on the echo decay, using the same parameters as in Fig. 4.6. Figure 4.7(a) and (b) show the estimated p.d.f. and c.c.d.f. of the coherence fidelity for the original and modified baths. Removing two exceptional defects enhances the fraction of qubits with coherence fidelity above 90% at time $t = 10^{-6}/\gamma_m$ by ≈ 3.9 [see Fig. 4.7(b)]. The estimated p.d.f. and c.c.d.f. of T_2 for the original and modified baths show that

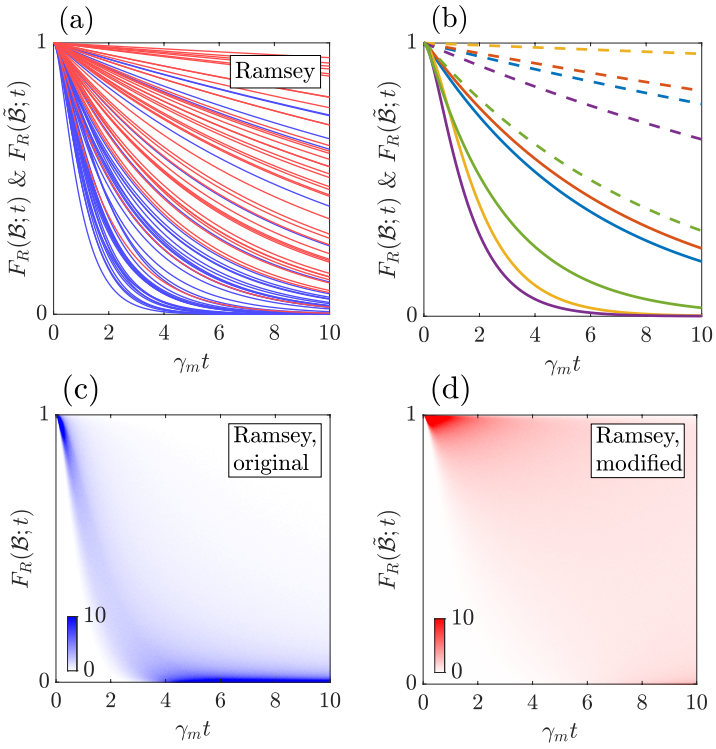

Figure 4.4: Improvement of Ramsey decay by removal of exceptional defects. (a) Ramsey decay over 40 bath samples (blue curves) with $\gamma_M/\gamma_m = 10^5$ and $n = 12$, giving $d \approx 1.04$. The coupling strengths are distributed according to $P_V(v) = \delta(v-\bar{v})$ with $\bar{v} = \gamma_m$. Each bath sample is modified by removing two TLFs with the smallest rates. Ramsey decay over modified baths is shown in red curves. (b) Ramsey decay over 5 bath samples with the same parameters as in (a). Solid/dashed curves show Ramsey decay over original/modified bath samples. Ramsey decay in the original and the corresponding modified bath have the same color. (c) and (d) Histograms estimating p.d.f.'s of $F_R(\mathcal{B};t)$ and $F_R(\tilde{\mathcal{B}};t)$ corresponding to parameter values in (a). Details of the histograms are the same as in Fig. 4.2(c).

the fraction of qubits with $T_2 \geq 4 \times 10^{-6}/\gamma_m$ improves by ≈ 7.5 [see Figs. 4.7(c) and (d)].

Since an infinitely narrow distribution of coupling strengths is unrealistic, we now check whether exceptional defects have similar impacts for a more realistic distribution of couplings. For this purpose, we consider a normal distribution of coupling strengths characterized by the mean value $\bar{v}$ and the standard deviation σ_V. To ensure a narrow distribution of coupling strengths, we impose the condition that the ratio of σ_V to $\bar{v}$ is much smaller than the ratio of the maximum to minimum rates, i.e.,

$$\frac{\sigma_V}{\bar{v}} \ll \frac{\gamma_M}{\gamma_m}. \tag{4.29}$$

This prevents the introduction of pronounced Lorentzian peaks into the spectrum

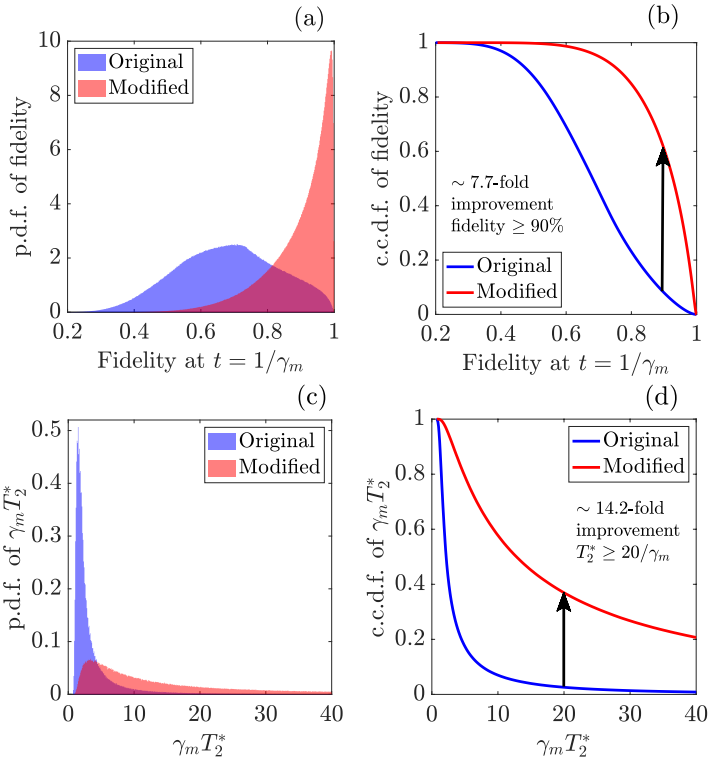

Figure 4.5: Quantified improvement of Ramsey decay by removal of exceptional defects. The system parameters are the same as in Fig. 4.4. (a) P.d.f.'s of fidelity at time $t = 1/\gamma_m$ for the original and modified baths. (b) C.c.d.f.'s of fidelity at time $t = 1/\gamma_m$ for the original and modified baths. The fraction of qubits with fidelity above 90% has approximately a 7.7-fold improvement. (c) P.d.f.'s of T_2^* for original and modified baths. (d) C.c.d.f.'s of T_2^* for original and modified baths. The fraction of qubits with coherence times $T_2^* \geq 20/\gamma_m$ improves approximately by a factor of 14.2.

that may occur if few TLFs with large coupling strengths are present on the tail of a wide distribution. Otherwise, the spectral density is substantially altered and deviates from the $1/f$ scaling with frequency between the lower and higher cutoffs. Figures 4.8 and 4.9 show the improvements of Ramsey and echo decay by removing exceptional defects, considering a normal distribution of coupling strengths. These results are qualitatively and quantitatively comparable to our previous findings for an infinitely narrow distribution of coupling strengths.

4.3.3. Revivals of Ramsey decay

Ramsey decay exhibits revivals in the strong coupling regime when the bath is sparse and the coupling strengths are narrowly distributed. However, these revivals disappear when the distribution of coupling strengths is wide, as shown in Fig. 4.10 through numerical simulations. We consider normally distributed coupling strengths

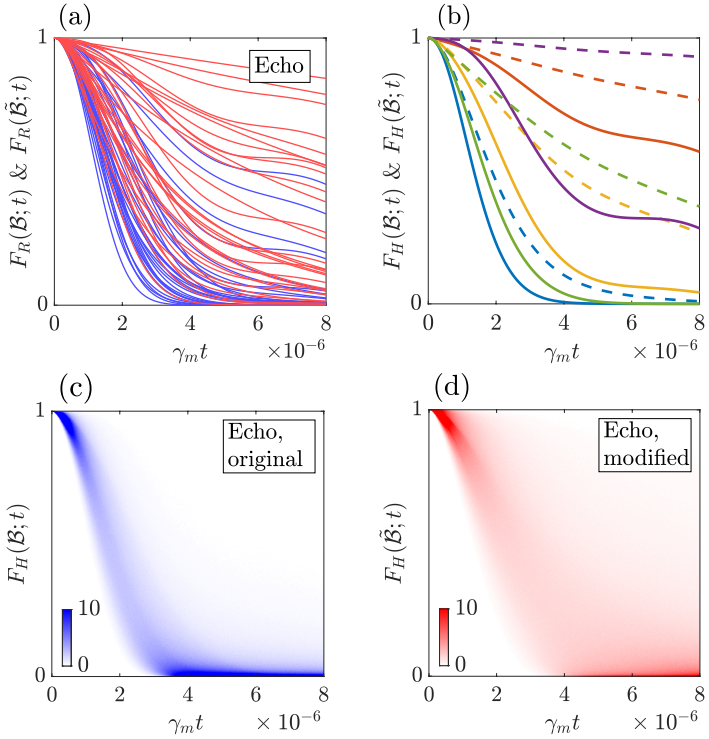

Figure 4.6: Improvement of echo decay by removal of exceptional defects. (a) Echo decay over 30 bath samples (blue curves) with $\gamma_M/\gamma_m = 10^{12}$ and $n = 20$, giving $d \approx 0.72$. The coupling strengths are distributed according to $P_V(v) = \delta(v - \bar{v})$ with $\bar{v} = \gamma_m$. Each bath sample is modified by removing two TLFs with the rates γ closest to $\bar{v}$. Ramsey decay over modified baths is shown in red curves. (b) Ramsey decay over 5 bath samples with the same parameters as in (a). Solid/dashed curves show Ramsey decay over original/modified bath samples. Ramsey decay in the original and the corresponding modified bath have the same color. (c) and (d) Histograms estimating p.d.f.'s of $F_H(\mathcal{B};t)$ and $F_H(\tilde{\mathcal{B}};t)$ corresponding to parameter values in (a). Details of the histograms are the same as in Fig. 4.2(c).

with mean $\bar{v}$ and deviation σ_V. Figure 4.10(a) shows the Ramsey decay for a fixed small density d and a wide distribution of coupling strengths, while the inset shows the Ramsey decay for a narrow distribution of coupling strengths. The corresponding histograms in Fig. 4.10(b) and its inset estimate the p.d.f.'s of the Ramsey decay $F_R(\mathcal{B};t)$ for wide and narrow distributions of coupling strengths. We see a revival with a peak at $\pi/\bar{v}$ for the narrow distribution, while in the case of wide distribution, the revivals are averaged out.

4.4. Discussion

We showed in Sec. 4.3.1 that decreasing the bath density d increases the variability of qubit decoherence while maintaining a $1/f$ spectral density. This greatly limits the applicability of the filter function formalism [12, 34–37] in describing qubit

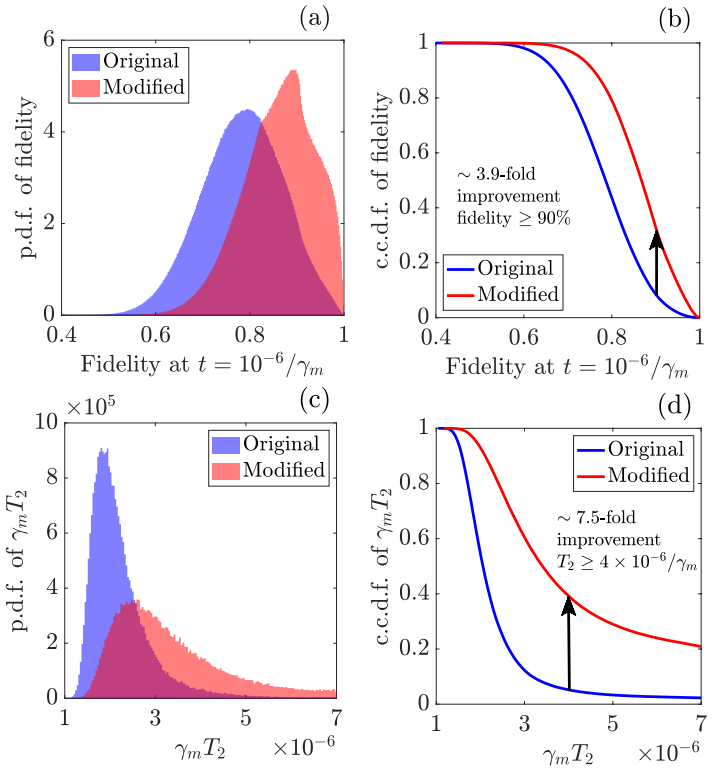

Figure 4.7: Quantified improvement of Ramsey decay by removal of exceptional defects. The system parameters are the same as in Fig. 4.6. (a) P.d.f.'s of fidelity at time $t = 10^{-6}/\gamma_m$ for the original and modified baths. (b) C.c.d.f.'s of fidelity at time $t = 10^{-6}/\gamma_m$ for the original and modified baths. The fraction of qubits with fidelity above 90% has approximately a 3.9-fold improvement. (c) P.d.f.'s of T_2 for original and modified baths. (d) C.c.d.f.'s of T_2 for original and modified baths. The fraction of qubits with coherence times $T_2 \geq 4 \times 10^{-6}/\gamma_m$ improves approximately by a factor of 7.5.

decoherence in sparse baths. The filter function formalism describes the qubit decoherence within the Gaussian approximation of the environmental noise. It relates the Ramsey and echo decay to the noise first spectral density $S(\omega)$ via

$$F_{R/H}[S(\omega);\ t] = \exp[-\frac{1}{2}\int d\omega S(\omega)\frac{G_{R/H}(\omega t)}{\omega^2}], \tag{4.30}$$

where $G_R(\omega t) = 2\sin^2\frac{\omega t}{2}$ and $G_H(\omega t) = 8\sin^4\frac{\omega t}{4}$ are the Ramsey and echo filter functions, respectively [35]. This equation allows for describing the qubit dynamics without requiring knowledge of the environment's microscopic details. One can also use Eq. (4.30) to characterize the environmental noise from the qubit's dynamics. However, it is important to note that Eq. (4.30) only provides partial information about the environmental noise since it is not known a priori whether the noise is a Gaussian random process. The first spectral density $S(\omega)$ can only fully characterize

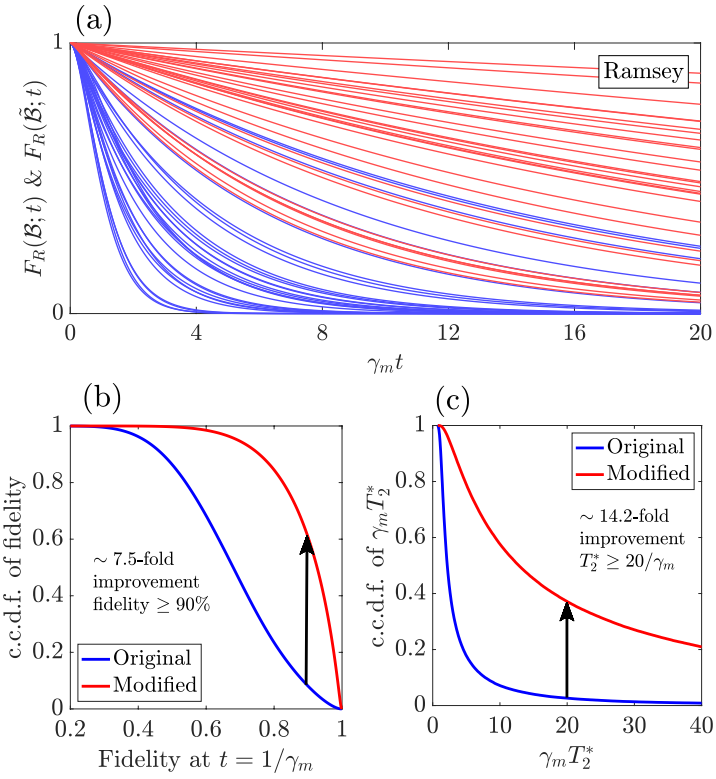

Figure 4.8: Improvement of Ramsey decay by removal of exceptional defects for a normal distribution of coupling strengths. (a) Ramsey decay over 30 bath samples (blue curves) with $\gamma_M/\gamma_m = 10^5$ and $n = 12$, giving $d \approx 1.04$. The coupling strengths are normally distributed with mean $\bar{v} = \gamma_m$ and deviation $\sigma_V = \gamma_m/10$. Each bath sample is modified by removing two TLFs with the smallest rates. Ramsey decay over modified baths is shown in red curves. (b) C.c.d.f.'s of fidelity at time $t = 1/\gamma_m$ for the original and modified baths. The fraction of qubits with fidelity above 90% has approximately a 7.5-fold improvement. (c) C.c.d.f.'s of T_2^* for original and modified baths. The fraction of qubits with coherence times $T_2^* \geq 20/\gamma_m$ improves approximately by a factor of 14.2.

the noise if it is a Gaussian random process [48], and the noise produced by a sparse bath can be non-Gaussian.

Increasing the bath density d, while keeping the interval $[\gamma_m,\ \gamma_M]$ and the noise variance $n\bar{v}^2$ constant, reduces the variability of Ramsey and echo decay [see Figs. 4.1, 4.2, and 4.3]. As the bath density d approaches infinity, the variability of Ramsey and echo decay disappears, and the signals $F_{R/H}(\mathcal{B};t)$ and $F_{R/H}[S(\omega);t]$, given by Eqs. (4.25) and (4.30), merge. In this limit, the noise produced by the TLF bath becomes a Gaussian random process. We stress that it is the bath density d and not the number of TLFs n that determine the Gaussianity of the noise. We believe that the present devices with high-quality qubits are plausibly coupled to sparse baths with small bath density d. In this regime, the qubit decoherence variability is high, despite the similarity of noise spectra shown in Fig. 4.1(b).

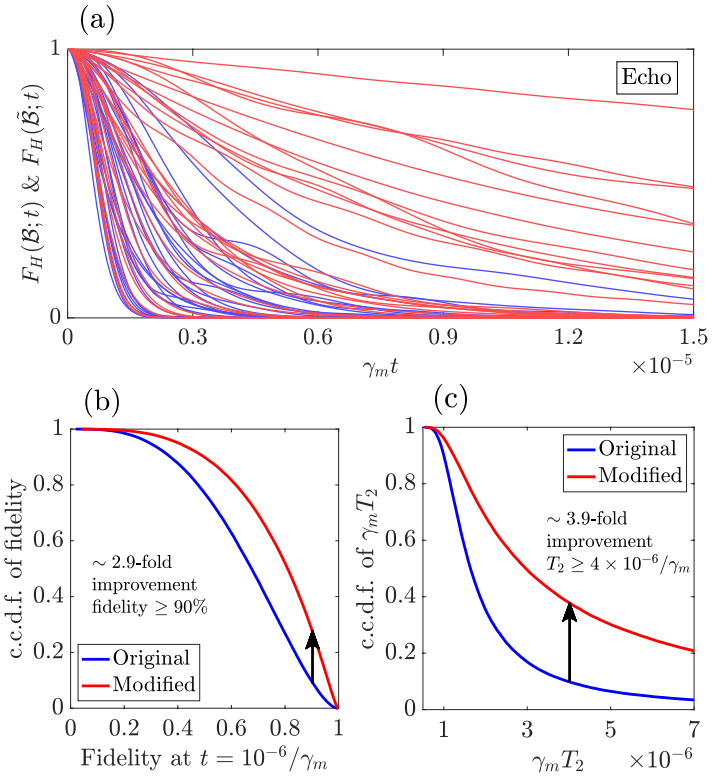

Figure 4.9: Improvement of echo decay by removal of exceptional defects for a normal distribution of coupling strengths. (a) echo decay over 30 bath samples (blue curves) with $\gamma_M/\gamma_m = 10^{12}$ and $n = 20$, giving $d \approx 0.72$. The coupling strengths are normally distributed with mean $\bar{v} = 10^6\gamma_m$ and deviation $\sigma_V = \bar{v}$. Each sample bath is modified by removing two TLFs with rates closest to $\bar{v}$. Ramsey decay over modified baths is shown in red curves. (b) C.c.d.f.'s of fidelity at time $t = 10^{-6}/\gamma_m$ for the original and modified baths. The fraction of qubits with fidelity above 90% improves approximately by a factor of 2.9. (c) C.c.d.f.'s of T_2 for original and modified baths. The fraction of qubits with coherence times $T_2 \geq 4 \times 10^{-6}/\gamma_m$ has approximately a 3.9-fold improvement.

We now analyze the significant impact of exceptional defects on coherence times, despite them being a small fraction of defects. Exceptional defects are best understood in the Ramsey decay. We consider the special case of strictly weak coupling strengths, $\forall k : \bar{v} \ll \gamma_k$, that are infinitely narrow distributed, $P_V(v) = \delta(v - \bar{v})$. The total Ramsey decay in the sample bath $\mathcal{B}$ and the decay induced by a single TLF are given by Eqs. (4.25) and (4.26), respectively. Asymptotically, the Ramsey decay induced by a single fluctuator for times $t \gg \gamma_k$ converges to

$$f_R(\gamma_k, \bar{v}; t) \approx \exp(-\frac{\bar{v}^2 t}{2\gamma_k}). \tag{4.31}$$

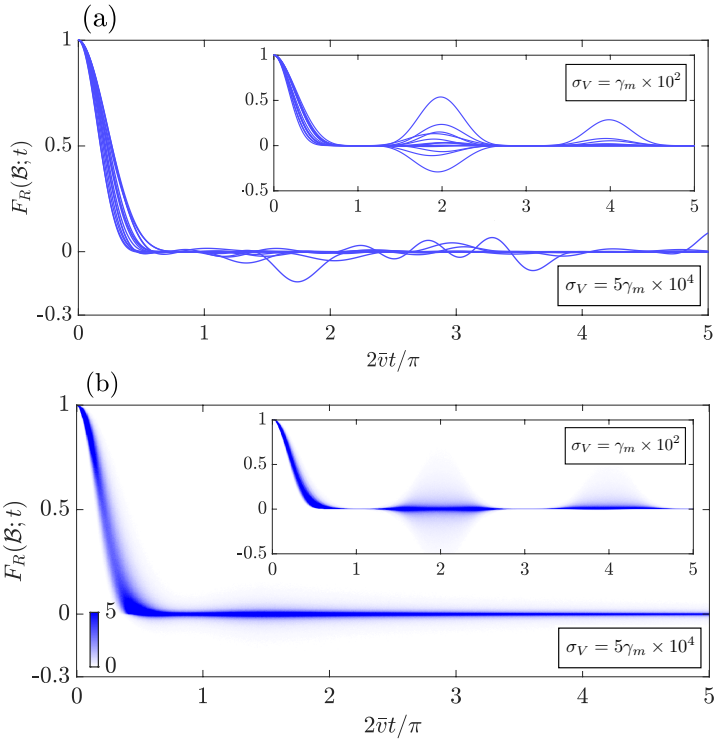

Figure 4.10: Revivals of Ramsey decay over sparse bath samples in the strong coupling regime ($\bar{v} \gg \gamma_m$), with a fixed ratio of $\gamma_M/\gamma_m = 10^{10}$, mean coupling strength of $\bar{v} = \gamma_m \times 10^5$, and $n = 16$ TLFs giving a bath density of $d \approx 0.69$. The axes of insets have the same labels as the main panels. (a) Ramsey decay over 15 sparse bath samples with a wide distribution of coupling strengths with standard deviation $\sigma_V = 5\gamma_m \times 10^5$. The inset shows the Ramsey decay in bath samples with a narrow distribution of coupling strengths with standard deviation $\sigma_V = \gamma_m \times 10^2$. (b) Histograms estimating the p.d.f.'s of the Ramsey decay with the same parameters as in (a) and its inset. In our numerical simulations, we considered the whole range of Ramsey decay $F_R(\mathcal{B};t)$, i.e., $[-1,\ 1]$, and the resolution of both the outer panel and the inset were originally 1000×1250 pixels. A vertical column of 1000 pixels at a given time t represents a histogram of 10^5 samples of $F_R(\mathcal{B};t)$. In the outer panel and its inset, the number of counts in each pixel is divided by 200 to estimate the p.d.f. values of $F_R(\mathcal{B};t)$. The estimated p.d.f. values smaller than 5 are linearly mapped to the color bar, while those greater than or equal to 5 are mapped to the darkest shade in the color bar. Here, we have cropped the plots for aesthetic reasons. The outer panel covers the range of Ramsey decay $[-0.3,\ 1]$ with a resolution of 650×1250 pixels. The inset covers the range of Ramsey decay $[-0.5,\ 1]$ and has a resolution of 750×1250 pixels.

For times $t \gg 1/\gamma_m$, the total Ramsey decay becomes

$$F_R(\mathcal{B};t) \approx \exp(-\frac{\bar{v}^2 t}{2}\zeta), \qquad \zeta = \sum_{k=1}^{n} \tau_k, \tag{4.32}$$

where $\tau_k = 1/\gamma_k$ with $k = 1, \ldots, n$. The probability density of γ_k is invariant under

this change of variable, i.e.,

$$P_T(\tau) = \frac{1}{w\tau}, \qquad \tau \in [\tau_m,\ \tau_M], \tag{4.33}$$

which is the same as $P_\Gamma(\gamma)$ given in Eq. (4.6), excluding the cutoffs $\tau_m = 1/\gamma_M$ and $\tau_M = 1/\gamma_m$. The probability density $P_Z(\zeta)$ of the sum ζ strongly affects the behavior of Ramsey decay. We sort the summands $\tau_1, \ldots, \tau_n$ by their magnitudes, with the typical ratio of subsequent summands $r \sim e^{1/d}$. When $d \ll 1$, the ratio r is large and the largest τ dominates the sum ζ. This means that the Ramsey decay in a sparse bath is dominated by the fluctuator with the smallest γ, known as the exceptional defect. Since the sum ζ is dominated by a single summand τ, it is tempting to presume its probability density resembles that of τ.

On the other hand, when $d \gg 1$, the ratio r approaches unity and neighboring summands become similar. As a result, the probability density of a group of neighboring τ's approximates a normal distribution, leading to a convolution of normal distributions for the entire sum. Therefore, a central limit theorem-like analysis is applicable in this regime.

Similar to Ramsey decay, the echo decay in sparse baths are also dominated by exceptional defects. We consider again an infinitely narrow distribution of coupling strengths. We divide the sample bath $\mathcal{B}$ into two baths of slow and fast TLFs, denoted by $\mathcal{B}_{\text{slow}}$ and $\mathcal{B}_{\text{fast}}$. The TLFs in the slow (fast) bath have rates γ smaller (larger) than the mean coupling $\bar{v}$. For times $t \gg 1/\bar{v}$, the echo decay induced by a single fast TLF is approximately $\exp(-\bar{v}^2 t/2\gamma)$, which has the same form as Eq. (4.31). The echo decay for times $t \gg 1/\bar{v}$ induced by all the fast TLFs reads

$$F_H(\mathcal{B}_{\text{fast}}; t) \approx \exp(-\frac{\bar{v}^2 t}{2}\zeta), \qquad \zeta = \sum_{k=1}^{m} \tau_k, \tag{4.34}$$

where m is the number of fast TLFs. Equation above takes the same form as Eq. (4.32). Therefore, the echo decay induced by the fast bath $\mathcal{B}_{\text{fast}}$ is dominated by the TLFs whose rates are closest to the mean coupling $\bar{v}$. On the other hand, the echo decay induced by a single slow TLF asymptotically converges to $\exp(-\gamma t)$ at times $t \gg 1/\bar{v}$. The echo decay induced by all the slow TLFs for times $t \gg 1/\bar{v}$ reads

$$F_H(\mathcal{B}_{\text{slow}}; t) \approx \exp(-\Gamma t), \qquad \Gamma = \sum_{k=1}^{l} \gamma_k, \tag{4.35}$$

where $l = n - m$. Decoherence induced by the slow bath $\mathcal{B}_{\text{slow}}$ is determined by Γ, which is a sum of log-uniformly distributed random variables γ. In sparse baths, the sum Γ is dominated by the largest γ, in the same way that ζ is dominated by the smallest γ. Therefore, the exceptional defects among the slow TLFs are also those with rates closest to $\bar{v}$.

Similar to exceptional defects, strongly coupled defects are a small fraction of defects that dominate the qubit decoherence [34, 37]. However, these defects introduce pronounced Lorentzian peaks into the noise spectral density [17]. Mathematically, these defects appear on the tail of a broad distribution, such as $P_V(v) \propto 1/v^2$ [34].

In our work, we consider a narrow distribution of coupling strengths maintaining the experimentally observed $1/f$ spectral density. Additionally, when strongly coupled defects are in resonance with the qubit, they significantly reduce the qubit's energy relaxation time T_1 through flip-flop processes [54]. The latter can be circumvented by tuning the qubit frequency away from the strongly coupled TLF. Our results on exceptional defects suggest that further improvement of coherence times is achievable even in the absence of strongly coupled defects.

Revivals of Ramsey decay, as predicted by our results, have not been previously observed in experiments. We showed that these revivals may only occur for a narrow distribution of coupling strengths, making them rare events. Additionally, confirmation bias may have prevented its detection as it is unlikely to continue recording the Ramsey signal once it decays to zero. To analyze this effect, we consider an infinitely narrow distribution of coupling strengths and divide the sample bath $\mathcal{B}$ into slow and fast baths, $\mathcal{B}_{\text{slow}}$ and $\mathcal{B}_{\text{fast}}$. Revivals are induced by the slow bath $\mathcal{B}_{\text{slow}}$, where each slow TLF causes an underdamped decay of approximately $\exp(-\gamma_k t)\cos(\bar{v}t)$. The Ramsey decay induced by all the slow TLFs reads

$$F_R(\mathcal{B}_{\text{slow}};t) \approx \exp(-\Gamma t)\cos^l(\bar{v}t), \qquad \Gamma = \sum_{k=1}^{l}\gamma_k, \tag{4.36}$$

where l is the number of slow TLFs. Revivals occur when the oscillations have similar frequencies due to a narrow distribution of coupling strengths, whereas a broad distribution or a large number of defects leads to the disappearance of revivals. This effect is similar to constructive and destructive interference.

4.5. Concluding remarks

We studied qubit decoherence by $1/f$ noise of a sparse bath of TLFs as measured in the Ramsey and Hahn echo experiments. We showed that decreasing the density of defects d leads to increased variability of coherence times among qubits. We also found that in sparse baths, the coherence times are dominated by a few exceptional defects characterized by their rates. Removing these exceptional defects can significantly improve coherence times. Additionally, we observed that for a narrow distribution of coupling strengths v, the Ramsey decay may exhibit revivals. Our findings provide new insights into the decoherence of high-quality qubits induced by $1/f$ noise and offer potential strategies for improving coherence times in many-qubit processors.

This study can be pursued in different directions. For example, our model can be extended to include qubit decoherence under dynamical decoupling pulse sequences (see App. 4.A). Our preliminary numerical simulations show that even in a dense bath, where the Ramsey decay vary slightly, the application of (perfect) refocusing pulses increases the variability of qubit decoherence (see Ch. 6). These results will be presented in a separate manuscript. Additionally, it would be useful to compare the variability of qubit decoherence in sparse baths for different dynamical decoupling protocols and investigate whether the qubit decoherence under dynamical decoupling pulse sequences is also dominated by exceptional defects.

4.A. Decoherence of a qubit subject to Carr-Purcell pulse sequence

The Ramsey and echo decay of a qubit in sparse TLF baths with $1/f$ spectral density were investigated in the main text. An important next step is to study dephasing of a qubit subject to dynamical decoupling pulse sequences. Here, we present preliminary simulation results for the Carr-Purcell sequence.

We use the same model described in Sec. 4.2 of the main text. The formulas for the Ramsey and echo decay are given in Sec. 4.2. The formula for the Carr-Purcell decay is given by [37]

$$F_{\mathrm{CP}}(\mathcal{B};\ t) = \prod_{k}^{n} f_{\mathrm{CP}}^{(k)}(t), \tag{4.37}$$

where

$$f_{\mathrm{CP}}^{(k)}(t) = \frac{e^{-\gamma_k t}}{2}\left[\frac{\gamma_k^2\cosh(\alpha_k t/m) - v_k^2}{\alpha_k\sqrt{\gamma_k^2\cosh^2(\alpha_k t/m) - v_k^2}}(\mu_{k,+}^m - \mu_{k,-}^m) + \mu_{k,+}^m + \mu_{k,-}^m\right], \tag{4.38}$$

with $\alpha_k = \sqrt{\gamma_k^2 - v_k^2}$ and

$$\mu_{k,\pm} = \frac{\gamma_k}{\alpha_k}\left[\sinh(\alpha_k t/m) \pm \sqrt{\cosh^2(\alpha_k t/m) - v_k^2/\gamma_k^2}\right]. \tag{4.39}$$

Here, m denotes the number of echo pulses, γ_k is the TLF switching rate, and v_k denotes the qubit-TLF coupling strength.

We first consider the strong coupling regime ($\gamma_m \ll \bar{v}$), where echo pulses enhance the dephasing times significantly. Figure 4.11 compares qubit dephasing as measured in the Ramsey, Hahn echo, and Carr-Purcell experiments. In Fig. 4.11, each bath sample consists of 10 TLFs and the switching rates of TLFs are log-uniformly distributed between γ_m and $\gamma_M = 10^5\gamma_m$. The coupling strengths v_k are normally distributed with mean $\bar{v} = 5\times10^4\gamma_m$ and standard deviation $\sigma_V = 10^3\gamma_m$. With this choice of parameters we are in the strong coupling regime ($\gamma_m \ll \bar{v}$). The simulations results presented in Fig. 4.11 demonstrate that while the Ramsey decay remains relatively constant across sparse bath samples, applying echo pulses leads to increased variations in qubit decoherence.

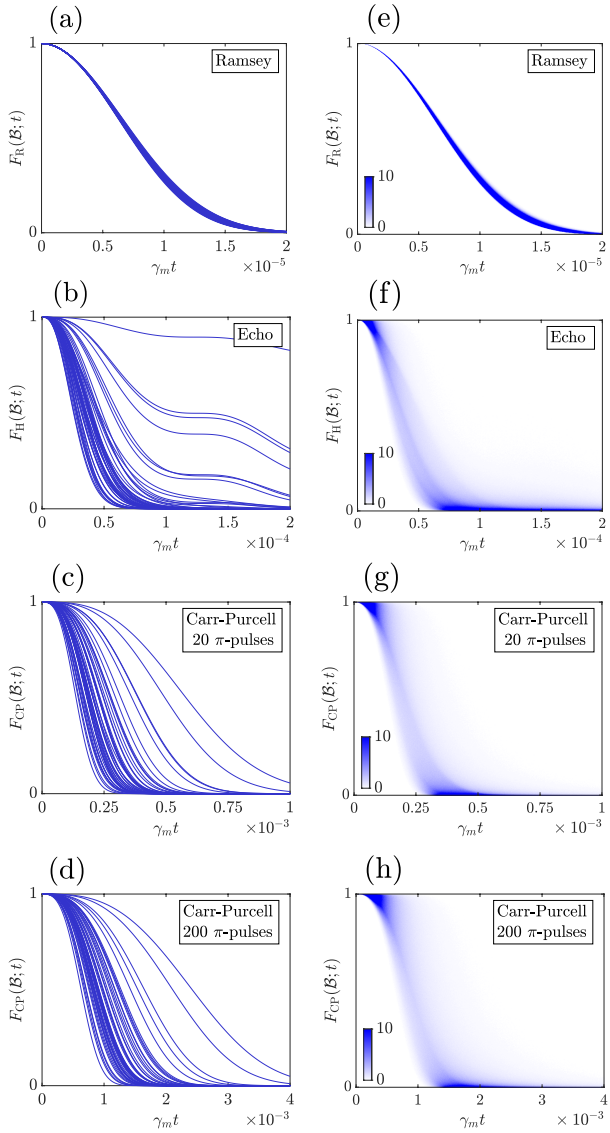

Figure 4.11: Comparison of qubit dephasing as measured in the Ramsey, Hahn echo, and Carr-Purcell experiment. (a)-(d) Each panel shows qubit decoherence in 50 bath samples with $n = 10$, $\gamma_M = 10^5\gamma_m$. The coupling strengths of TLFs are normally distributed with mean $\bar{v} = 5 \times 10^4\gamma_m$ and deviation $\sigma_V = 10^3\gamma_m$. (e)-(h) Histograms estimating p.d.f.'s of qubit decoherence. Each panel has a resolution of $10^3 \times 10^3$ pixels, and a vertical column of 10^3 pixels at a given time t represents a histogram of 10^5 samples of $F_{\mathrm{R/H/CP}}(\mathcal{B};t)$. The number of counts in each pixel is divided by 100 to estimate the probability density of $F_{\mathrm{R/H/CP}}(\mathcal{B};t)$. The estimated p.d.f. values smaller than 10 are linearly mapped to the color bar, while those greater than or equal to 10 are mapped to the darkest shade in the color bar.

Comparing the simulation results of Ramsey and echo decay [Figs. 4.11(a), (b), (e) and (f)] offers insight into the increased variability in qubit decoherence resulting from the application of echo pulses. In the Ramsey decay [see Figs. 4.11(a) and (e)], qubit decoherence is dominated by slow TLFs, with switching rates $\gamma_k < v_k$. In a given bath sample, the contribution of each slow TLF to qubit decoherence is an underdamped decay of approximately $\approx \exp(-\gamma_k t)\cos(v_k t)$ [55]. Due to narrow distribution of coupling strengths, the underdamped decays induced by slow TLFs exhibit oscillations with frequencies close to $\bar{v}$, leading to negligible variations of qubit decoherence among different bath samples. The echo decay induced by a slow TLF is approximately $\approx \exp(-\gamma_k t)$ [55]. The overall contribution of all slow TLFs to the echo decay is then approximately $\approx \exp(-\sum_k^l \gamma_k t)$, where l denotes the number of slow TLFs. The qubit decoherence is therefore influenced by a sum of log-uniformly distributed random variables $\sum_k^l \gamma_k$, resulting in significant variations across sparse bath samples [see Figs. 4.11(b) and (f)].

The effectiveness of echo pulses in mitigating qubit dephasing induced by $1/f$ noise depends on the value of mean coupling strength $\bar{v}$ relative to minimum switching rate γ_m. As discussed in the main text, for a narrow distribution of coupling strengths, the noise spectral density across different bath samples maintains its $1/f$ scaling with frequency. In our noise model, varying the mean coupling strength $\bar{v}$ does not affect the $1/f$ scaling of the spectral density with frequency. In Fig. 4.11, we considered the strong coupling regime ($\bar{v} \gg \gamma_m$), where the echo pulses significantly increase the dephasing times. In this regime, the Ramsey decay varies negligibly across bath samples, and applying a single echo pulse results in large variations of coherence times. In contrast, in the weak coupling regime ($\bar{v} \lesssim \gamma_m$), the echo pulses are less effective in enhancing the dephasing times. In the latter case, the Ramsey decay is already subject to large variations across bath samples. The contrast in variability of Ramsey decay in the weak and strong coupling regimes, and effectiveness of a single echo pulse in increasing the coherence times, is illustrated in Fig. 4.12.

Simulations of qubit decoherence in the weak coupling regime ($\bar{v} < \gamma_m$) and for the Carr-Purcell sequence are presented in Figs. 4.13(c)-(d). Figures 4.13(a)-(b) show the Ramsey and echo decay and have been repeatedly presented before. Here, we include them for understanding the performance of the Carr-Purcell sequence in the weak coupling regime. In Figs. 4.13(a)-(d), each curve represents the qubit decoherence in a specific bath sample. Each bath sample consists of 10 TLFs with switching rates γ log-uniformly distributed between the minimum rate γ_m and the maximum rate $\gamma_M = 10^5\gamma_m$. The coupling strengths v are normally distributed with the mean value $\bar{v} = 0.5 \times \gamma_m$ and standard deviation $\sigma_V = 0.01 \times \gamma_m$.

As previously mentioned, the effectiveness of echo pulses in mitigating the qubit decoherence depends on the value of the mean coupling strength $\bar{v}$ compared to the range of TLF rates $[\gamma_m,\ \gamma_M]$ [35, 56]. As shown in Figs. 4.13(a)-(c), in the weak coupling where $\bar{v} < \gamma_m$, the Ramsey and echo decays exhibit similar coherence times on average, and the Carr-Purcell sequence with 20 π-pulses does not lead to significant improvements of coherence times. Since $\bar{v}$ is smaller than γ_m, the coherence fidelities, $F_{\mathrm{R}}(\mathcal{B};\ t)$, start to decay exponentially at very short times.

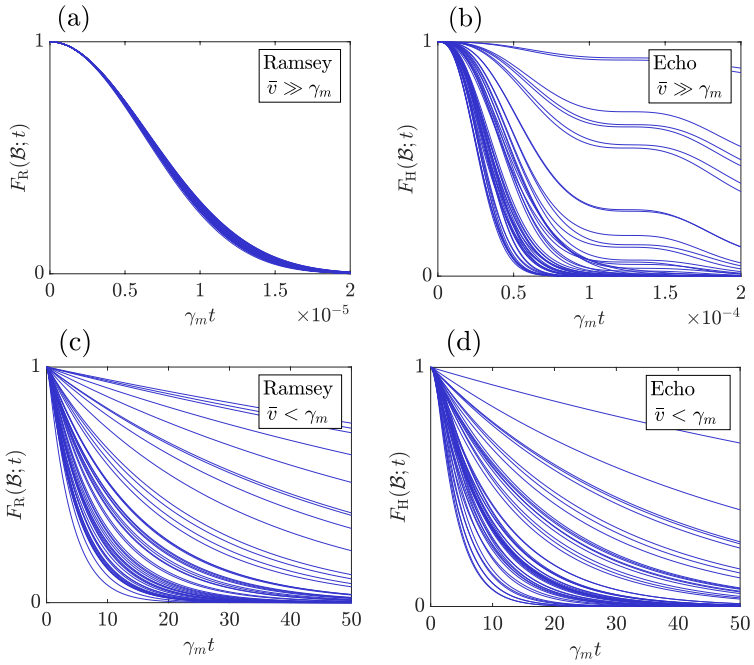

Figure 4.12: Comparison of Ramsey and echo decay in the strong ($\bar{v} \gg \gamma_m$) versus weak ($\bar{v} < \gamma_m$) coupling regimes. Each curve represents the Ramsey/echo decay in a sample bath consisting of 10 TLFs. The TLF rates in (a)-(d) are log-uniformly distributed between γ_m and $\gamma_M = 10^5\gamma_m$. (a)-(b) Ramsey and echo decay in the strong coupling regime. The coupling strengths v are normally distributed with mean $5 \times 10^4\gamma_m$ and deviation $10^3\gamma_m$. The Ramsey decays in (a) show minimal variations across bath samples, while the echo decays in (b) exhibit large variations. (c)-(d) Ramsey and echo decay in the weak coupling regime. The coupling strengths v are normally distributed with mean $0.5 \times \gamma_m$ and deviation $0.01 \times \gamma_m$. The Ramsey decays in (c) are already subject to large variations across bath samples, and applying an echo pulse in (d) does not result in a notable improvement in coherence times.

This can be likened to motional narrowing effect. Roughly speaking, in the weak coupling regime, an echo pulse can mitigate the qubit decoherence if applied at the time interval prior to exponential decay, where the curvature of coherence fidelity $F_{\mathrm{R}}(\mathcal{B};\ t)$ is still negative. Since this time interval in the weak coupling regime is small, more and more echo pulses are needed to mitigate the qubit decoherence. This effect is illustrated in Fig. 4.12(d), where the Carr-Purcell sequence with 200 π-pulses eventually leads to noticeable increase in the coherence times.

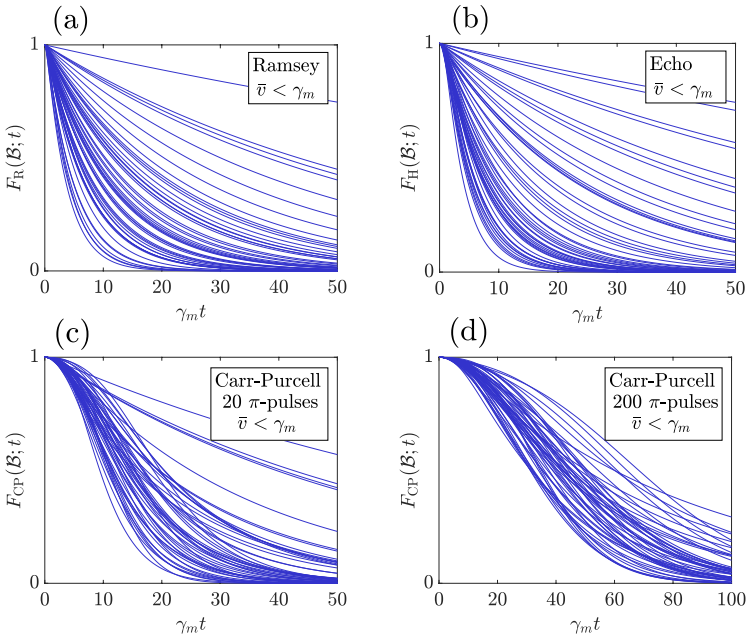

Figure 4.13: Qubit decoherence in the weak coupling regime for the Ramsey, echo, and Carr-Purcell sequence. (a)-(d) Each curve represents the qubit decoherence in a specific bath sample consisting of 10 TLFs with rates γ log-uniformly distributed between γ_m and $\gamma_M = 10^5\gamma_m$. The coupling strengths are normally distributed with mean $\bar{v} = 0.5 \times \gamma_m$ and standard deviation $\sigma_V = 0.01 \times \gamma_m$. (a)-(b) The coherence times in the Ramsey (a) and echo (b) decay appear to be similar. (c) The Carr-Purcell sequence with 20 π-pulses does not lead to significant improvements of coherence times. (d) The Carr-Purcell sequence with 200 π-pulses leads to noticeable improvement of coherence times.

REFERENCES

[1] M. Mehmandoost and V. V. Dobrovitski, *Decoherence induced by a sparse bath of two-level fluctuators: Peculiar features of $1/f$ noise in high-quality qubits,* Phys. Rev. Res. **6**, 033175 (2024).

[2] D. P. DiVincenzo, *The physical implementation of quantum computation,* Fortschritte der Physik **48**, 771 (2000).

[3] B. M. Terhal, *Quantum error correction for quantum memories,* Rev. Mod. Phys. **87**, 307 (2015).

[4] E. Paladino, Y. M. Galperin, G. Falci, and B. L. Altshuler, *$1/f$ noise: Implications for solid-state quantum information,* Rev. Mod. Phys. **86**, 361 (2014).

[5] E. Kawakami, T. Jullien, P. Scarlino, D. R. Ward, D. E. Savage, M. G. Lagally, V. V. Dobrovitski, M. Friesen, S. N. Coppersmith, M. A. Eriksson, and L. M. K. Vandersypen, *Gate fidelity and coherence of an electron spin in an*

si/sige quantum dot with micromagnet, Proceedings of the National Academy of Sciences **113**, 11738 (2016).

[6] L. M. K. Vandersypen, H. Bluhm, J. S. Clarke, A. S. Dzurak, R. Ishihara, A. Morello, D. J. Reilly, L. R. Schreiber, and M. Veldhorst, *Interfacing spin qubits in quantum dots and donnors–hot, dense, and coherent,* npj Quantum Inf. **3**, 34 (2017).

[7] J. Yoneda, K. Takeda, T. Otsuka, T. Nakajima, M. R. Delbecq, G. Allison, T. Honda, T. Kodera, S. Oda, Y. Hoshi, N. Usami, K. M. Itoh, and S. Tarucha, *A quantum-dot spin qubit with coherence limited by charge noise and fidelity higher than 99.9%,* Nature Nanotech. **13**, 102 (2018).

[8] E. J. Connors, JJ Nelson, H. Qiao, L. F. Edge, and J. M. Nichol, *Low-frequency charge noise in Si/SiGe quantum dots,* Phys. Rev. B **100**, 165305 (2019).

[9] L. Petit, H. G. J. Eenink, M. Russ, W. I. L. Lawrie, N. W. Hendrickx, S. G. J. Philips, J. S. Clarke, L. M. K. Vandersypen, and M. Veldhorst, *Universal quantum logic in hot silicon qubits,* Nature **580**, 355 (2020).

[10] T. Struck, A. Hollmann, F. Schauer, O. Fedorets, A. Schmidbauer, K. Sawano, H. Riemann, N. V. Abrosimov, Ł. Cywiński, D. Bougeard, and L. R. Schreiber, *Low-frequency spin qubit energy splitting noise in highly purified* ^{28}*Si/SiGe,* npj Quantum Inf. **6**, 40 (2020).

[11] E. J. Connors, J. Nelson, and J. M. Nichol, *Charge-noise spectroscopy of Si/SiGe quantum dots via dynamically-decoupled exchange oscillations,* Nat. Commun. **13**, 940 (2022).

[12] G. Ithier, E. Collin, P. Joyez, P. J. Meeson, D. Vion, D. Esteve, F. Chiarello, A. Shnirman, Y. Makhlin, J. Schriefl, and G. Schön, *Decoherence in a superconducting quantum bit circuit,* Phys. Rev. B **72**, 134519 (2005).

[13] F. Yoshihara, K. Harrabi, A. O. Niskanen, Y. Nakamura, and J. S. Tsai, *Decoherence of flux qubits due to* $1/f$ *flux noise,* Phys. Rev. Lett. **97**, 167001 (2006).

[14] R. C. Bialczak, R. McDermott, M. Ansmann, M. Hofheinz, N. Katz, E. Lucero, M. Neeley, A. D. O'Connell, H. Wang, A. N. Cleland, and J. M. Martinis, $1/f$ *flux noise in Josephson phase qubits,* Phys. Rev. Lett. **99**, 187006 (2007).

[15] K. Kakuyanagi, T. Meno, S. Saito, H. Nakano, K. Semba, H. Takayanagi, F. Deppe, and A. Shnirman, *Dephasing of a superconducting flux qubit,* Phys. Rev. Lett. **98**, 047004 (2007).

[16] F. Luthi, T. Stavenga, O. W. Enzing, A. Bruno, C. Dickel, N. K. Langford, M. A. Rol, T. S. Jespersen, J. Nygård, P. Krogstrup, and L. DiCarlo, *Evolution of nanowire transmon qubits and their coherence in a magnetic field,* Phys. Rev. Lett. **120**, 100502 (2018).

[17] S. Schlör, J. Lisenfeld, C. Müller, A. Bilmes, A. Schneider, D. P. Pappas, A. V. Ustinov, and M. Weides, *Correlating decoherence in transmon qubits: Low frequency noise by single fluctuators,* Phys. Rev. Lett. **123**, 190502 (2019).

[18] S. Kogan, *Electronic Noise and Fluctuations in Solids* (Cambridge University Press, Cambridge, England, 1996).

[19] P. Dutta and P. M. Horn, *Low-frequency fluctuations in solids: $\frac{1}{f}$ noise,* Rev. Mod. Phys. **53**, 497 (1981).

[20] M. B. Weissman, $\frac{1}{f}$ *noise and other slow, nonexponential kinetics in condensed matter,* Rev. Mod. Phys. **60**, 537 (1988).

[21] U. Weiss, *Quantum Dissipative Systems*, 4th ed. (WORLD SCIENTIFIC, 2012).

[22] P. W. Anderson, B. I. Halperin, and C. M. Varma, *Anomalous low-temperature thermal properties of glasses and spin-glasses,* Philos. Mag. **25**, 1 (1972).

[23] W. A. Phillips, *Tunneling states in amorphous solids,* J. Low Temp. Phys. **7**, 351 (1972).

[24] J. Lisenfeld, A. Bilmes, A. Megrant, R. Barends, J. Kelly, P. Klimov, G. Weiss, J. M. Martinis, and A. V. Ustinov, *Electric field spectroscopy of material defects in transmon qubits,* npj Quantum Information **5**, 105 (2019).

[25] M. Meyer, C. Déprez, T. R. van Abswoude, I. N. Meijer, D. Liu, C.-A. Wang, S. Karwal, S. Oosterhout, F. Borsoi, A. Sammak, N. W. Hendrickx, G. Scappucci, and M. Veldhorst, *Electrical control of uniformity in quantum dot devices,* Nano Letters **23**, 2522 (2023).

[26] J. Atalaya, J. Clarke, G. Schön, and A. Shnirman, *Flux $1/f^{\alpha}$ noise in two-dimensional heisenberg spin glasses: Effects of weak anisotropic interactions,* Phys. Rev. B **90**, 014206 (2014).

[27] D. A. Rower, L. Ateshian, L. H. Li, M. Hays, D. Bluvstein, L. Ding, B. Kannan, A. Almanakly, J. Braumüller, D. K. Kim, A. Melville, B. M. Niedzielski, M. E. Schwartz, J. L. Yoder, T. P. Orlando, J. I.-J. Wang, S. Gustavsson, J. A. Grover, K. Serniak, R. Comin, and W. D. Oliver, *Evolution of $1/f$ flux noise in superconducting qubits with weak magnetic fields,* (2023), arXiv:2301.07804 [cond-mat.mes-hall] .

[28] B. Paquelet Wuetz, D. Degli Esposti, A.-M. J. Zwerver, S. V. Amitonov, M. Botifoll, J. Arbiol, A. Sammak, L. M. K. Vandersypen, M. Russ, and G. Scappucci, *Reducing charge noise in quantum dots by using thin silicon quantum wells,* Nat. Commun. **14**, 1385 (2023).

[29] A. Elsayed, M. Shehata, C. Godfrin, S. Kubicek, S. Massar, Y. Canvel, J. Jussot, G. Simion, M. Mongillo, D. Wan, B. Govoreanu, I. P. Radu, R. Li, P. V. Dorpe, and K. D. Greve, *Low charge noise quantum dots with industrial CMOS manufacturing,* (2022), arXiv:2212.06464 [cond-mat.mes-hall] .

[30] J. M. Martinis, K. B. Cooper, R. McDermott, M. Steffen, M. Ansmann, K. D. Osborn, K. Cicak, S. Oh, D. P. Pappas, R. W. Simmonds, and C. C. Yu, *Decoherence in Josephson qubits from dielectric loss,* Phys. Rev. Lett. **95**, 210503 (2005).

[31] P. Kumar, S. Sendelbach, M. A. Beck, J. W. Freeland, Z. Wang, H. Wang, C. C. Yu, R. Q. Wu, D. P. Pappas, and R. McDermott, *Origin and reduction of* $1/f$ *magnetic flux noise in superconducting devices,* Phys. Rev. Applied **6**, 041001 (2016).

[32] S. E. de Graaf, A. A. Adamyan, T. Lindström, D. Erts, S. E. Kubatkin, A. Y. Tzalenchuk, and A. V. Danilov, *Direct identification of dilute surface spins on* al_2o_3*: Origin of flux noise in quantum circuits,* Phys. Rev. Lett. **118**, 057703 (2017).

[33] J. Lisenfeld, A. Bilmes, and A. V. Ustinov, *Enhancing the coherence of superconducting quantum bits with electric fields,* npj Quantum Inf. **9**, 8 (2023).

[34] J. Schriefl, Y. Makhlin, A. Shnirman, and G. Schön, *Decoherence from ensembles of two-level fluctuators,* New Journal of Physics **8**, 1 (2006).

[35] L. Cywiński, R. M. Lutchyn, C. P. Nave, and S. Das Sarma, Phys. Rev. B **77**, 174509 (2008).

[36] J. Bergli, Y. M. Galperin, and B. L. Altshuler, *Decoherence in qubits due to low-frequency noise,* New Journal of Physics **11**, 025002 (2009).

[37] P. Szańkowski, G. Ramon, J. Krzywda, D. Kwiatkowski, and Ł. Cywiński, *Environmental noise spectroscopy with qubits subjected to dynamical decoupling,* Journal of Physics: Condensed Matter **29**, 333001 (2017).

[38] H. J. Wold, H. Brox, Y. M. Galperin, and J. Bergli, *Decoherence of a qubit due to either a quantum fluctuator, or classical telegraph noise,* Phys. Rev. B **86**, 205404 (2012).

[39] F. K. Du Pré, *A suggestion regarding the spectral density of flicker noise,* Phys. Rev. **78**, 615 (1950).

[40] A. Van Der Ziel, *On the noise spectra of semi-conductor noise and of flicker effect,* Physica **16**, 359 (1950).

[41] A. L. McWhorter, *Semiconductor surface physics,* (University of Pennsylvania Press, Philadelphia, 1957) Chap. $1/f$ noise and germanium surface properties, pp. 207–228.

[42] Y. M. Galperin, B. L. Altshuler, J. Bergli, and D. V. Shantsev, *Non-Gaussian low-frequency noise as a source of qubit decoherence,* Phys. Rev. Lett. **96**, 097009 (2006).

[43] M. B. Weissman, *What is a spin glass? a glimpse via mesoscopic noise,* Rev. Mod. Phys. **65**, 829 (1993).

[44] E. Paladino, L. Faoro, G. Falci, and R. Fazio, *Decoherence and $1/f$ noise in Josephson qubits,* Phys. Rev. Lett. **88**, 228304 (2002).

[45] M. Pioro-Ladrière, J. H. Davies, A. R. Long, A. S. Sachrajda, L. Gaudreau, P. Zawadzki, J. Lapointe, J. Gupta, Z. Wasilewski, and S. Studenikin, *Origin of switching noise in* $GaAs/Al_xGa_{1-x}As$ *lateral gated devices,* Phys. Rev. B **72**, 115331 (2005).

[46] C. Müller, J. H. Cole, and J. Lisenfeld, *Towards understanding two-level-systems in amorphous solids: insights from quantum circuits,* Rep. Prog. Phys. **82**, 124510 (2019).

[47] N. G. van Kampen, *Stochastic Processes in Physics and Chemistery*, 3rd ed. (Elsevier, Amsterdam, 2007).

[48] R. Kubo, M. Toda, and N. Hashitsume, *Statistical Physics II: Nonequilibrium Statistical Mechanics* (Springer, Heidelberg, Germany, 1991).

[49] W. Feller, *An Introduction to Probability Theory and Its Applications*, 2nd ed., Vol. II (John Wiley & Sons, New York, 1991).

[50] L. Viola and S. Lloyd, *Dynamical suppression of decoherence in two-state quantum systems,* Phys. Rev. A **58**, 2733 (1998).

[51] C. Slichter, *Principles of Magnetic Resonance*, Springer Series in Solid-State Sciences (Springer Berlin Heidelberg, 1996).

[52] G. Zhidomirov and K. M. Salikhov, *Contribution to the theory of spectral diffusion in magnetically diluted solids,* Sov. Phys. JETP **29**, 1037 (1969).

[53] R. de Sousa and S. Das Sarma, *Theory of nuclear-induced spectral diffusion: Spin decoherence of phosphorus donors in Si and GaAs quantum dots,* Phys. Rev. B **68**, 115322 (2003).

[54] P. V. Klimov, J. Kelly, Z. Chen, M. Neeley, A. Megrant, B. Burkett, R. Barends, K. Arya, B. Chiaro, Y. Chen, A. Dunsworth, A. Fowler, B. Foxen, C. Gidney, M. Giustina, R. Graff, T. Huang, E. Jeffrey, E. Lucero, J. Y. Mutus, O. Naaman, C. Neill, C. Quintana, P. Roushan, D. Sank, A. Vainsencher, J. Wenner, T. C. White, S. Boixo, R. Babbush, V. N. Smelyanskiy, H. Neven, and J. M. Martinis, *Fluctuations of energy-relaxation times in superconducting qubits,* Phys. Rev. Lett. **121**, 090502 (2018).

[55] S. Matityahu, A. Shnirman, G. Schön, and M. Schechter, *Decoherence of a quantum two-level system by spectral diffusion,* Phys. Rev. B **93**, 134208 (2016).

[56] G. Ramon, *Non-Gaussian signatures and collective effects in charge noise affecting a dynamically decoupled qubit,* Phys. Rev. B **92**, 155422 (2015).

5

Dephasing times and frequency shifts of heated spin qubits

Semiconductor spin qubits offer the potential for scalable quantum computing by integrating classical electronics on the same chip as the qubits. To achieve this, operating spin qubits at temperatures above 1 K is necessary, yet their performance at higher temperatures remains poorly understood due to most experiments being conducted below 100 mK. Two observed phenomena in the pursuit of operating spin qubits at higher temperatures are thermal stabilities of dephasing times and a temperature-dependent shift in qubit frequency. We investigate whether these two phenomena can be explained by a phenomenological model of charge noise originating from a bath of tunneling two-level fluctuators coupled to acoustic phonons. The theoretical model justifies the qubit frequency shift as the equilibrium state of the two-level fluctuators shifts the qubit frequency by a constant value. The model also relates the Ramsey and echo decay times to phonon bath temperature. However, our numerical simulations reveal that while each effect can be explained by adjusting the model parameters, our model does not reproduce both phenomena simultaneously. Our hope is that the present work motivates the development of experiments to refute or validate this phenomenological model.

Author contributions: Contributed to conceiving and implemented the work. Analyzed the results with inputs from L. M. K. Vandersypen, V. V. Dobrovitski, and M. Rimbach-Russ.

5.1. Introduction

Real-time communication between the classical and quantum realms is essential for fault-tolerant quantum computing, which involves detecting and correcting errors in millions of qubits using algorithms running on a classical computer [1]. However, current semiconductor spin qubits are typically operated at temperatures below 100 mK [2, 3], and room-temperature control electronics interface them to a classical computer. This creates an interconnect bottleneck in scaling spin qubits due to limitations in cooling power [4–6]. Operating spin qubits at elevated temperatures of $1-4$ K potentially allows for the integration of a first layer of classical electronics next to the qubits thus facilitating the scalability [4].

Recent efforts to raise the operating temperature of quantum dot spin qubits have yielded promising results [5–10]. However, these experiments have uncovered intriguing phenomena that require further investigation. Specifically, increasing the temperature of silicon spin qubits (from a few millikelvin to 0.6 K) has been shown to cause a shift in their Larmor frequency [11], that may be linked to pulse-induced resonance shift [12, 13]. Additionally, coherence times of the spin qubits measured in the Ramsey and Hahn echo experiments have shown little dependence on temperatures below 1 K [5, 6, 8].

In this chapter, we study the temperature dependencies of the qubit frequency as well as the Ramsey and echo decay times using a phenomenological model of charge noise. The microscopic origins of charge noise in quantum dot devices is a subject of ongoing research [13–19]. Here, we model the charge noise by a bath of Two-Level Fluctuators (TLFs) which undergo tunneling by emission and absorption of acoustic phonons. The electric dipole moments of the TLFs couple to the charge, and therefore orbital state, of the quantum dot electron via the Coulomb interaction. The artificial and/or intrinsic spin-orbit interactions convert the electric fields to magnetic fields [20]. Therefore, the electric field fluctuations caused by TLFs translate to random modulations of the qubit Larmor frequency.

Random modulations of the qubit Larmor frequency result in dephasing of the spin qubits and their mean value shifts the qubit frequency. Since the dynamics of TLFs depend on the phonon bath temperature, the random modulations of the qubit frequency is also temperature dependent [21]. The qubit frequency shift can be explained by the time-averaged states of the TLFs in thermal equilibrium with the phonon bath. The coherence times of spin qubits are relatively insensitive to temperature in various material stacks used for fabricating quantum dot devices [5, 6, 8]. However, the qubit frequency shift is unique to each device heterostructure and can be positive, negative, or non-monotonic depending on the device heterostructure [11, 12, 22]. In this work, we aim to replicate the positive non-monotonic frequency shift reported in Ref. [11], where the qubit frequency increases with temperature, reaching a maximum at approximately 200 mK before declining at higher temperatures.

The rest of this chapter is organized as follows. In Sec. 5.2, we introduce the phenomenological model of the low-frequency charge noise produced by a bath of TLFs, and present the formulas for the qubit Ramsey and echo decay and the qubit frequency shift. Section 5.3 presents the numerical simulations of the model. We

analyze and discuss the simulation results in Sec. 5.4. We conclude the chapter in Sec. 5.5 by pointing at the implications of our results and suggesting future research directions.

5.2. Model description

We consider a qubit coupled to a bath of TLFs. The density matrix of the qubit can be expressed as

$$\hat{\rho} = \frac{1}{2}(\mathbf{1} + m_x\hat{\sigma}_x + m_y\hat{\sigma}_y + m_z\hat{\sigma}_z), \tag{5.1}$$

where $\hat{\sigma}_x$, $\hat{\sigma}_y$, and $\hat{\sigma}_z$ are the Pauli matrices, $\mathbf{1}$ is the identity matrix, and m_α with $\alpha \in \{x, y, z\}$ are the components of the qubit's Bloch vector. The qubit is defined using the basis states $|0\rangle$ and $|1\rangle$, which are the eigenstates of the Pauli matrix $\hat{\sigma}_z$ with eigenvalues $+1$ and -1, respectively.

The Hamiltonian of the whole system can be written as

$$\hat{H} = \hat{H}_\mathrm{Q} + \hat{H}_\mathrm{B} + \hat{H}_\mathrm{I}, \tag{5.2}$$

where $\hat{H}_\mathrm{Q}$ represents the qubit Hamiltonian, $\hat{H}_\mathrm{B}$ is the Hamiltonian of the TLF bath coupled to acoustic phonons, and $\hat{H}_\mathrm{I}$ describes the interaction between the qubit and the TLF bath. For simplicity, we set $\hbar = 1$. The qubit states $|0\rangle$ and $|1\rangle$ are encoded in the eigenstates of a single electron spin, parallel and anti-parallel to an external magnetic field $B_z\hat{\mathbf{e}}_z$. The qubit Hamiltonian can be expressed as

$$\hat{H}_\mathrm{Q} = -\frac{\omega_0}{2}\hat{\sigma}_z + \frac{\Omega(t)}{2}\cos[\omega_0 t + \phi(t)]\hat{\sigma}_x, \tag{5.3}$$

where the first term represents the spin precession with Larmor frequency ω_0 around the quantization axis $\hat{\mathbf{e}}_z$. The second term describes the control pulse sequence in Ramsey and Hahn echo experiments, where $\Omega(t)$ denotes the envelope and $\phi(t)$ specifies the phase of the control pulses. These pulses are resonant with the qubit's Larmor frequency ω_0, inducing single-qubit rotations, with the rotation angle and axis determined by $\Omega(t)$ and $\phi(t)$ [23]. The Larmor frequency $\omega_0 = g\mu_\mathrm{B}B_z$ includes the Bohr magneton μ_B, the electron Landé g-factor, and the strength of the external magnetic field B_z.

The qubit bath is described using the standard TLF model, which was initially developed to explain anomalies observed in glasses at low temperatures [24–33]. In this model, a TLF refers to a charged particle that can tunnel between two localized states due to interactions with acoustic phonons. The Hamiltonian that describes the TLF bath can be expressed as the sum of three terms:

$$\hat{H}_\mathrm{B} = \hat{H}_\mathrm{TLF} + \hat{H}_\mathrm{ph} + \hat{H}_\mathrm{int}. \tag{5.4}$$

The first term, represents the bare Hamiltonian of the TLF ensemble in the localized basis and is given by

$$\hat{H}_\mathrm{TLF} = \frac{1}{2}\sum_k^n(\epsilon_k\hat{\tau}_k^z + \Delta_k\hat{\tau}_k^x), \tag{5.5}$$

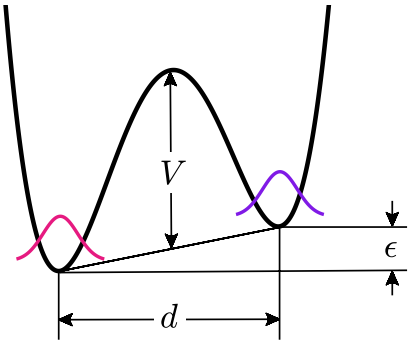

Figure 5.1: The double-well potential of a tunneling TLF. The localized states of the TLF with detuning energy ϵ and distance d are depicted by the blue and red curves. The average energy of the localized states is considered to be zero. The barrier height from the zero of energy is indicated by V. The tunneling amplitude $\Delta = \Delta_0 \exp(-\Lambda)$, where $\Lambda \approx (2m_* V)^{1/2} d/2$ and Δ_0 depend on the specific details of the double-well potential [24]. Here, m_* represents the mass of the tunneling entity.

where k labels the TLFs and $\hat{\tau}_k^\alpha$ with $\alpha \in \{x, y, z\}$ are the Pauli matrices acting in the subspace of the k-th TLF. The parameters ϵ_k and Δ_k are the detuning energy and tunneling amplitude, respectively. They depend on details of the TLF potential shown in Fig. 5.1. The second term, given by

$$\hat{H}_{\text{ph}} = \sum_\lambda \omega_\lambda \hat{a}_\lambda^\dagger \hat{a}_\lambda, \tag{5.6}$$

describes the phonon bath, which is a collection of harmonic oscillators with angular frequencies ω_λ. Here, $\hat{a}_\lambda$ and $\hat{a}_\lambda^\dagger$ are bosonic annihilation and creation operators. The third term given by

$$\hat{H}_{\text{int}} = \sum_k^n \hat{\tau}_k^z \sum_\lambda g_\lambda (\hat{a}_\lambda + \hat{a}_\lambda^\dagger), \tag{5.7}$$

represents the interaction between the TLFs and the phonon bath. We assume for simplicity that all TLFs have the same coupling strength to the phonon mode λ, denoted as g_λ. In reality, the strain fields perturb both the detuning energy ϵ_k and tunneling amplitude Δ_k, but we ignore the perturbations of Δ_k since they are negligible [28].

We further assume that the decoherence and relaxation rates of each TLF is much larger than its coupling strength to the qubit. Under this condition, the dynamics of a TLF is not affected by the state of the qubit, and the TLF can be approximated as random telegraph noise (RTN) [34]. The corresponding dynamics of each TLF is the energy relaxation, which is best understood in the energy eigenbasis using the

transformation

$$\begin{aligned}\hat{\tau}_k^x &= \frac{\Delta_k}{E_k}\tilde{\tau}_k^z - \frac{\epsilon_k}{E_k}\tilde{\tau}_k^x \\ \hat{\tau}_k^z &= \frac{\epsilon_k}{E_k}\tilde{\tau}_k^z + \frac{\Delta_k}{E_k}\tilde{\tau}_k^x\end{aligned} \tag{5.8}$$

with $E_k = \sqrt{\epsilon_k^2 + \Delta_k^2}$. This allows us to rewrite the bare TLF Hamiltonian as

$$\tilde{H}_{\mathrm{TLF}} = \sum_k^n E_k \tilde{\tau}_k^z. \tag{5.9}$$

The transformed interaction Hamiltonian reads

$$\tilde{H}_{\mathrm{int}} = \sum_k^n \frac{\Delta_k}{E_k}\tilde{\tau}_k^x \sum_\lambda g_\lambda(\hat{a}_\lambda + \hat{a}_\lambda^\dagger), \tag{5.10}$$

where we have neglected the term proportional to $\tilde{\tau}_k^z$ due to vanishing coupling of the TLFs to off-resonant phonons [34, 35].

This study focuses on the TLFs present in dielectrics. At temperatures below 1 K, energy relaxation of TLFs is mainly determined by one-phonon processes [27]. By using Fermi's golden rule, we can compute the excitation and relaxation rates, also known as switching rates, of a TLF through one-phonon processes. The excitation rate is given by

$$\gamma_k^\uparrow = J(E_k)\left(\frac{\Delta_k}{E_k}\right)^2 n_{\mathrm{B}}(E_k), \tag{5.11}$$

while the relaxation rate is given by

$$\gamma_k^\downarrow = J(E_k)\left(\frac{\Delta_k}{E_k}\right)^2 [n_{\mathrm{B}}(E_k) + 1]. \tag{5.12}$$

Here, the Bose factor $n_{\mathrm{B}}(\omega) = [\exp(\beta\omega) - 1]^{-1}$, where $\beta = 1/k_{\mathrm{B}}T$ is the inverse temperature, and $J(\omega) = \sum_\lambda g_\lambda^2 \delta(\omega - \omega_\lambda)$ is the spectral function of the phonon bath. Considering the coupling of the TLFs to acoustic phonons, we assume a cubic spectral function $J(\omega) = 2J_0\ \omega^3$ [30].

The average switching rate, given by

$$\begin{aligned}\gamma_k &= \frac{\gamma_k^\downarrow + \gamma_k^\uparrow}{2} \\ &= J_0\ \Delta_k^2\ E_k \coth(\beta E_k/2),\end{aligned} \tag{5.13}$$

determines how fast the TLF undergoes tunneling between the excited and ground state. For simplicity, we set the Boltzman constant $k_{\mathrm{B}} = 1$. As shown in Fig. 5.2, for temperatures $T \ll E_k$, the average switching rate remains a small constant and the TLF almost freezes in the ground state. For temperatures $T \gg E_k$, the TLF excitation and relaxation rates become equal, and the average switching rate grows

linearly with temperature. It is worth noting that for large temperatures, higher excited states of the double-well potential become populated, and the TLF picture breaks down.

The TLFs couple to the spin qubit via the Coulomb interaction [36, 37]. More specifically, the electric dipole moments of the TLFs couple to the charge, and thus orbital states, of the quantum dot electron. The electron's orbital state, in turn, couples to the electron spin via the micromagnet's gradient field. The gradient field is needed to implement single-qubit gates in silicon via electric-dipole spin resonance as well as the frequency selectivity of qubits. This mechanism can be thought of as synthetic spin-orbit coupling [20, 38, 39]. In summary, changes in the TLF state effectively alter the magnetic field sensed by the electron spin. Charge noise in general contributes to both energy relaxation (T_1) and dephasing (T_2^* and T_2) of the spin qubits [20]. However, due to the energy mismatch between the TLFs and the qubit, it is assumed that the TLFs only contribute to qubit dephasing. Therefore, we describe the interaction between the qubit and the TLF bath using the simplified Hamiltonian

$$\hat{H}_{\mathrm{I}} = \hat{\sigma}_z \sum_k^n v_k \tilde{\tau}_k^z. \tag{5.14}$$

Here, the coupling strengths between the TLFs and the qubit are represented by the values v_k. We assume that the coupling strengths v_k are distributed independently and identically according to a normal probability density function given by

$$P_V(v) = \frac{1}{\sigma_V \sqrt{2\pi}} \exp\left[-\frac{1}{2}\left(\frac{v-\bar{V}}{\sigma_V}\right)^2\right], \tag{5.15}$$

where $\bar{V}$ and σ_V represent the mean and standard deviation of the random variable V. In a given bath, the coupling strengths v_k are samples of V.

We now simplify the system Hamiltonian by approximating the TLFs as RTN signals. In the frame rotating with Larmor frequency ω_0, and within the rotating wave approximation, the dynamics of a qubit in a bath of TLFs can be described by the Hamiltonian

$$\tilde{H}_{\mathrm{RWA}} = \frac{\omega_{\mathrm{Q}}(t)}{2}\hat{\sigma}_z + \frac{\Omega(t)}{2}[\cos\phi(t)\hat{\sigma}_x + \sin\phi(t)\hat{\sigma}_y]. \tag{5.16}$$

Here,

$$\omega_{\mathrm{Q}}(t) = \sum_k \nu_k(t), \tag{5.17}$$

describes random modulations of the qubit frequency induced by RTN signals. An RTN signal is denoted by $\nu_k(t) = v_k\xi_k(t)$, where v_k is the coupling constant and $\xi_k(t)$ is a two-state Markov process. Each two-state process randomly switches between the state $+1$ and -1, which are mappings of the excited and ground state of a TLF. The two-state process switches between these states with excitation and relaxation rates, $\gamma_k^{\uparrow}$ and $\gamma_k^{\downarrow}$, as given in Eqs. (5.11) and (5.12).

We assume that the RTNs are stationary random processes. The autocorrelation function of each RTN can be written as

$$\langle \nu_k(t)\nu_k(0)\rangle = \frac{v_k^2\, e^{-\gamma_k|t|}}{\cosh^2(\beta E_k/2)} + \langle \nu_k\rangle^2, \tag{5.18}$$

where

$$\langle \nu_k\rangle = -v_k \tanh(\beta E_k/2), \tag{5.19}$$

is the mean value of the RTN. The angular brackets $\langle\cdots\rangle$ indicate averaging over different realizations of the RTN. A detailed derivation of this formula can be found in App. 5.A. It is important to note that even for $t \to \infty$, the autocorrelation function has a non-vanishing component proportional to $\langle \nu_k\rangle^2$. This nonzero mean value results in a shift of the qubit Larmor frequency given by

$$\begin{aligned} \delta\omega_0 &= \langle \omega_Q(t)\rangle \\ &= \sum_k^n v_k \tanh(\beta E_k/2). \end{aligned} \tag{5.20}$$

The RTN variance can be readily obtained from Eq. (5.18) as

$$\langle \nu_k^2\rangle - \langle \nu_k\rangle^2 = \frac{v_k^2}{\cosh^2(\beta E_k/2)}. \tag{5.21}$$

As shown in Fig. 5.2, at low temperatures when $\beta E_k \to \infty$ the RTN variance decays exponentially as $\sim \exp(-\beta E_k)$, and the contribution of the RTN to the total noise becomes negligible.

The spectral density of each RTN is defined as [40]

$$\begin{aligned} S_k(\omega) &= \frac{v_k^2}{2\pi}\int_{-\infty}^{\infty} dt\, \left[\langle \xi_k(t)\xi_k(0)\rangle - \langle \xi_k\rangle^2\right] e^{-i\omega t} \\ &= \frac{v_k^2}{\cosh^2(\beta E_k/2)} \cdot \frac{\gamma_k}{\pi} \cdot \frac{1}{\gamma_k^2+\omega^2}. \end{aligned} \tag{5.22}$$

The value of $S_k(\omega)$ remains almost constant for $\omega \ll \gamma_k$, while it scales with frequency as $S_k(\omega) \sim 1/\omega^2$ for $\omega \gg \gamma_k$. The total noise spectral density, given by

$$S(\omega) = \sum_k^n S_k(\omega), \tag{5.23}$$

depends on the distribution of the detuning energy ϵ_k and tunneling amplitude Δ_k of the TLFs. The conventional TLF model assumes a uniform distribution of detuning energy ϵ_k and a log-uniform distribution of tunneling amplitude Δ_k [24, 25]. This results in a log-uniform distribution of the average switching rate γ_k, and therefore, the noise spectral density takes the form $S(\omega) \sim 1/\omega$ [41]. However, it is unclear whether the distribution of TLF parameters in quantum dot devices is the same as

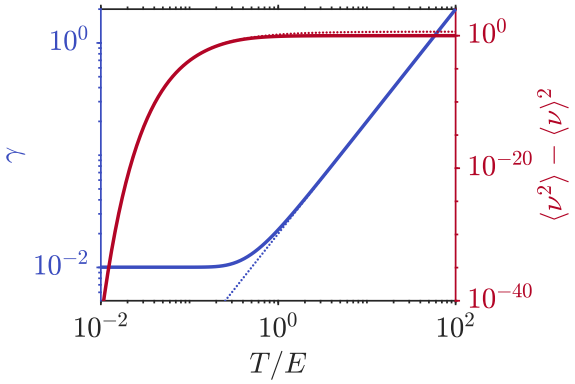

Figure 5.2: Temperature dependence of the average switching rate γ (solid blue) and variance $\langle\nu^2\rangle - \langle\nu\rangle^2$ (solid red) of a single TLF as described by Eqs. (5.13) and (5.21), respectively. The TLF parameters are $E = 1$ K, $\Delta = 0.1$ s^{-1}, $J_0 = 1$ s^2, and $v = 1$ s^{-1}. As $T/E \to 0$, the TLF freezes in the ground state and the average rate converges to the constant value $J_0\Delta^2 E$. In this limit, the variance decays as $\sim \exp(-E/T)$ (dotted red). As $T/E \to \infty$, the excitation and relaxation rates of the TLF become equal. The average rate then scales linearly with temperature, i.e., $\gamma \sim T$ (dotted blue). This average rate is half the TLF-phonon spontaneous emission rate.

that in bulk dielectrics. In this study, we consider different distributions of detuning energy ϵ_k, while maintaining the log-uniform distribution of tunneling amplitudes Δ_k, to replicate the experimentally observed $1/\omega$ spectral density [42, 43].

Using the simplified system Hamiltonian given in Eq. (5.16), we now present the formulas for the qubit Ramsey and echo decay. We assume the control pulses are ideal and instantaneous [44]. In the Ramsey experiment, the qubit is initialized in the state $(|0\rangle + |1\rangle)/\sqrt{2}$, and is measured in the x-basis after a variable delay time t. The implementation of the echo experiment is identical, except for a π rotation around the x axis at time $t/2$. The qubit Ramsey decay can be written as

$$F_{\mathrm{R}}(t) = \langle \exp[i \int_0^t ds\, \omega_{\mathrm{Q}}(s)] \rangle. \tag{5.24}$$

The π rotation in the echo experiment effectively changes the sign of the noise $\omega_{\mathrm{Q}}(t)$ and can be written as

$$F_{\mathrm{H}}(t) = \langle \exp[i \int_0^{t/2} ds\, \omega_{\mathrm{Q}}(s) - i \int_{t/2}^t ds\, \omega_{\mathrm{Q}}(s)] \rangle. \tag{5.25}$$

Since the RTNs are independent, the Ramsey/echo decay can be written as

$$F_{\mathrm{R/H}}(t) = \prod_k^n f_{\mathrm{R/H}}^{(k)}(t), \tag{5.26}$$

where $f_{\mathrm{R/H}}^{(k)}(t)$ is the Ramsey/echo decay induced by the k'th RTN.

The Ramsey and echo decay induced by a single RTN can be calculated by combining the rate equations of the RTN with the Bloch equations of the qubit for constant RTN states (for details, see Ch. 2). The Ramsey decay induced by a single RTN reads [45]

$$f_{\mathrm{R}}(t) = \exp(-\Gamma t)\left[\cosh(At) + \frac{\Gamma}{A}\sinh(At)\right], \tag{5.27}$$

where $\Gamma = \gamma - iv\delta\gamma/2\gamma$, $A = (\gamma^2 - iv\delta\gamma - v^2)^{\frac{1}{2}}$, and $\delta\gamma = \gamma_\downarrow - \gamma_\uparrow$. The echo decay by a single RTN can be written as

$$\begin{aligned} f_{\mathrm{H}}(t) =& e^{-\gamma t}[\cosh(At/2)\cosh(A^*t/2) \\ &+ \frac{v^2+\gamma^2}{A^*A}\sinh(At/2)\sinh(A^*t/2) \\ &+ \frac{\Gamma}{A}\sinh(At/2)\cosh(A^*t/2) \\ &+ \frac{\Gamma^*}{A^*}\sinh(A^*t/2)\cosh(At/2)]. \end{aligned} \tag{5.28}$$

Here, we dropped the index k labeling the RTN for clarity. The Ramsey and echo decay times, T_2^* and T_2^{H}, are defined via

$$F_{\mathrm{R}}(\mathcal{B}; T_2^*) = 1/e, \tag{5.29}$$

and

$$F_{\mathrm{H}}(\mathcal{B}; T_2^{\mathrm{H}}) = 1/e. \tag{5.30}$$

The model developed in this section generalizes the framework from Ch. 4, incorporating both the effects of the phonon bath temperature and the microscopic properties of TLFs. In general, the detuning energy of the TLF, ϵ, is not necessary zero, nor is it guaranteed that the temperature, T, is significantly larger than the TLF energy, E. Therefore, the TLF cannot always be approximated by a symmetric RTN signal. However, at high temperatures, where $T/E \gg 1$, the difference between the relaxation and excitation rates $\delta\gamma$ approaches 0. In this limit, Eqs. (5.27) and (5.28) simplify to the Ramsey and echo decay induced by symmetric RTN, as described in Ch. 4 and in Refs. [45–48].

The simplified system Hamiltonian in this chapter [Eq. (5.16)] closely resembles the system Hamiltonian from Ch. 4 [Eq. (4.3)], and the Ramsey and echo decay calculations follow similar methods (see Ch. 2). However, by expressing the excitation and relaxation rates of the asymmetric RTN, $\gamma_\uparrow$ and $\gamma_\downarrow$, in terms of the tunneling amplitude Δ, detuning energy ϵ, and phonon bath temperature T, a more accurate description of the TLF behavior in different regimes is achieved. This model, in particular, enables the study of the regime where a TLF is frozen in its ground state at temperatures $T \ll E$, and the transition to the regime where the TLF rates saturate to a constant common value for temperatures $T \gg E$ (see Fig. 5.2).

Analyzing qubit decoherence induced by an ensemble of TLFs is highly complex, as the excitation and relaxation rates depend on distributions of tunneling

amplitudes Δ and detuning energies ϵ, neither of which are predetermined in the experimental setup described in Ref. [11]. Due to the likely finite dispersion of TLF energies, TLFs exhibit a range of dynamics at any given temperature, from inactive to saturated, making it challenging to approximate the qubit decoherence caused by the entire ensemble, given in Eq. (5.26). In the following section, we employ a numerical approach to explore various distributions of these parameters, aiming to reproduce both the qubit frequency shift with temperature reported in Ref. [11] and the minimal temperature dependence of Ramsey and echo decay times, T_2^* and T_2^{H}, observed in experiments.

5.3. Numerical simulations

This section presents the results from the numerical simulations. We aim to determine whether the model outlined in the previous section can replicate both a frequency shift similar to experimental observations and Ramsey and echo decay times that are not affected by temperature. We explore two cases: (*i*) a TLF bath tailored to replicate temperature-insensitive Ramsey and echo decay times, and (*ii*) a TLF bath tailored to match the observed frequency shift in experiments.

Figure 5.3 shows the numerical simulation results for case (*i*). We consider a normal distribution of TLF detuning energies with a mean value (1 mK) that is much smaller than the lowest temperature in our simulations (0.1 K). This choice of detuning energies guarantees that the TLFs are already saturated at 0.1 K (see Fig. 5.2), and their variance, $\langle \nu^2 \rangle - \langle \nu \rangle^2$, only negligibly increases at higher temperatures. We consider log-uniformly distributed tunneling amplitudes giving rise to a $1/f$ noise spectral density. We observe in Fig. 5.3(a) that increasing the temperature mainly leads to increased lower and higher frequency cutoffs. The temperature dependence of the Ramsey and echo decay times, shown in Figs. 5.3(b) and (c), is comparable to the experimental observations [for Ramsey decay times, see Fig. 5.6(b)].

The temperature dependence of the qubit frequency shift, based on the bath parameters from Fig. 5.3, is shown in Fig. 5.4. Figure 5.4 presents the qubit frequency shift for coupling strengths that are either (a) all positive or (b) equally likely to be positive or negative. The sign of the coupling strength v is determined by the spatial configuration of the electric dipole moments of the TLFs and the Larmor frequency shift they induce depending on deformations of the orbital state of the dot electron within an inhomogeneous magnetic field. For example, for a TLF with a coupling strength of magnitude $|v|$, if the TLF in its ground state induces a positive (or negative) frequency shift, the coupling strength v is considered positive (or negative). Some of the curves in Fig. 5.4(b) have a non-monotonic temperature dependence, and the qubit frequency shift can be negative. In both cases, the frequency shifts are approximately an order of magnitude smaller than experimental observations (see Fig. 3.2). Choosing larger values for the coupling strengths results in a more accurate quantitative agreement between the simulation and the experimental results. However, this approach would also lead to lower T_2^* values than those observed experimentally.

The noise spectral density and the Ramsey and echo decay times corresponding to case (*ii*) are shown in Fig. 5.5. The bath is now modeled by two types of TLFs,

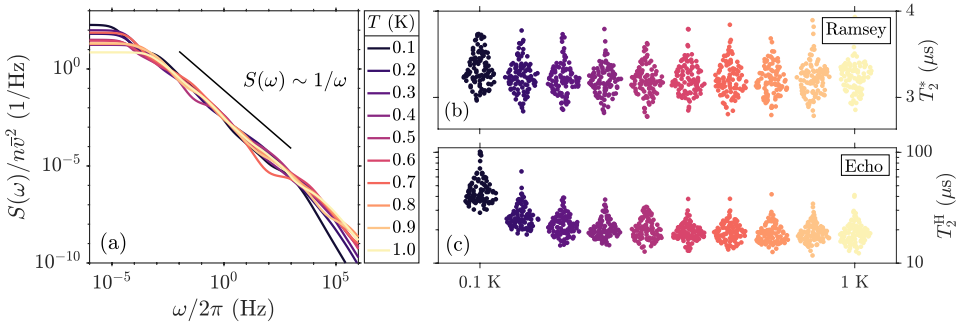

Figure 5.3: Spectral density, Ramsey decay time, T_2^*, and echo decay time, T_2^{H}, for various bath samples at ten different temperatures linearly spaced between 0.1 K and 1 K. Each bath sample consists of 40 TLFs with log-uniformly distributed tunneling amplitudes Δ between $\Delta_m = 10^{-5}$ s^{-1} and $\Delta_M = 10$ s^{-1}, normally distributed detuning energies ϵ with mean 10^{-3} K and deviation 10^{-4} K, and normally distributed coupling strengths v with mean 8×10^4 s^{-1} and deviation 10^4 s^{-1}. The constant $J_0 = 2 \times 10^6$ s^2. (a) Spectral densities of individual bath samples, each at a specific temperature. The spectra scale with frequency as $1/\omega$ between the lower and higher cutoffs. (b) Ramsey decay time data points for 100 bath samples at each temperature. (c) Echo decay time data points for each bath sample. Horizontal jitters in (b) and (c) emulate the distribution of coherence times T_2^* and T_2^{H}.

namely an A and B bath of TLFs. The TLFs from bath A are positively coupled to the qubit, while the TLFs from bath B are negatively coupled. Positive or negative signs of the coupling strengths do not affect the spectral density, the Ramsey, and the echo decay [see Eqs. (5.22), (5.27), and (5.28)]. However, the different signs give rise to a non-monotonic qubit frequency shift shown in Fig. 5.6 [see Eq. (5.20)].

We randomly sample TLFs from bath A or bath B, with probabilities $P_A = 60\%$ and $P_B = 1 - P_A = 40\%$. The detuning energies of A TLFs are normally distributed with mean 0.1 K and deviation 0.05 K. The tunneling amplitudes of A TLFs are log-uniformly distributed between 0.05 K and 0.15 K. The detuning energies of B TLFs are normally distributed with mean 0.5 K and deviation 0.05 K. The tunneling amplitudes of B TLFs are log-uniformly distributed between 0.45 K and 0.55 K. This choice of tunneling amplitudes and detuning energies results in energies E of TLFs from the A and B baths approximately concentrated around 0.1 K and 0.5 K. This results in a positive shift of the qubit frequency with temperature up to ≈ 0.5 K and its decline beyond this point (see Fig. 5.6). The simulated frequency shifts shown in Fig. 5.6 exhibit some agreement with the experimental data presented in Fig. 3.2. However, the simulated Ramsey and echo decay times, T_2^* and T_2^{H}, show a significant decrease with increasing temperature, which is not observed in the experiments.

5.4. Discussion

According to experimental observations the Larmor frequency of semiconductor spin qubits increases as the temperature rises [11], while the coherence times remain approximately unaffected by temperature variations [5, 6, 8, 11]. Our goal was to investigate whether a phenomenological model of tunneling two-level fluctuators

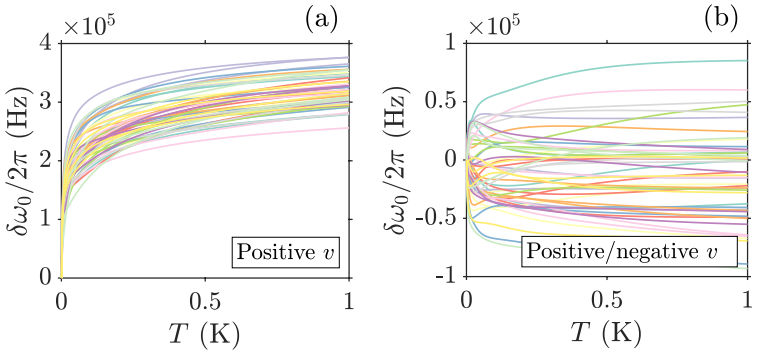

Figure 5.4: Monotonic and non-monotonic qubit frequency shift corresponding to various bath samples. The bath samples are the same as those in Fig. 5.3, consisting of 40 TLFs with log-uniformly distributed tunneling amplitudes Δ between $\Delta_m = 10^{-5}$ s^{-1} and $\Delta_M = 10$ s^{-1}, normally distributed detuning energies ϵ with mean 10^{-3} K and deviation 10^{-4} K, and normally distributed coupling strengths v with mean 8×10^4 s^{-1} and deviation 10^4 s^{-1}. (a) Monotonic qubit frequency shift for positive values of the coupling constants v. (b) Non-monotonic qubit frequency shift for positive and negative values of v. The probability of sampling a positive v is 50 %. The qubit frequency shift in (a) and (b) is calculated using Eq. (5.20).

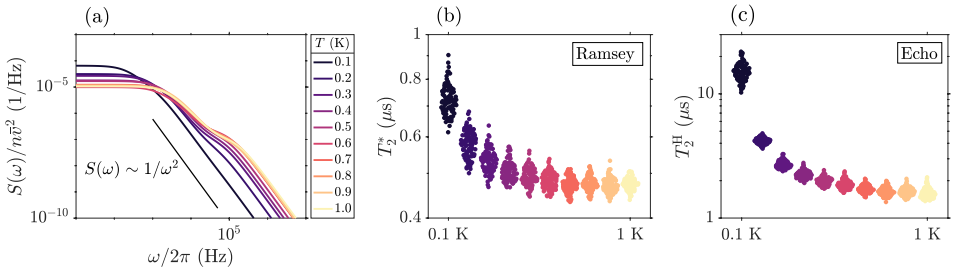

Figure 5.5: Spectral density, Ramsey and echo decay times, T_2^* and T_2^{H}, for various bath samples consisting of two sub-baths, referred to as A and B baths in the main text. The energies of the TLFs in the A and B baths are peaked around 0.1 K and 0.5 K. (a) Spectral density of sample TLF baths at different temperatures, showing a broadened Lorentzian peak at around ≈ 1 kHz for the A TLFs and a second peak at around ≈ 100 kHz for the B TLFs. (b) and (c) Ramsey and echo decay times for various bath samples at different temperatures, with each data point indicating the coherence time, T_2^* or T_2^{H}, corresponding to a specific bath sample. The jitters in the horizontal direction in (b) and (c) are artificially introduced to emulate the distribution of coherence times.

coupled to acoustic phonons could explain these effects. The theoretical model can potentially account for the shift in the qubit Larmor frequency with temperature by considering the time-averaged states of the TLFs in thermal equilibrium with the phonon bath. Additionally, the model links the temperature dependence of the Ramsey and echo decay times to the dynamics of TLFs, which rely on the phonon bath temperature.

We performed numerical simulations to evaluate how well the model could replicate the experimental observations. We explored two different scenarios. In the

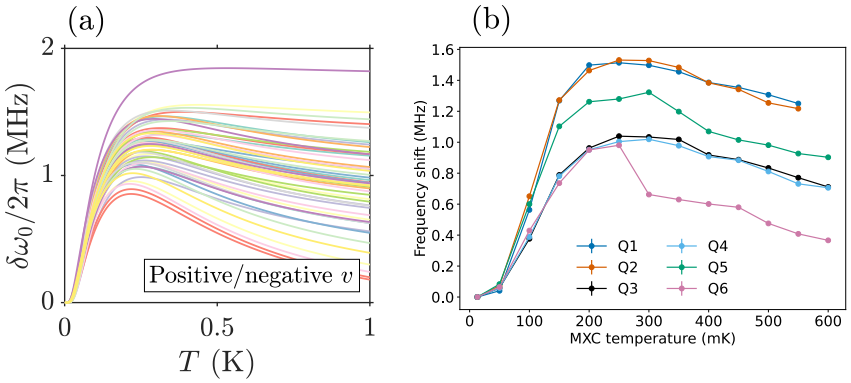

Figure 5.6: (a) Qubit frequency shift due to a TLF bath consisting of two sub-baths A and B, where the A TLFs are positively coupled and the B TLFs are negatively coupled to the qubit. The coupling strengths v are normally distributed with mean 5×10^5 s^{-1} and deviation 10^5 s^{-1}, with a 60% probability of sampling an A TLF. The detuning energies of A TLFs are normally distributed with mean 0.1 s^{-1} and deviation 0.05 s^{-1}, while the tunneling amplitudes of B TLFs are log-uniformly distributed between 0.05 s^{-1} and 0.15 s^{-1}. The detuning energies of B TLFs are normally distributed with mean 0.5 s^{-1} and deviation 0.05 s^{-1}, while the tunneling amplitudes of B TLFs are log-uniformly distributed between 0.45 s^{-1} and 0.55 s^{-1}. The energies of A and B TLFs peak around 0.1 K and 0.5 K. The constant $J_0 = 2 \times 10^6$ s^2. (b) Experimentally measured frequency shift of the spin qubits. This panel is taken from Ref. [11].

first case, we adjusted the model parameters to reproduce temperature-insensitive coherence times, but the frequency shift predicted by the model was an order of magnitude smaller than what was observed in experiments. In the second case, we modified the bath parameters to obtain a qubit frequency shift similar to what was observed in experiments, but this resulted in a decline in coherence times with temperature, which was not observed in experiments.

A comparable phenomenological model was recently proposed in Ref. [13]. Reference [13] also attributes the frequency shift to the equilibrium electric field resulting from the electric dipoles of TLFs, which linearly couples to the qubit, similar to our model. However, this model takes into account the spatial distribution of the electric dipoles and their internal interactions. In our simplified model, we considered a normal distribution of coupling strengths and the precise distribution of these couplings is determined by the spatial distribution of the electric dipoles. Unlike our work, Ref. [13] does not study the frequency shift and the coherence times simultaneously. It should be noted that neither model takes into account other potential sources of noise or structural deformations of the device caused by heating. It is possible that the observed frequency shift may be due to structural deformations, and that the measured T_2^* and T_2^{H} values are not primarily shortened by intrinsic noise, but rather by extrinsic noise injected by the instrumentation.

5.5. Conclusion and outlook

We studied the dephasing times and frequency shifts of heated semiconductor spin qubits by utilizing a phenomenological model of charge noise. Our model considered the charge noise arising from switching electric dipoles of an aggregate of TLFs coupled to acoustic phonons. Through numerical simulations, we aimed to replicate the experimentally observed qubit frequency shift with temperature, as well as temperature-insensitive Ramsey and echo decay times. Our results revealed that the model parameters could be adjusted to replicate each of these effects individually, but not simultaneously.

While an extensive exploration of the model's parameter space may reproduce observed effects, the intricate design of spin qubit devices requires consideration of other temperature-dependent mechanisms. One promising research direction is the study of multiple phonon baths at different temperatures to examine the thermodynamics of heat flow and transient pulse-induced resonance shifts. Finally, understanding all temperature-dependent sources of noise, including noise of the metallic gates, could narrow the research scope and aid in comprehending the qubit frequency shift and the stability with temperature of the coherence times.

5.A. Autocorrelation function

In this Section, we calculate the autocorrelation function of the noise $\nu(t) = v\,\xi(t)$. We begin with the rate equations for the single RTN $\xi(t)$. The probabilities of the RTN to be in the state $+1$ or -1 at time t, are denoted by $P_e(t)$ and $P_g(t)$. The rate equations may be written as

$$\dot{P}(t) = \mathbb{M}P(t), \tag{5.31}$$

where

$$\mathbb{M} = \begin{bmatrix} -\gamma_\downarrow & \gamma_\uparrow \\ \gamma_\downarrow & -\gamma_\uparrow \end{bmatrix}, \tag{5.32}$$

and $P(t) = [P_e(t),\ P_g(t)]^T$. The excitation and relaxation rates, $\gamma_\uparrow$ and $\gamma_\downarrow$, are given in Eqs. (5.11) and (5.12). Equation 5.31 can be solved by exponentiation. It follows

$$P(t) = e^{t\mathbb{M}}P(0). \tag{5.33}$$

We write

$$e^{t\mathbb{M}} = \begin{bmatrix} P_{e|e} & P_{e|g} \\ P_{g|e} & P_{g|g} \end{bmatrix}. \tag{5.34}$$

The autocorrelation function can be written as

$$\begin{aligned} \langle \nu(0)\nu(t)\rangle &= v^2[P_e(\infty)P_{e|e}(t) - P_e(\infty)P_{e|g}(t) - P_g(\infty)P_{g|e}(t) + P_g(\infty)P_{g|g}(t)] \\ &= \frac{v^2\ e^{-\gamma|t|}}{\cosh^2(\beta E/2)} + \langle\nu\rangle^2, \end{aligned} \tag{5.35}$$

where $\langle\nu\rangle = -v\tanh(\beta E/2)$. Here, $P_e(\infty)$ and $P_g(\infty)$ are the probabilities for the random process $\xi(t)$ to be in the excited or the ground state on average.

References

[1] B. M. Terhal, *Quantum error correction for quantum memories,* Rev. Mod. Phys. **87**, 307 (2015).

[2] S. G. J. Philips, M. T. Mądzik, S. V. Amitonov, S. L. de Snoo, M. Russ, N. Kalhor, C. Volk, W. I. L. Lawrie, D. Brousse, L. Tryputen, B. P. Wuetz, A. Sammak, M. Veldhorst, G. Scappucci, and L. M. K. Vandersypen, *Universal control of a six-qubit quantum processor in silicon,* Nature **609**, 919 (2022).

[3] K. Takeda, A. Noiri, T. Nakajima, T. Kobayashi, and S. Tarucha, *Quantum error correction with silicon spin qubits,* Nature **608**, 682 (2022).

[4] L. M. K. Vandersypen, H. Bluhm, J. S. Clarke, A. S. Dzurak, R. Ishihara, A. Morello, D. J. Reilly, L. R. Schreiber, and M. Veldhorst, *Interfacing spin qubits in quantum dots and donnors–hot, dense, and coherent,* npj Quantum Inf. **3**, 34 (2017).

[5] C. H. Yang, R. C. C. Leon, J. C. C. Hwang, A. Saraiva, T. Tanttu, W. Huang, J. Camirand Lemyre, K. W. Chan, F. E. Tan, K. Y. Hudson, K. M. Itoh, M. Morello, A. Pioro-Ladrière, and A. S. Laucht, A. Dzurak, *Operation of a silicon quantum processor unit cell above one Kelvin,* Nature **580**, 350 (2020).

[6] J. Y. Huang, R. Y. Su, W. H. Lim, M. Feng, B. van Straaten, B. Severin, W. Gilbert, N. D. Stuyck, T. Tanttu, S. Serrano, J. D. Cifuentes, I. Hansen, A. E. Seedhouse, E. Vahapoglu, N. V. Abrosimov, H.-J. Pohl, M. L. W. Thewalt, F. E. Hudson, C. C. Escott, N. Ares, S. D. Bartlett, A. Morello, A. Saraiva, A. Laucht, A. S. Dzurak, and C. H. Yang, *High-fidelity operation and algorithmic initialisation of spin qubits above one kelvin,* (2023), arXiv:2308.02111 [quant-ph] .

[7] L. Petit, J. M. Boter, H. G. J. Eenink, G. Droulers, M. L. V. Tagliaferri, R. Li, D. P. Franke, K. J. Singh, J. S. Clarke, R. N. Schouten, V. V. Dobrovitski, L. M. K. Vandersypen, and M. Veldhorst, *Spin lifetime and charge noise in hot silicon quantum dot qubits,* Phys. Rev. Lett. **121**, 076801 (2018).

[8] L. Petit, H. G. J. Eeenink, M. Russ, W. I. L. Lawrie, N. W. Hendrickx, S. G. J. Philips, J. S. Clarke, L. M. K. Vandersypen, and M. Veldhorst, *Universal quantum logic in hot silicon qubits,* Nature **580**, 355 (2020).

[9] L. Petit, M. Russ, G. H. G. J. Eenink, W. I. L. Lawrie, J. S. Clarke, L. M. K. Vandersypen, and M. Veldhorst, *Design and integration of single-qubit rotations and two-qubit gates in silicon above one Kelvin,* Commun. Mat. **3**, 82 (2022).

[10] L. C. Camenzind, S. Geyer, A. Fuhrer, R. J. Warburton, D. M. Zumbürl, and A. V. Kuhlmann, *A hole spin qubit in a fin field-effect transistor above 4 kelvin,* Nat. Electron. **5**, 178 (2022).

[11] B. Undseth, O. Pietx-Casas, E. Raymenants, M. Mehmandoost, M. T. Mądzik, S. G. J. Philips, S. L. de Snoo, D. J. Michalak, S. V. Amitonov, L. Tryputen, B. P. Wuetz, V. Fezzi, D. D. Esposti, A. Sammak, G. Scappucci, and L. M. K. Vandersypen, *Hotter is easier: unexpected temperature dependence of spin qubit frequencies,* (2023), arXiv:2304.12984 [cond-mat.mes-hall] .

[12] K. Takeda, J. Yoneda, T. Otsuka, T. Nakajima, M. R. Delbecq, G. Allison, Y. Hoshi, N. Usami, K. M. Itoh, S. Oda, T. Kodera, and S. Tarucha, *Optimized electrical control of a Si/SiGe spin qubit in the presence of an induced frequency shift,* npj Quantum Inf. **4**, 54 (2018).

[13] Y. Choi and R. Joynt, *Interacting random-field dipole defect model for heating in semiconductor-based qubit devices,* (2023), arXiv:2308.00711 [quant-ph] .

[14] E. J. Connors, JJ Nelson, H. Qiao, L. F. Edge, and J. M. Nichol, *Low-frequency charge noise in Si/SiGe quantum dots,* Phys. Rev. B **100**, 165305 (2019).

[15] U. Güngördü and J. P. Kestner, *Indications of a soft cutoff frequency in the charge noise of a si/sige quantum dot spin qubit,* Phys. Rev. B **99**, 081301 (2019).

[16] S. Ahn, S. Das Sarma, and J. P. Kestner, *Microscopic bath effects on noise spectra in semiconductor quantum dot qubits,* Phys. Rev. B **103**, L041304 (2021).

[17] D. Mickelsen, H. M. Carruzzo, S. N. Coppersmith, and C. C. Yu, *Effects of temperature fluctuations on charge noise in quantum dot qubits,* (2023), arXiv:2305.14515 [cond-mat.mes-hall] .

[18] R. E. Throckmorton and S. D. Sarma, *A generalized model of the noise spectrum of a two-level fluctuator in the presence of an electron subbath,* (2023), arXiv:2305.14348 [cond-mat.mes-hall] .

[19] D. L. Mickelsen, H. M. Carruzzo, and C. C. Yu, *Interacting two-level systems as a source of 1/f noise in silicon quantum dot qubits,* (2023), arXiv:2308.13674 [cond-mat.mes-hall] .

[20] G. Burkard, T. D. Ladd, A. Pan, J. M. Nichol, and J. R. Petta, *Semiconductor spin qubits,* Rev. Mod. Phys. **95**, 025003 (2023).

[21] E. Paladino, Y. M. Galperin, G. Falci, and B. L. Altshuler, $1/f$ *noise: Implications for solid-state quantum information,* Rev. Mod. Phys. **86**, 361 (2014).

[22] A. M. J. Zwerver, T. Kraehenmann, T. F. Watson, L. Lampert, H. C. George, R. Pillarisetty, S. A. Bojarski, P. Amin, S. V. Amitonov, J. M. Boter, R. Caudillo, D. Correas-Serrano, J. P. Dehollain, G. Droulers, E. M. Henry, R. Kotlyar, M. Lodari, F. Lüthi, D. J. Michalak, B. K. Mueller, S. Neyens, J. Roberts, N. Samkharadze, G. Zheng, O. K. Zietz, G. Scappucci, M. Veldhorst, L. M. K. Vanderypen, and J. S. Clarke, *Qubits made by advanced semiconductor manufacturing,* Nat. Electron. **5**, 184 (2022).

[23] C. Slichter, *Principles of Magnetic Resonance*, Springer Series in Solid-State Sciences (Springer Berlin Heidelberg, 1996).

[24] P. W. Anderson, B. I. Halperin, and C. M. Varma, *Anomalous low-temperature thermal properties of glasses and spin-glasses,* Philos. Mag. **25**, 1 (1972).

[25] W. A. Phillips, *Tunneling states in amorphous solids,* J. Low Temp. Phys. **7**, 351 (1972).

[26] J. Jäckle, *On the ultrasonic attenuation in glasses at low temperatures,* Zeitschrift für Physik A Hadrons and nuclei **257**, 212 (1972).

[27] W. A. Phillips, *Two-level states in glasses,* Reports on Progress in Physics **50**, 1657 (1987).

[28] A. J. Leggett, S. Chakravarty, A. T. Dorsey, M. P. A. Fisher, A. Garg, and W. Zwerger, *Dynamics of the dissipative two-state system,* Rev. Mod. Phys. **59**, 1 (1987).

[29] S. Kogan, *Electronic Noise and Fluctuations in Solids* (Cambridge University Press, Cambridge, England, 1996).

[30] A. Würger, *From coherent tunneling to relaxation* (Springer Berlin, 1997).

[31] P. Esquinazi, *Tunneling Systems in Amorphous and Crystalline Solids* (Springer Berlin, 1998).

[32] C. Enss and S. Hunklinger, *Low-Temperature Physics* (Springer Berlin, Heidelberg, 2005).

[33] U. Weiss, *Quantum Dissipative Systems*, 4th ed. (WORLD SCIENTIFIC, 2012).

[34] H. J. Wold, H. Brox, Y. M. Galperin, and J. Bergli, *Decoherence of a qubit due to either a quantum fluctuator, or classical telegraph noise,* Phys. Rev. B **86**, 205404 (2012).

[35] X. You, A. A. Clerk, and J. Koch, *Positive- and negative-frequency noise from an ensemble of two-level fluctuators,* Phys. Rev. Res. **3**, 013045 (2021).

[36] G. Ramon and X. Hu, *Decoherence of spin qubits due to a nearby charge fluctuator in gate-defined double dots,* Phys. Rev. B **81**, 045304 (2010).

[37] J. K. Gamble, M. Friesen, S. N. Coppersmith, and X. Hu, *Two-electron dephasing in single Si and GaAs quantum dots,* Phys. Rev. B **86**, 035302 (2012).

[38] Y. Tokura, W. G. van der Wiel, T. Obata, and S. Tarucha, *Coherent single electron spin control in a slanting Zeeman field,* Phys. Rev. Lett. **96**, 047202 (2006).

[39] M. Pioro-Ladriere, T. Obata, Y. Tokura, Y.-S. Shin, T. Kubo, K. Yoshida, T. Taniyama, and S. Tarucha, *Electrically driven single-electron spin resonance in a slanting Zeeman field,* Nat. Phys. **4**, 776 (2008).

[40] R. Kubo, M. Toda, and N. Hashitsume, *Statistical Physics II: Nonequilibrium Statistical Mechanics* (Springer, Heidelberg, Germany, 1991).

[41] C. Müller, J. H. Cole, and J. Lisenfeld, *Towards understanding two-level-systems in amorphous solids: insights from quantum circuits,* Rep. Prog. Phys. **82**, 124510 (2019).

[42] J. Yoneda, K. Takeda, T. Otsuka, T. Nakajima, M. R. Delbecq, G. Allison, T. Honda, T. Kodera, S. Oda, Y. Hoshi, N. Usami, K. M. Itoh, and S. Tarucha, *A quantum-dot spin qubit with coherence limited by charge noise and fidelity higher than 99.9%,* Nature Nanotech. **13**, 102 (2018).

[43] E. J. Connors, J. Nelson, and J. M. Nichol, *Charge-noise spectroscopy of Si/SiGe quantum dots via dynamically-decoupled exchange oscillations,* Nat. Commun. **13**, 940 (2022).

[44] L. Viola and S. Lloyd, *Dynamical suppression of decoherence in two-state quantum systems,* Phys. Rev. A **58**, 2733 (1998).

[45] E. Paladino, L. Faoro, G. Falci, and R. Fazio, *Decoherence and $1/f$ noise in Josephson qubits,* Phys. Rev. Lett. **88**, 228304 (2002).

[46] G. Zhidomirov and K. M. Salikhov, *Contribution to the theory of spectral diffusion in magnetically diluted solids,* Sov. Phys. JETP **29**, 1037 (1969).

[47] R. de Sousa and S. Das Sarma, *Theory of nuclear-induced spectral diffusion: Spin decoherence of phosphorus donors in Si and GaAs quantum dots,* Phys. Rev. B **68**, 115322 (2003).

[48] Y. M. Galperin, B. L. Altshuler, J. Bergli, and D. V. Shantsev, *Non-Gaussian low-frequency noise as a source of qubit decoherence,* Phys. Rev. Lett. **96**, 097009 (2006).

[49] O. Pietx-Casas, *Private communication,* .

6

Conclusion and Outlook

The primary goal of this thesis was to gain new insights into the dynamics of spin qubits in their actual environment. To achieve this, we relied on theoretical models as our main tools. The development of these models were primarily stimulated by experimental findings. In this section, we will discuss the findings of our research from a broad perspective and suggest potential areas for future investigation.

Excluding the introductory Chapters 1 and 2, the following are the conclusions for each thesis chapter:

- Chapter 3 presents experimental findings on the nonlinear scaling of the spin qubit's Rabi frequency with the amplitude of the microwave drive that is in resonance with the qubit Larmor frequency. The chapter also reports on a novel crosstalk mechanism, where the Rabi frequency of a spin qubit changes as the drive of an adjacent qubit is turned on. In this chapter, a phenomenological model is proposed to describe both the nonlinear response and the crosstalk. This model merely relates the electrical driving to the observed effects, and the microscopic origins of the effects remain elusive.

- Chapter 4 explores the qubit dephasing, as measured in the Ramsey and Hahn echo experiments, in a sparse bath of TLFs with $1/f$ spectral density. The chapter demonstrates that the bath density, defined as the ratio of the number of TLFs over the logarithmic width of the distribution of TLF switching rates, is a crucial parameter in determining the variability of the qubit dephasing. It is observed that in sparse baths, where the bath density is small, the qubit dephasing experiences considerable variations from sample to sample. Furthermore, the chapter reveals that in certain parameter regimes, the qubit decoherence is dominated by a few TLFs, referred to as exceptional defects. Eliminating these TLFs results in a substantial improvement in coherence times. Moreover, when the distribution of TLF coupling strengths is narrowly concentrated around a value significantly greater than the minimum TLF switching rate, the Ramsey decay in sparse baths exhibits revivals.

- Chapter 5 focuses on the theoretical exploration of the temperature-dependent frequency shift of spin qubits. This work was motivated by the experimental observation of the qubit frequency shift with temperature, reported in Ref. [1]. We employed a phenomenological model that considers charge noise originating from a bath of TLFs in equilibrium with acoustic phonons. The model also establishes a relationship between the phonon bath temperature and the Ramsey and echo decay times, which serves as a self-consistency test for explaining the frequency shift, as these coherence times are largely insensitive to temperature. Through numerical simulations, we found that it is possible to explain either the frequency shift or the temperature-insensitive coherence times by adjusting the model parameters, but not both simultaneously.

The experimental results outlined in Chapter 3 underscore the need for additional research into the spin qubit's environment. The phenomenological model presented in this chapter relates the microwave drivings with the observed qubit dynamics, without offering a deeper understanding of the underlying physical mechanisms. Essentially, this model serves as a transfer function that establishes a nonlinear relationship between the input and output microwave driving(s). Exploring an "open quantum system" perspective could provide further insight into the underlying physical mechanisms behind the observed phenomena. For example, one could examine the interaction of spin qubits with a TLF bath and microwave fields that couple to the electric dipole moments of the TLFs. By activating the microwave field, the TLFs could be driven out of equilibrium, potentially leading to a renormalization of the qubit's Larmor frequency. However, this is a simplified scenario, and a comprehensive understanding of such a complex system would require detailed quantitative investigations.

The scaling of the qubit Rabi frequency with the microwave drive amplitude closely resembles the scaling of the qubit Larmor frequency with the energy delivered to the system via microwave (pre-)pulses [1, 2]. This similarity tentatively suggests that there might be a common physical origin for both effects. Additionally, assuming that TLF defects are present in the spin qubit devices but do not result in the qubit frequency shift with temperature or the nonlinear response of the Rabi frequency with microwave driving, these defects may still play a secondary role in the documented phenomena by transforming electromagnetic radiation to heat. In this case, the mechanical deformation of the heterostructure might be the immediate cause of the frequency shift or nonlinear response. Therefore, it is crucial to explore all possible causes of these effects to develop a comprehensive understanding of the spin qubit's environment.

In Chapter 4, the assumption is made that the properties of TLFs remain constant over time. However, it has been observed that the energy relaxation times of superconducting qubits, which are also affected by TLF-like defects, exhibit fluctuations over time [3]. Therefore, it is reasonable to hypothesize that if the spin qubits are coupled to similar types of defects, then their dephasing times may also fluctuate over time. This presents an opportunity for future research to investigate the dephasing of spin qubits caused by $1/f$ noise from a sparse bath of TLFs whose properties change over time. The switching rates of individual TLFs in an annealed

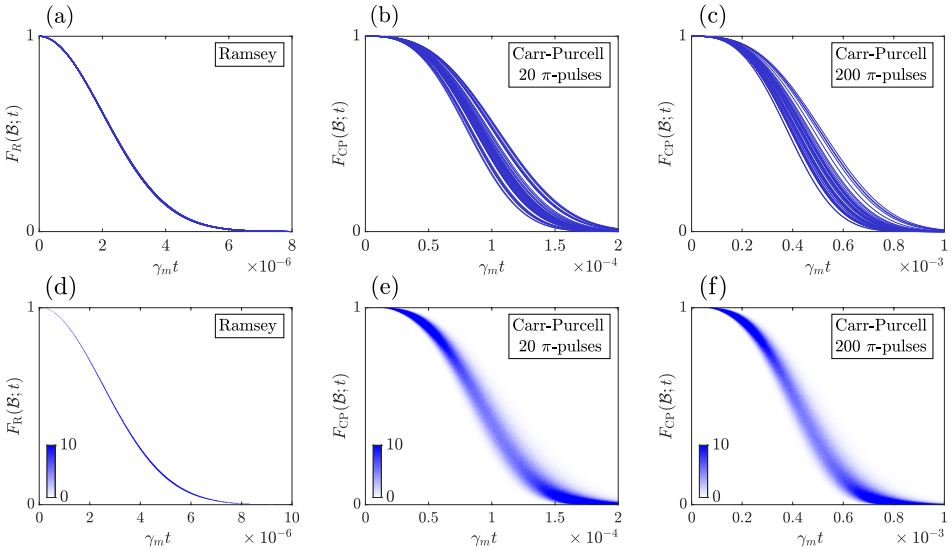

Figure 6.1: Numerical simulations of qubit decoherence in Ramsey and Carr-Purcell experiments for dense TLF baths ($d \approx 8.68$). (a)-(c) Each panel shows qubit decoherence in 50 bath samples. (d)-(f) Estimated probability density of qubit decoherence. Each panel has a resolution of $10^3 \times 10^3$ pixels, and a vertical column of 10^3 pixels at a specific value of $\gamma_m t$ represents a histogram of 10^4 samples of $F_{\mathrm{R}}(\mathcal{B};t)$ or $F_{\mathrm{CP}}(\mathcal{B};t)$. The number of counts in each pixel is divided by 10 to estimate the probability density. The estimated p.d.f. values smaller than 10 are linearly mapped to the color bar, while those greater than 10 are mapped to the darkest shade in the color bar.

bath will take multiple values. It is tempting to presume that in such a bath, the dephasing times of spin qubits may exhibit less sample-to-sample variation. In fact, randomization of TLF energies has been proposed as a technique to decrease the variability of relaxation times in superconducting qubits [4]. This suggests that future research could explore the impact of bath engineering on the dephasing times of spin qubits.

Numerical simulations investigating qubit decoherence in a bath of TLFs have yielded surprising results, some of which are discussed in Ch. 4. Here, we present another unexpected effect that warrants further investigation (for a description of the model system, refer to Ch. 4). We consider 100 symmetric TLFs with switching rates distributed between γ_m and $\gamma_M = 100\gamma_m$. This parameter selection leads to a relatively dense bath with $d \approx 8.68$. The coupling strengths of TLFs are normally distributed with a mean $\bar{v} = 10^5\gamma_m$ and a deviation $\sigma_V = 10^3\gamma_m$. The simulation results for the qubit decoherence in Ramsey and Carr-Purcell experiments is shown in Fig. 6.1. Specifically, Figures 6.1(a) and (d) illustrate that the Ramsey decay remains relatively constant across different bath samples. However, Figures 6.1(b), (c), (e), and (f) show that the application of echo pulses in the Carr-Purcell experiments results in variability of qubit decoherence.

In Chapter 5, we made the assumption that the TLFs couple to a phonon bath that is in thermal equilibrium. However, it is known that the heat introduced by

microwave pulses dissipates to colder reservoirs [1]. To improve upon our model, it would be useful to consider the heat flow between multiple phonon baths. The model presented in Chapter 5 can already be criticized for having too many free parameters, and considering multiple phonon baths adds another layer of complexity and additional free parameters. Therefore, it is also crucial to experimentally characterize the TLFs in the spin qubits' environment [5].

To gain a better understanding of the impact of charge noise on spin qubit decoherence, it is important to investigate the effect of echo pulse sequences. The application of microwave pulses alters the frequencies of spin qubits. This effect can lead to decreased fidelity of single-qubit gates utilized for dynamical decoupling of the qubit from its environment. Consequently, it is imperative to develop new models that consider the imperfections of pulses and non-equilibrium dynamics of the bath induced by the echo pulses themselves, which are intended to enhance coherence times. These models will aid in investigating the efficacy of echo pulse sequences in increasing coherence times while accounting for the adverse effects of pulse imperfections and non-equilibrium qubit environments.

References

[1] B. Undseth, O. Pietx-Casas, E. Raymenants, M. Mehmandoost, M. T. Mądzik, S. G. J. Philips, S. L. de Snoo, D. J. Michalak, S. V. Amitonov, L. Tryputen, B. P. Wuetz, V. Fezzi, D. D. Esposti, A. Sammak, G. Scappucci, and L. M. K. Vandersypen, *Hotter is easier: unexpected temperature dependence of spin qubit frequencies,* (2023), arXiv:2304.12984 [cond-mat.mes-hall] .

[2] B. Undseth, X. Xue, M. Mehmandoost, M. Rimbach-Russ, P. T. Eendebak, N. Samkharadze, A. Sammak, V. V. Dobrovitski, G. Scappucci, and L. M. Vandersypen, *Nonlinear response and crosstalk of electrically driven silicon spin qubits,* Phys. Rev. Appl. **19**, 044078 (2023).

[3] P. V. Klimov, J. Kelly, Z. Chen, M. Neeley, A. Megrant, B. Burkett, R. Barends, K. Arya, B. Chiaro, Y. Chen, A. Dunsworth, A. Fowler, B. Foxen, C. Gidney, M. Giustina, R. Graff, T. Huang, E. Jeffrey, E. Lucero, J. Y. Mutus, O. Naaman, C. Neill, C. Quintana, P. Roushan, D. Sank, A. Vainsencher, J. Wenner, T. C. White, S. Boixo, R. Babbush, V. N. Smelyanskiy, H. Neven, and J. M. Martinis, *Fluctuations of energy-relaxation times in superconducting qubits,* Phys. Rev. Lett. **121**, 090502 (2018).

[4] S. Matityahu, A. Shnirman, and M. Schechter, *Stabilization of qubit relaxation rates by frequency modulation,* Phys. Rev. Applied **16**, 044036 (2021).

[5] F. Ye, A. Ellaboudy, D. Albrecht, R. Vudatha, N. T. Jacobson, and J. M. Nichol, *Characterization of individual charge fluctuators in si/sige quantum dots,* (2024), arXiv:2401.14541 [cond-mat.mes-hall] .

Acknowledgements

I would like to express my gratitude to Viatcheslav Dobrovitski for offering me a PhD position and supervising the projects in this thesis. Dear Slava, I appreciate your guidance and supervision in enhancing my understanding of scientific research. I am grateful for the time you spent elucidating the underlying concepts, engaging in thorough discussions of results, and providing guidance on potential research avenues that could lead to producing interesting, useful results. Your supervision has been instrumental in guiding my progress towards becoming an independent researcher.

I extend my gratitude to Lieven Vandersypen for his support and guidance throughout the PhD. Dear Lieven, I am particularly grateful for the opportunities to participate in experimental projects under your supervision. These experiences have played a significant role in cultivating a practical perspective on semiconductor spin qubit devices. Your insights into scientific research and overall support have been invaluable to me in my journey towards completing my PhD.

I would also like to thank Maximilian Rimbach-Russ for numerous discussions on semiconductor spin qubits and providing support in completing the thesis. Dear Max, I am especially grateful for helping me see the broader scope of the works and suggesting alternative approaches to solving problems. I wish you all the best in your scientific pursuits.

I would like to thank Marja Plas, Chantal Smith, and Laura Elshove for their invaluable assistance with many administrative tasks. I am certain there are many others beyond this list with whom I have not been in direct contact but who have carried out crucial official arrangements, and I extend my gratitude to them as well.

Participating in collaborative projects would not have been possible without the generosity of other researchers at QuTech. I particularly thank Brennan Undseth, Xiao Xue, Oriol Pietx-Casas, Eline Raymenants, and David Michalak for our collaborations. I would also like to thank Marcel Meyer, Brian Paquelet Wuetz and Davide Degli Esposti for interesting discussions on charge noise in semiconductor spin qubit devices.

Attending courses taught by Yuli Nazarov, Barbara Terhal, David DiVincenzo, Jukka Pekkola, and Wolfgang Wernsdorfer has been incredibly refreshing, providing not only new knowledge but also valuable perspectives outside of my own research. I am also grateful to Leonardo DiCarlo and David Elkouss for the opportunity to serve as a teaching assistant. My thanks go to Tim Coopmans, Sebastian de Bone, Ramiro Sagastizabel, Hany Ali and many others with whom I engaged in teaching assistant activities.

I have shared many wonderful moments with colleagues at QuTech and the TU Delft Faculty of Applied Sciences, whether through stimulating lunchtime conversations or memorable gatherings outside of work. I would especially like to thank

Walter Hahn, Fenglei Gu, Tanmoy Chakraborty, Antariksha Das, Arash Ahmadi, Talieh Ghiasi, Brennan Undseth, Oriol Pietx-Casas, Irene Fernandez de Fuentes, Corentin Déprez, Marcel Meyer, Andrea Corna, Stephen Philips, Sjaak van Diepen, Guoji Zheng, Uditendu Mukhopadhyay, Juan Pablo Dehollain, Luca Petit, Sasha Ivlev, Liza Morozova, Alberto Tosato, Amir Sammak, Kenji Capannelli, Hanifa Tidjani, Pablo Cova Farina, Nodar Samkharadze, Mohamed Abobeih, Arian Stolk, Kian van der Enden, Julia brevoord, Christopher Waas, Sander de Snoo, Greg Mazur, Raymond Schouten, Olaf Benningshof, Jason Mensingh, Vinod Narain, Siebe Visser, Hasan Aydin, Kai-Niklas Schymik, Benjamin Pingault, Yang Wang, Thijs Stavenga, Santiago Valles Sanclemente, Nandini Muhusubramanian, Sean van der Meer, Marios Samiotis, Tim Vroomans, Rebecca Gharibaan, Figen Yilmaz, Martijn Zwanenburg, Taryn Stefanski, Siddharth Singh, Damian Kwiatkowski, Siddhant Singh, Nicolas Demetriou, Julius Fischer, Yanik Herrmann, Sebastian Miles, Mert Bockzurt, Juan Daniel Torres and Antonio Manesco.

I was fortunate to have the unwavering support of many friends throughout my PhD years. I am deeply grateful to Maryam Ansar, Negin Latifi, Mahmoudreza Forouhi, Vahid Dolatkhah, Maryam Ghasemi, and Ramin Soltani for their constant encouragement and support.

I am grateful to my parents and brother for their constant presence and support. Dear Maman, Baba, and Milad, your availability, advice, and encouragement on various occasions have been invaluable throughout this journey.

Curriculum Vitæ

Mohammad Mehmandoost

Education

Sep. 2002 – Dec. 2007	BSc in Electrical Engineering University of Guilan, Rasht, Iran
Sep. 2008 – Oct. 2010	MSc in Electrical Engineering Iran University of Science and Technology, Tehran, Iran
Oct. 2014 – Feb. 2017	MSc in Physics Ulm University, Ulm, Germany
Jan. 2018 – Nov. 2024	PhD Physics Technical University of Delft, Delft, The Netherlands

List of Publications

1. **M. Mehmandoost**, V. V. Dobrovitski, *Decoherence induced by a sparse bath of two-level fluctuators: Peculiar features of* $1/f$ *noise in high-quality qubits*, Phys. Rev. Research **6**, 033175 (2024).

2. B. Undseth, O. Pietx-Casas, E. Raymenants, **M. Mehmandoost**, M. T. Madzik, S. G. J. Philips, S. L. de Snoo, D. J. Michalak, S. V. Amitonov, L. Tryputen, B. P. Wuetz, V. Fezzi, D. D. Esposti, A. Sammak, G. Scappucci, and L. M. K. Vandersypen, *Hotter is Easier: Unexpected Temperature Dependence of Spin Qubit Frequencies*, Phys. Rev. X **13**, 041015 (2023).

3. B. Undseth, X. Xue, **M. Mehmandoost**, M. Rimbach-Russ, P. T. Eendebak, N. Samkharadze, A. Sammak, V. V. Dobrovitski, G. Scappucci, and L. M.K. Vandersypen, *Nonlinear Response and Crosstalk of Electrically Driven Silicon Spin Qubits*, Phys. Rev. Applied **19**, 044078 (2023).